

FREQUENCY-DOMAIN SYNTHETIC APERTURE  
FOCUSING TECHNIQUES FOR IMAGING WITH  
SINGLE-ELEMENT FOCUSED TRANSDUCERS

by

Elyas Shaswary

M.Sc. Biomedical Physics, Ryerson University, 2013

B.Sc. Medical Physics, Ryerson University, 2010

A dissertation  
presented to Ryerson University  
in partial fulfillment of the  
requirements for the degree of  
Doctor of Philosophy  
in the program of  
Biomedical Physics

Toronto, Ontario, Canada, 2019

© Elyas Shaswary, 2019

# Author's Declaration

I hereby declare that I am the sole author of this dissertation. This is a true copy of the dissertation, including any required final revisions, as accepted by my examiners.

I authorize Ryerson University to lend this dissertation to other institutions or individuals for the purpose of scholarly research.

I further authorize Ryerson University to reproduce this dissertation by photocopying or by other means, in total or in part, at the request of other institutions or individuals for the purpose of scholarly research.

I understand that my dissertation may be made electronically available to the public.

# Abstract

## SYNTHETIC APERTURE FOCUSING TECHNIQUES FOR IMAGING WITH SINGLE-ELEMENT FOCUSED TRANSDUCERS

Elyas Shaswary

Doctor of Philosophy, Biomedical Physics

Ryerson University, 2019

Synthetic aperture focusing techniques (SAFT) make the lateral spatial resolution of the conventional ultrasound imaging from a single-element focused transducer more uniform. In this work, two new frequency-domain SAFT (FD-SAFT) algorithms are proposed, which are based on 2D matched filtering techniques. The first algorithm is the FD-SAFT virtual disk source (FD-VDS) that treats the focus of a focused transducer as a finite sized virtual source and the diffraction effect in the far-field is accounted for in the image reconstruction. The second algorithm is the FD-SAFT deconvolution (FD-DC) that uses the simulated point spread function of the imaging system as a matched filter kernel in the image reconstruction. These algorithms were implemented for pulsed and linear frequency modulated chirp excitations. The performance of these algorithms was studied using a series of simulations and experiments, and it was compared with the conventional B-mode and time-domain virtual point source SAFT (TD-VPS) imaging techniques. The image quality was analyzed in terms of spatial resolution,

sidelobe level, signal-to-noise ratio (SNR), contrast resolution, contrast-to-speckle ratio, and *ex vivo* tissue image quality. The results showed that the FD-VDS had the highest spatial resolution and FD-DC had the second highest spatial resolution. In addition, FD-DC had generally the highest SNR. The computation run time of the proposed methods was significantly lower than the TD-VPS. Furthermore, chirp excitation improves the SNR of all methods by about 8 dB without significantly affecting the spatial resolution and sidelobe level. Thus, the FD-VDS and FD-DC methods offer efficient solutions to make the spatial resolution of conventional B-mode imaging more uniform.

# Acknowledgements

I am very thankful and grateful to my supervisors Dr. J. Carl Kumaradas and Dr. Jahan Tavakkoli for providing guidance, support and training throughout my studies. Dr. Kumaradas has been instrumental in training me to be a better researcher and has taught me critical thinking skills. Dr. Tavakkoli has been very knowledgeable, supportive and patient, and his guidance helped me complete this research. I could not have imagined having better supervisors for my Ph.D. study.

I would like to thank committee members, Dr. Raffi Karshafian and Dr. Yuan Xu, for providing helpful feedback and guidance on this research work. I'm also thankful to the thesis examination committee members, Dr. Karthi Umopathy, Dr. Roger Zemp, Dr. Michael Kolios, and Dr. Raffi Karahafian, for providing valuable feedback to improve this thesis. Many thanks to Dr. Michael Kolios for providing access to the high-frequency ultrasound scanner, and to Mr. Arthur Worthington, Dr. Borna Maraghechi and Dr. Graham Ferrier for providing technical assistance. I would like to thank my fellow graduate students, support staffs, and faculty members at the Physics Department.

This work was partially supported by the Natural Sciences and Engineering Research Council of Canada Discovery Grants.

Last but not least, I would like to thank my family for their unconditional love, support and encouragement throughout my life.

# Contents

<b>Author’s Declaration</b>	<b>ii</b>
<b>Abstract</b>	<b>iii</b>
<b>Acknowledgements</b>	<b>v</b>
<b>List of Tables</b>	<b>ix</b>
<b>List of Figures</b>	<b>x</b>
<b>Abbreviations</b>	<b>xv</b>
<b>Symbols</b>	<b>xvii</b>
<b>1 Introduction</b>	<b>1</b>
1.1 Ultrasound Transducers . . . . .	2
1.2 Ultrasound Image Quality . . . . .	5
1.2.1 Spatial Compounding . . . . .	5
1.2.2 Frequency Compounding . . . . .	6
1.2.3 Coded Excitation . . . . .	7
1.2.4 Tissue Harmonic Imaging . . . . .	8
1.2.5 Synthetic Aperture Imaging . . . . .	12
1.3 Synthetic Aperture Focusing Technique . . . . .	13
1.3.1 SAFT for High-Frequency Single-Element Transducers	13
1.3.2 SAFT for Linear Array Transducers . . . . .	15
1.3.3 SAFT with Coded Excitation . . . . .	19
1.4 Thesis Hypothesis and Specific Aims . . . . .	19
1.5 Thesis Organization . . . . .	20
<b>2 Theory</b>	<b>21</b>
2.1 Wavenumber Algorithm . . . . .	21
2.1.1 Forward Model . . . . .	21
2.1.2 Image Reconstruction . . . . .	25
2.1.3 Stolt Transformation . . . . .	26

2.2	Image Quality Analysis . . . . .	28
2.2.1	Spatial Resolution . . . . .	28
2.2.2	Signal-to-Noise Ratio . . . . .	29
2.2.3	Contrast-to-Speckle Ratio . . . . .	30
2.2.4	Clutter Energy to Total Energy Ratio . . . . .	30
<b>3</b>	<b>Efficient Frequency-Domain Synthetic Aperture Focusing Techniques for Imaging with a High-Frequency Single-Element Focused Transducer</b>	<b>32</b>
3.1	Abstract . . . . .	33
3.2	Introduction . . . . .	33
3.3	Theory . . . . .	38
3.3.1	Frequency-Domain Virtual Source SAFT . . . . .	38
3.3.2	Frequency-Domain Deconvolution SAFT . . . . .	40
3.3.3	Time-Domain SAFT . . . . .	41
3.4	Methods . . . . .	42
3.4.1	Simulations . . . . .	43
3.4.2	Experiments . . . . .	46
3.5	Results and Discussion . . . . .	47
3.5.1	Spatial Resolution and Sidelobe . . . . .	47
3.5.2	Signal-to-Noise Ratio and Contrast Resolution . . . . .	50
3.5.3	Contrast-to-Speckle Ratio . . . . .	53
3.5.4	<i>Ex vivo</i> Tissue Image Quality . . . . .	53
3.5.5	Reconstruction Performance . . . . .	57
3.6	Conclusion . . . . .	59
3.7	Acknowledgements . . . . .	59
<b>4</b>	<b>The Use of Coded Excitation for Frequency-Domain Syn- thetic Aperture Focusing Techniques in Single-Element Ul- trasound Imaging</b>	<b>60</b>
4.1	Abstract . . . . .	61
4.2	Introduction . . . . .	61
4.3	Methods . . . . .	64
4.4	Results and Discussion . . . . .	67
4.4.1	Chirp Excitation Length . . . . .	67
4.4.2	Spatial Resolution and Sidelobe Level . . . . .	67
4.4.3	Signal-to-Noise Ratio . . . . .	70
4.4.4	Contrast-to-Speckle Ratio . . . . .	73
4.5	Conclusion . . . . .	74
4.6	Acknowledgements . . . . .	75
<b>5</b>	<b>Discussion, Conclusions, and Future Work</b>	<b>76</b>
5.1	Discussion . . . . .	76

5.2	Conclusion . . . . .	78
5.3	Future Work . . . . .	79
<b>A</b>	<b>Supplementary materials for Chapter 3</b>	<b>81</b>
A.1	Lateral Width of the Point Scatterer . . . . .	81
A.2	Statistical Analysis . . . . .	82
	<b>References</b>	<b>100</b>

# List of Tables

3.1	Simulation parameters for the point scatterer and tissue-mimicking phantoms. . . . .	44
4.1	The values of the simulation parameters for the point scatterer phantom. . . . .	66
4.2	The values of the simulation parameter for tissue-mimicking contrast phantom. . . . .	67

# List of Figures

1.1	An element of ultrasound transducer generating a travelling wave and receiving the wave scattered from a spherical object. Adopted from [3]. . . . .	2
1.2	Pressure field of a typical linear array transducer. In (a) a subset of the elements was used to focus the beam a point. In (b) the normalized far-field magnitude of the transmit pressure versus observation angle shown. . . . .	4
1.3	<i>In vivo</i> images of a scar (shown by the arrows) inside the dermis layer of the skin using a high-frequency (20 MHz) single-element focused transducer. In (a) the conventional B-mode and in (b) the spatial compounded image are shown. Adopted from [36]. . . . .	6
1.4	<i>In vivo</i> images of a breast lesion surrounded by the fatty background acquired by a linear array transducer. In (a) the conventional B-mode (at 14 MHz) and in (b) the frequency compounded images (at 10 MHz and 14 MHz) are shown. Adopted and modified from [38]. . . . .	7
1.5	<i>In vivo</i> images of a liver acquired by a 4 MHz single-element focused transducer. In (a) the linear frequency-modulated coded excitation and in (b) the conventional B-mode (pulsed) images are shown. Adopted from [40]. . . . .	8
1.6	<i>In vivo</i> images of a kidney from dorsal direction using a 3.4-7.2 MHz convex array transducer. In (a) the second harmonic at 6.6 MHz, in (b) fundamental at 6.5 MHz and in (c) fundamental at 3.4 MHz images are shown. Adopted from [45]. . . . .	10
1.7	A schematic illustration of the transmitted and received frequency spectra of the signal in tissue harmonic imaging. The bandwidth of the transducer must be wide enough to accommodate both transmit and receive bandwidths. Adopted from [11]. . . . .	11
1.8	Virtual point source at the focus of a single-element focused transducer. . . . .	14

1.9	Postmortem images of a rat pup's abdominal region (sagittal plane). In (a) conventional B-mode image, in (b) spatial compound image, in (c) TD-SAFT image, and in (d) TD-SAFT with spatial compounding image are shown. Images were acquired by a 20 MHz single-element focused transducer. Adopted from [65]. . . . .	15
1.10	Reconstructed images of point targets at various axial distances using (a) simulated and (b) experimental data. The transducer was 1 MHz single-element focused transducer with a focal distance of 76 mm and a diameter of 38 mm. Adopted from [68]. . . . .	16
1.11	Data acquisition in SAFT using an array transducer. Adopted from [32]. . . . .	17
1.12	Virtual point source for linear array transducer during transmission and reception. . . . .	18
2.1	Geometry for calculating the off-axis far-field response of circular transducer. Adopted from [88]. . . . .	22
2.2	Angular diffraction pattern of a circular plane piston transducer in the far-field. . . . .	22
2.3	Distribution of the data (a) in $(k_x, \omega)$ and (b) $(k_x, k_z)$ coordinates. Adopted from [87]. . . . .	25
2.4	Distribution of discrete data before and after interpolation. Adopted from [48]. . . . .	27
2.5	Point spread function (PSF) with $-6$ dB and $-24$ contour areas for the measurement of spatial resolution and sidelobe level, respectively. . . . .	29
2.6	Measurement of the signal-to-noise ratio. The signal is the image data inside the $-6$ dB contour area and the noise is image data inside a rectangular window in the background. . . . .	29
2.7	Measurement of the contrast-to-speckle ratio for quantifying tissue contrast between a region inside of a cyst and a region outside the cyst. . . . .	30
2.8	Measurement of the clutter energy to total energy ratio, that is the ratio of the energy of the signal outside a circle of $5\lambda$ diameter to the total energy of the signal. . . . .	31
3.1	Schematic FD-VDS. . . . .	40
3.2	Schematic diagrams of the phantom and image of the <i>ex vivo</i> tissue sample. (a) Custom-built nylon thread phantom. (b) Image of the <i>ex vivo</i> chicken heart. . . . .	47
3.3	Reconstructed images of the virtual point scatterer phantom in water. The focal distance of the transducer was 15 mm. . . . .	48

3.4	Reconstructed images of the nylon thread in a water phantom. The focal distance of the transducer was 15 mm. The prefocal region of (a) CONV, (b) TD-VPS, (c) FD-VDS, and (d) FD-DC. The postfocal region of the (e) CONV, (f) TD-VPS, (g) FD-VDS, and (h) FD-DC. . . . .	48
3.5	Contour area of the simulated data above (a) $-6$ and (b) $-24$ dB, and the contour area of the experimental data above (c) $-6$ and (d) $-24$ dB as a function of depth. The focal distance of the transducer was at 15 mm. . . . .	49
3.6	SNR of the (a) simulated and (b) experimental data as a function of depth. . . . .	51
3.7	Axial beam profiles for the simulated (left) and experimental (right) data. . . . .	51
3.8	Contrast resolution, measured by the CTR, of the (a) simulated and (b) experimental data as a function of depth. . . .	52
3.9	Reconstructed images of the virtual tissue-mimicking contrast phantom. The diameter of the inclusions was 3 mm. The contrast of the inclusions (from left to right) were $-15$ , $-5$ , $+5$ , and $+15$ dB relative to the background. (a) CONV, (b) TD-VPS, (c) FD-VDS, and (d) FD-DC are shown. The focal distance of the transducer was at 15 mm. . . . .	54
3.10	Measurement of the CSR of the inclusion contrast. Five different virtual tissue-mimicking contrast phantoms were scanned and the average contrast was calculated for each inclusion at various depths. The error bars represent the standard deviation. * represents $p$ -value $< 0.05$ compared to CONV. . . .	54
3.11	Reconstructed images of the <i>ex vivo</i> chicken heart tissue in water in the prefocal, focal, and postfocal regions of the transducer. (a) Cross-sectional image of the approximate scan region. The CONV images are shown in (b), (f), and (j), the TD-VPS images are shown in (c), (g), and (k), FD-VDS images are shown in (d), (h), and (l), and the FD-DC images are shown in (e), (i), and (m). . . . .	55
3.12	CSR measurement of the left ventricle of the heart (center of the tissue) at various depths. . . . .	56
3.13	Average computation time to reconstruct and display an image as a function of image size. For each image size. (The 10 data set was processed and all calculations were carried out in MATLAB.) . . . . .	58
3.14	Average computation time ratios between SAFT algorithms and the CONV as a function of image size. . . . .	58
4.1	Excitation signal (a) and its frequency spectrum (b). . . . .	65
4.2	Dependence of image quality parameters on chirp length. . . .	68

4.3	The reconstructed images of the virtual point scatterer phantom in water for the pulsed (top row) and coded (bottom row) excitations. The focal distance of the transducer was 15 mm.	69
4.4	The contour area of the pulsed excitation above $-6$ dB (a) and $-24$ dB (c), and the contour area of the coded excitation above $-6$ dB (b) and $-24$ dB (d) as a function of depth. . .	70
4.5	The ratio of the contour areas of chirp to pulsed excitations.	70
4.6	The average ratio of $-6$ dB and $-24$ dB contour areas between various methods and the average difference in SNR between the various methods in the pre-focal, focal and post-focal regions for the pulsed (left column) and chirp (right column) data. The error bars represent the standard deviation of the ratios and difference and * represents a p-value $< 0.05$ .	71
4.7	The signal-to-noise ratio (SNR) of the pulsed (a) and chirp (b) excitations as a function of depth. . . . .	72
4.8	SNR difference between chirp and pulsed excitations. The error bars represent the standard deviation of the difference in SNR between the regions around the point scatterers and * represents a p-value $< 0.05$ . . . . .	72
4.9	The reconstructed images of the virtual tissue-mimicking contrast phantom for the pulsed (top row) and coded (bottom row) excitations. The diameter of the inclusions was 3 mm. The contrast of the inclusions (from left to right) was $-15$ dB, $-5$ dB, $+5$ dB, and $+15$ dB relative to the background. The focal distance of the transducer was at 15 mm. . . . .	73
4.10	The measurement of the CSR of the inclusion contrast. 5 different virtual tissue-mimicking contrast phantoms were scanned and the average contrast was calculated for each inclusion at various depths for both (a) pulsed and (b) coded excitations. The error bars represent the standard deviation of CSR and * represents p-value $< 0.05$ compared to conventional B-mode.	74
5.1	Simulated pressure field for pulsed excitation of (a) a focused source, (b) a point source, and (c) a disk source. . . . .	77
A.1	The scatterer lateral width of the simulated data at $-6$ dB (a) and $-24$ dB (b), and experimental data at $-6$ dB (c) and $-24$ dB (d) as a function of depth. The focal distance of the transducer was at 15 mm . . . . .	82

A.2 The average ratio difference in the contour areas above  $-6$  dB and  $-24$  dB, the average ratio difference in the lateral width of the point scatterers at  $-6$  dB and  $-24$  dB, and the average difference in SNR between the conventional B-mode, TD-VPS, FD-VDS, and FD-DC in the pre-focal, focal and post-focal regions. For the simulated (left column) and experimental (right column) data. The error bars represent standard deviation and \* represents  $p$ -value  $< 0.05$ . . . . . 83

# Abbreviations

<b>CHRP</b>	<b>Chirp</b>
<b>CONV</b>	<b>Conventional B-mode</b>
<b>CSR</b>	<b>Contrast-to-Speckle-Ratio</b>
<b>CTR</b>	<b>Clutter Energy To Total Energy Ratio</b>
<b>DAS</b>	<b>Delay-And-Sum</b>
<b>DC</b>	<b>Deconvolution</b>
<b>FD</b>	<b>Frequency-Domain</b>
<b>FFT</b>	<b>Fast Fourier Transform</b>
<b>FWHM</b>	<b>Full-Width-at-Half-Maximum</b>
<b>LTI</b>	<b>Linear Time-Shift Invariant</b>
<b>MRI</b>	<b>Magnetic Resonance Imaging</b>
<b>PLSD</b>	<b>Pulsed</b>
<b>PSF</b>	<b>Point Spread Function</b>
<b>RF</b>	<b>Radio Frequency</b>
<b>RMS</b>	<b>Root Mean Square</b>
<b>ROI</b>	<b>Region Of Interest</b>
<b>SAFT</b>	<b>Synthetic Aperture Focusing Technique</b>
<b>SAR</b>	<b>Synthetic Aperture Radar</b>
<b>SAS</b>	<b>Synthetic Aperture Sonar</b>
<b>SNR</b>	<b>Signal-to-Noise-Ratio</b>
<b>STA</b>	<b>Synthetic Transmit Aperture</b>
<b>TD</b>	<b>Time-Domain</b>

<b>TGC</b>	<b>Time Gain Compensation</b>
<b>VDS</b>	<b>Virtual Disc Source</b>
<b>VPS</b>	<b>Virtual Piont Source</b>

# Symbols

$*$	complex conjugate	
$a$	radius of virtual source	m
$A$	directivity spectrum	
$c_0$	speed of sound	m/s
$D$	diameter of virtual source	m
$\Delta_x$	lateral scan step size	m
$F$	object reflectivity spectrum	
$\hat{F}$	reconstruction image spectrum	
$H$	electro-mechanical impulse response spectrum	
$f_s$	sampling frequency	Hz
$k$	wavenumber	rads/m
$\mu$	mean	
$n$	transducer position	
$\omega$	angular frequency	rads/s
$P$	excitation signal spectrum	
$\phi_D$	divergence angle	radian
$\mathcal{S}\{\cdot\}$	Stolt transformation	
$\sigma$	standard deviation	
$x$	lateral direction	
$z$	axial direction	
$z_c$	distance to the ROI midpoint	m
$z_f$	focal length of transducer	m

# Chapter 1

## Introduction

Ultrasound is an extensively used imaging modality, second only to conventional x-ray imaging [1]. Besides a wide range of industrial imaging applications in areas such as nondestructive testing and evaluation (NDT/NDE) [2], [3], it is commonly used in clinical diagnosis to obtain both anatomical and functional images of the body. A few notable examples of clinical applications of ultrasound imaging are cardiology, obstetrics and gynaecology, urology, general abdominal imaging, vascular imaging, and guidance of surgical procedures [4]. In addition to its use in clinical diagnosis, ultrasound has many therapeutic applications. For example, it is used in cancer therapy, physiotherapy, histotripsy, immunotherapy, lithotripsy, and targeted drug delivery [5], [6].

Ultrasound imaging not only complements other medical imaging modalities, such as x-ray and magnetic resonance imaging (MRI), but it also possesses unique characteristics that are advantageous compared to other imaging modalities [7]. Ultrasound is able to image the anatomy, the dynamic movement of organs and blood flow in real-time. Ultrasound is considered safe because it is non-ionising radiation and the induced bioeffects (e.g., tissue heating and acoustic cavitation) are relatively well understood and controllable. In addition, ultrasound is relatively inexpensive and portable.

## 1.1 Ultrasound Transducers

The ultrasound transducer is one of the most critical component of an ultrasound imaging system. The transducers elements are typically made of a piezoelectric material, which converts electric energy into mechanical motion of the element and vice versa [3]. Fig. 1.1 outlines the role of the transducer in ultrasound imaging. When the transducer is excited by an electrical pulse, a travelling pulse of ultrasound in the form of an acoustic wave will be generated in the water and if this wave strikes an object, such as a spherical reflector, then the waves will get scattered in all directions where some of the waves will return to the transducer. The returned wave, which is also referred to as the backscattered wave, will be converted back into an electrical signal by the transducer and recorded as a voltage versus time pulse after amplification.

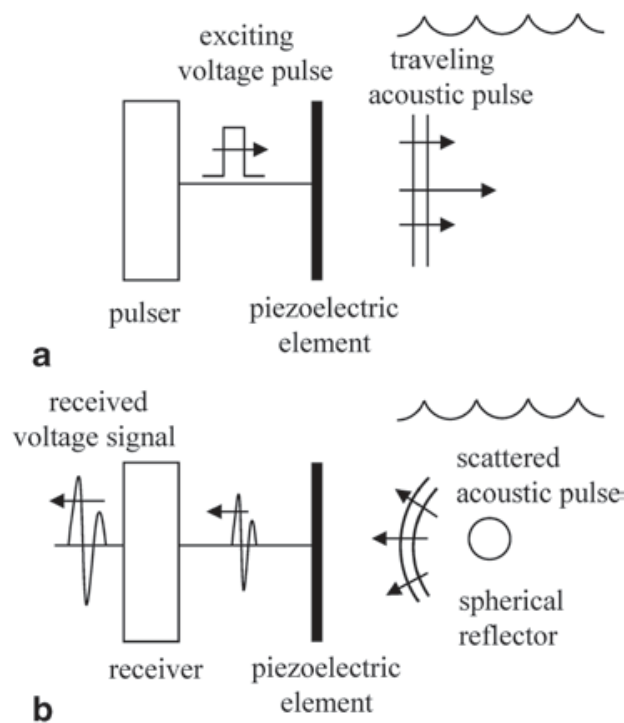


Fig. 1.1. An element of ultrasound transducer generating a travelling wave and receiving the wave scattered from a spherical object. Adopted from [3].

Ultrasound transducers are available in various sizes, shapes, and operating

frequencies. Each one is optimized for specific clinical applications [1]. Common transducer geometries include focused and unfocused single-elements and linear, curvilinear and annular arrays. Single-element transducers are primarily used in high-frequency (i.e., 20-100 MHz) imaging [8] and in most therapeutic applications. Two-dimensional images are formed by mechanical translation or rotation of the single-element transducer. Linear and phased array transducers are more widely used for clinical imaging. Array transducers offer electronic scanning, which is faster than mechanical scanning resulting in an increased temporal resolution [9]. Linear array transducers mimic mechanical translation of the transducer by firing elements sequentially in a linear fashion to move the ultrasound beam [10]. They are typically used when the acoustic window (i.e., imaging region that is not obstructed by bone or gas-filled structures) is large (e.g., in vascular and obstetrics imaging). Phased array transducers mimic mechanical tilting of the transducer by tuning the phases of the pulses fired by its elements to steer the direction of the ultrasound beam. They are typically used in applications where the acoustic window is small, for example in cardiology to image the heart through a small space in between the ribs. An example of a pressure field of a linear array transducer is shown in Fig. 1.2. A general shortcoming of array transducers over single-element transducers is the generation of higher levels of grating lobes [11]. Grating lobes are weak replicas of the main beam, which appears at angles of up to  $90^\circ$  on each side of the main beam. Grating lobes are generated in an array transducer having regularly spaced elements, where the element-to-element spacing is greater than half a wavelength. Grating lobes widen the beam and generate spurious echoes, which degrade lateral and contrast resolutions [11]. Sidelobes also produce spurious echoes that reduce contrast resolution (i.e., a measure of how well the differences in the mean amplitude of the received ultrasound signal from different scattering media can be differentiated [12]). The number and magnitude of the sidelobes relative to the main lobe depend on the shape of the transducer and the ratio of transducer aperture size to wavelength [7].

The performance of the transducer is one of the bottlenecks preventing current ultrasound imaging systems from reaching its theoretical resolution

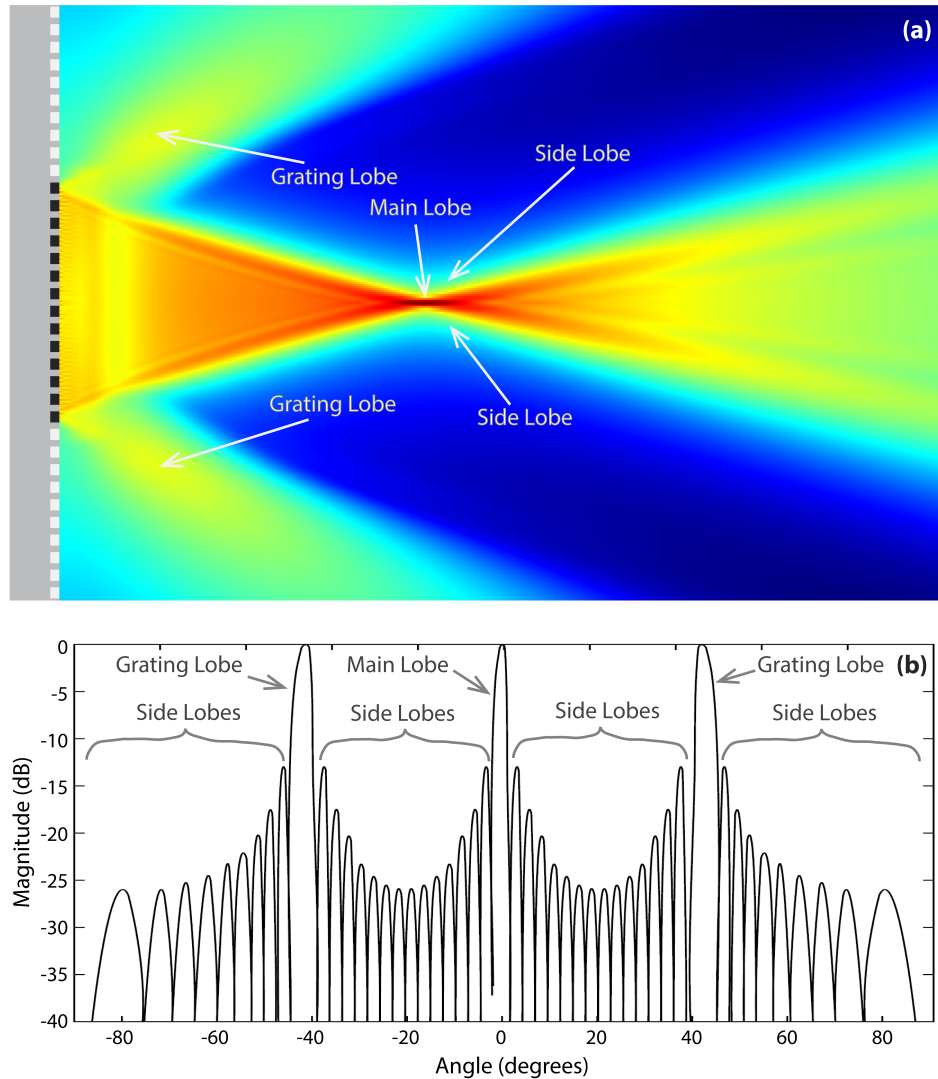


Fig. 1.2. Pressure field of a typical linear array transducer. In (a) a subset of the elements was used to focus the beam a point. In (b) the normalized far-field magnitude of the transmit pressure versus observation angle shown.

limit [7]. The main reason for this is that the design and fabrication of medical ultrasound transducers are broad interdisciplinary processes which require expertise from various disciplines, such as acoustic, electrical engineering, material sciences, and medical imaging. The design of transducers is still predominantly empirical and it is often based on a trial and error. The ideal transducers would have a characteristic acoustic impedance perfectly matched to the object being imaged, have a high efficiency as a transmitter and high sensitivity as a receiver, a wide dynamic range (i.e.,

range of minimum to maximum detectable pressures) and a wide frequency response (i.e., a wide bandwidth) [13].

## 1.2 Ultrasound Image Quality

Improvements in the design and the fabrication of ultrasound transducers make the most significant difference in enhancing ultrasound imaging. In addition, ultrasound image quality can be improved through non-conventional signal generation and acquisition, and advanced signal processing methods [4]. Examples include, but not limited to, spatial and frequency compounding [14]–[18], coded excitation [19]–[21], tissue harmonic imaging [22]–[24], pulse inversion [25]–[27], filtering [28], [29], and synthetic aperture imaging [30]–[33]. Ultrasound images are affected by various artifacts, such as speckle, clutter and noise. Speckle refers to a granular texture in ultrasound images, which arises from constructive and destructive interference of ultrasound waves that are scattered from multiple scatterers with varying positions and scattering strengths within the beam [7], [11]. Speckle reduces image contrast and blurs tissue boundaries [1]. Clutter (or acoustic noise) refers to spurious echoes, which typically arises from the distortion of an ultrasound beam as it propagates in tissue [4], [34]. Examples of clutter include sidelobes, grating lobes, reverberation, and acoustic shadowing [34]. Noise refers to artifacts which are initiated by the ultrasound imaging system due to electronic, quantization and image reconstruction artifacts.

### 1.2.1 Spatial Compounding

Spatial compounding is a technique that combines images taken from various angles using an array transducer [34]. The ultrasound beam is electronically steered to predetermined angles, typically within  $20^\circ$  from the perpendicular direction, to acquire several frames (typically three to nine). The acquired frames are then aligned (e.g., using a cross-correlation method) and averaged to form a compound image that is updated in real-time with

each subsequent scan. Spatial compounding has also been done by physically translation of the array transducer in the lateral direction [35] and the combination of angular and lateral displacements [36]. An example of spatial compounding in ultrasound imaging is shown in Fig. 1.3. It has been reported that spatial compounding improves contrast resolution and signal-to-noise ratio (SNR), without compromising spatial resolution, by reducing artifacts such as speckle, clutter and noise [4], [34]–[36]. The main drawbacks of spatial compounding techniques are a reduction in temporal resolution, and blurredness of moving objects [4], [34].

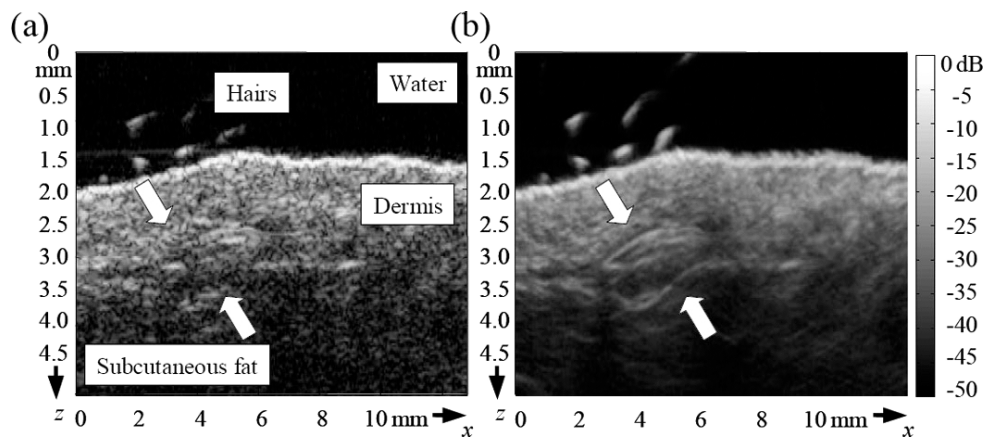


Fig. 1.3. *In vivo* images of a scar (shown by the arrows) inside the dermis layer of the skin using a high-frequency (20 MHz) single-element focused transducer. In (a) the conventional B-mode and in (b) the spatial compounded image are shown. Adopted from [36].

## 1.2.2 Frequency Compounding

Frequency compounding is a technique, which combines images acquired using multiple frequencies. Since the appearance of speckle depends on the frequency of the ultrasound wave combining images with different frequencies leads to a reduction of speckle [1], [37]. It can be done either during transmit mode by transmitting pulses at different centre frequencies or during receive mode by subdividing the frequency spectrum of the received signal into sub-bands to make separate images [4]. This method requires transducers with large enough bandwidth to be able to cover a sufficient frequency range [37]. It has been shown that frequency compounding, using the frequency spectrum subdivision method, enhances SNR and contrast

resolution without compromising spatial resolution [29]. An example of a frequency compounded ultrasound image is shown in Fig. 1.4.

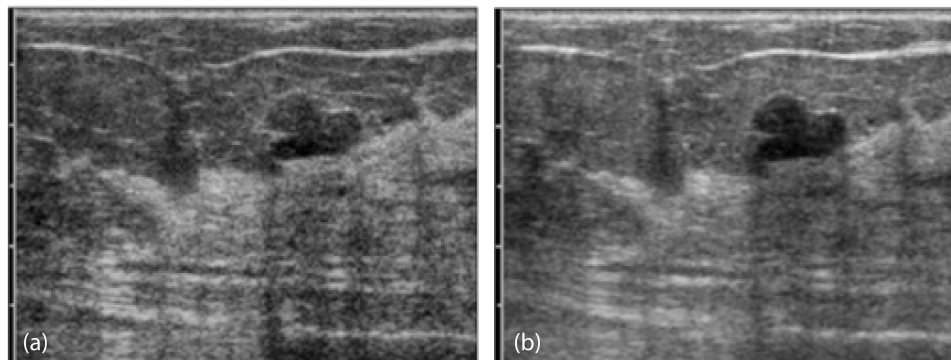


Fig. 1.4. *In vivo* images of a breast lesion surrounded by the fatty background acquired by a linear array transducer. In (a) the conventional B-mode (at 14 MHz) and in (b) the frequency compounded images (at 10 MHz and 14 MHz) are shown. Adopted and modified from [38].

### 1.2.3 Coded Excitation

Coded excitation techniques digitally encode the transmitted pulses before the transmission and digitally decode the received echo signals after the reception. High frequency transmit pulses forms a narrow beam which provides good lateral resolution and short transmit pulses provides good axial resolution [11]. However, high frequency and short ultrasound transmit pulses are attenuated more rapidly, which reduces the SNR and the penetration depth. Although increasing the amplitude of the transmitted pulses increases the SNR of the received signals which also increases penetration depth, this is not a viable solution due to potential bioeffects and regulatory limits. Transmitting longer pulses increases the SNR of the received signal, however, it reduces the axial resolution [20]. Coded excitation has been proposed to increase SNR without significantly reducing the axial resolution or increasing the amplitude of the transmitted pulses [20], [39]. Coded excitation techniques generate longer duration and lower amplitude transmitted pulses, compared to the conventional method. Coded excitation can be done by sweeping the frequency within the pulse (from low to high within the bandwidth of the transducer), known as a chirp signal. In addition,

coded excitation can be done by modulating the pulses with binary code (e.g., orthogonal Golay or Barker codes) [13], [20]. The received signals are correlated with the time-reversed version of the transmitted pulses by a matched filter to obtain compressed received signals [13]. The main drawbacks of this technique are system complexity and cost [11]. An example of an ultrasound image generated by the chirp coded excitation is shown in Fig. 1.5 where coded excitation shows improved SNR and penetration depth.

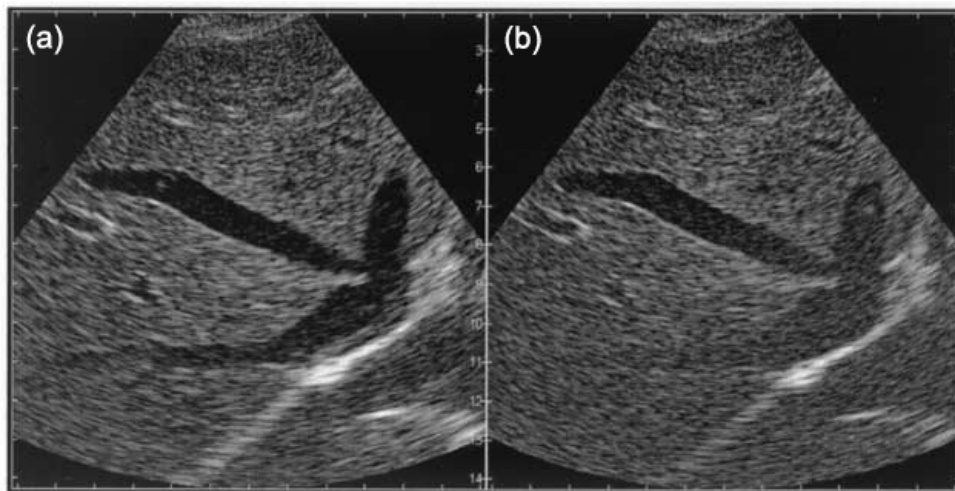


Fig. 1.5. *In vivo* images of a liver acquired by a 4 MHz single-element focused transducer. In (a) the linear frequency-modulated coded excitation and in (b) the conventional B-mode (pulsed) images are shown.

Adopted from [40].

### 1.2.4 Tissue Harmonic Imaging

Tissue harmonic imaging makes use of the harmonic frequencies that are generated by nonlinear propagation of ultrasound waves in a medium to form B-mode images. Ultrasound waves become progressively distorted as they propagate in a medium; however, the degree of distortion is more prominent with the transmission of high amplitude (also known as finite amplitude) waves [11], [41]. In addition, the degree of distortion depends on the medium properties [41].

There are two competing mechanisms that change the shape of a wave as it propagates in a medium [9]. The first one is the frequency-dependent attenuation, which down-shifts the central frequency of the transmitted wave. The second mechanism is the combined effects of the changes in the speed of sound and the effect of convection. The speed at which the transmitted wave propagates in a medium depends on the density of the medium. The wave propagates faster during the compression phase and slower during the rarefaction phase, which causes portions of the wave to become steeper as the wave propagates further into the medium, resulting in the production of higher harmonics. In addition, the propagating wave is convected because during the compression phase the medium moves in the direction of wave propagation and in the opposite direction during rarefaction phase, which leads to distortion of the wave similar to the speed of sound variation [9]. The amount of nonlinearity of a medium is quantified by either the ratio  $B/A$  or the coefficient of nonlinearity,  $\beta$ .  $B/A$  is the ratio of coefficients of the quadratic and linear terms in the Taylor series expansion which relates variations in acoustic pressure to variations in density of the medium [42].  $\beta$  is defined as  $\beta = 1 + B/2A$ . For soft tissues, the range of  $\beta$  is between 3 and 7 [1].

As a finite amplitude wave propagates in a nonlinear medium, the energy from the fundamental frequency is partially transferred to the harmonic frequencies, which are multiples of the fundamental frequency. The harmonic frequencies are produced cumulatively with increasing depth up to a point where tissue attenuation overcomes the harmonic buildup and causes them to decrease again [43]. The amplitude of the harmonics is always lower compared to the fundamental at all depths. For a focused beam, there will be minimal distortion close to the transducer, because the amplitude is relatively small, and the transmitted pulse has not propagated through sufficient tissue to produce much distortion. Most of the distortion occurs close to the focal zone, where the amplitude of the pulse is the largest. Beyond the focal zone, the distortion decreases since attenuation reduces the amplitude of the pulse [41].

In tissue harmonic imaging, the received signal is filtered so that the second harmonic frequency band is utilized to form the image [41]. Although

theoretically, it is possible to use higher harmonics, they are rarely utilized because they are low in amplitude and require wide bandwidth and large dynamic range transducers [1], [41].

Tissue harmonic imaging improves the spatial and contrast resolution of B-mode images compared to conventional ultrasound imaging [1], [4], [13]. The second harmonic has a beam profile with a narrower central lobe and lower sidelobes compared to the profile at the fundamental frequency [4], [44]. An example of tissue harmonic imaging is shown in Fig. 1.6. In addition, tissue harmonic imaging is particularly beneficial to examine "clinically difficult" subjects (e.g., patients with obesity or dense muscle structure) [13], [43], [44]. Harmonics can penetrate more deeply into the tissue because they are generated cumulatively until they are offset by the tissue attenuation and low frequency transmitted waves suffer little distortion when passing through superficial tissues [7], [13].

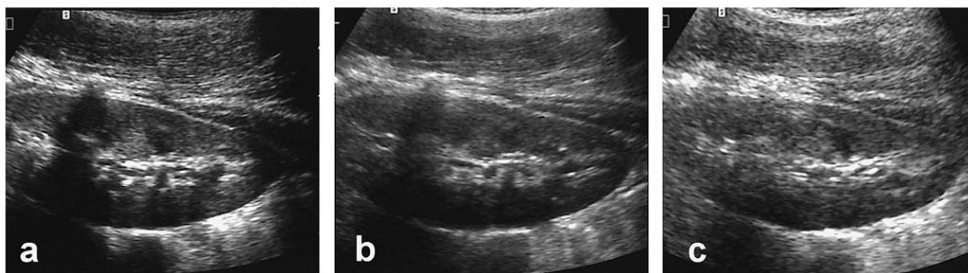


Fig. 1.6. *In vivo* images of a kidney from dorsal direction using a 3.4-7.2 MHz convex array transducer. In (a) the second harmonic at 6.6 MHz, in (b) fundamental at 6.5 MHz and in (c) fundamental at 3.4 MHz images are shown. Adopted from [45].

Tissue harmonic imaging requires a wide bandwidth transducer so that the frequency spectrum of both the transmitted and received second harmonic signals are within the bandwidth of the transducer [13], [41]. As shown in Fig. 1.7, if the transmit and receive bandwidths overlap with each other, then linear echo signal from the tissue will be detected in the harmonic signal. This can mask the nonlinear echoes from weak scatterers resulting in a reduction of contrast in harmonic signal [46]. One way to alleviate this issue is to transmit longer pulses so that the frequency spectrum of the transmitted pulse is narrower to reduce the degree of overlapping. However,

this will come at the cost of reducing the axial resolution. Two other well-known methods to overcome this issue, at the cost of frame rate, are pulse inversion and amplitude modulation [1], [7], [13], [41].

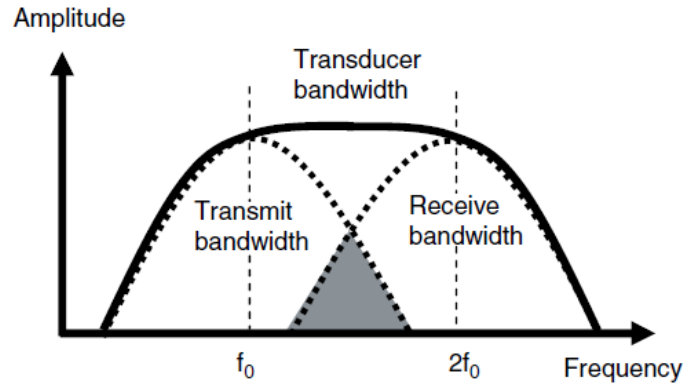


Fig. 1.7. A schematic illustration of the transmitted and received frequency spectra of the signal in tissue harmonic imaging. The bandwidth of the transducer must be wide enough to accommodate both transmit and receive bandwidths. Adopted from [11].

The pulse inversion method transmits two pulses sequentially, where one pulse is inverse (i.e.,  $180^\circ$  out of phase) of the previous one [41]. When the received signals are summed up the linear echoes will cancel since they have the same amplitude and a phase difference of  $180^\circ$ . However, the nonlinear echoes will not cancel in the summed signal because the phase difference will not differ by  $180^\circ$ . This results in the omission of the fundamental frequency component while keeping the harmonic frequencies. In this method, even harmonics are emphasized and odd harmonics (including the fundamental) are suppressed [26], [46].

Amplitude modulation method transmits two pulses of different amplitudes sequentially in the same direction [41]. The lower amplitude pulse propagates linearly (without producing significant harmonics), while the higher amplitude pulse propagates nonlinearly and will give rise to harmonics. The received signals are normalized (so that they have the same amplitude) before the lower amplitude pulse is subtracted from the higher amplitude pulse, which results in a signal with only harmonic frequencies. Unlike the pulse inversion method which cancels odd harmonics and keeps even harmonics,

this method cancels only the fundamental and keeps all higher harmonics [1].

In addition, tissue harmonic imaging requires a system with a large dynamic range because the amplitudes of the second harmonics are typically at least 20 dB lower than the fundamental [1], [41]. Moreover, tissue harmonic imaging has limited depth of penetration because of low SNR and high tissue attenuation at higher frequencies.

Even though tissue harmonic imaging has been shown in numerous studies to improve spatial and contrast resolution, under some circumstances it does not perform better than conventional (fundamental) ultrasound imaging [1]. For example, in some high-frequency imaging applications or in imaging of normally easy-to-image subjects, tissue harmonic imaging may not provide additional diagnostic benefits. Thus, tissue harmonic imaging is still in its infancy and more work needs to be done to study its benefits and limitations. Some current ultrasound imaging systems combine fundamental and harmonic images (i.e., frequency compound) to reduce speckle and improve image quality [1].

### 1.2.5 Synthetic Aperture Imaging

Synthetic aperture imaging techniques have been used in synthetic aperture radar (SAR) since the early 1950s [47], [48]. SAR is considered to be one of the most advanced engineering innovations of the 20th century [48]. SAR has been used to obtain high-resolution images of remote objects on a terrain or a planet. SAR uses signal-processing methods to generate an effective long antenna instead of actually using a physically long antenna [49]. Typically, an antenna is mounted on an airplane or satellite, which travels along a flight trajectory while transmitting electromagnetic pulses (in the frequency range of 2 MHz to 220 GHz [50]) and recording the scattered pulses [47]. Mathematical techniques are applied to the received signal to form high-resolution images. Synthetic aperture imaging techniques have been subsequently implemented in sonar (i.e., synthetic aperture sonar [SAS]) [51], non-destructive evaluation (NDE) [52] and medical imaging [53].

## 1.3 Synthetic Aperture Focusing Technique

Synthetic aperture imaging techniques are also commonly referred to as synthetic aperture focusing techniques (SAFT). Numerous SAFT algorithms have been proposed in both frequency and time domains. SAFT algorithms for SAR and SAS are mainly implemented in the frequency-domain, which are computationally more efficient since they are based on the fast Fourier transform [48], [54]–[56]. On the other hand, SAFT algorithms for NDE and ultrasound medical imaging are mainly implemented in the time-domain [30], [31], [52], [56]–[59]. In ultrasound medical imaging, SAFT with linear arrays and high-frequency single-element focused transducers are commonly used for a wide range of applications.

### 1.3.1 SAFT for High-Frequency Single-Element Transducers

The acquisition of data with a single-element transducer is done in the same way as conventional pulse-echo imaging, where the transducer is mechanically scanned over the region-of-interest (ROI). At each scan position, a scan of data (known as the analytical signal) is acquired to form a 2D data set of the ultrasonic reflectivity map from the insonified ROI. Then, SAFT is applied off-line to the acquired data so that each point in the image is in focus [60]. Generally, the SAFT algorithms in the literature can be categorized into time-domain SAFT and frequency-domain SAFT.

Time-domain SAFT (TD-SAFT) is based on a delay-and-sum (DAS) beamforming method. For focused transducers, the concept of a virtual point source is typically used, where the focal point of the transducer is treated as a virtual source of spherical waves. A schematic of the virtual point source concept is shown in Fig. 1.8. The virtual point source concept was initially introduced by Passmann and Ermert [61], where it was implemented in high-frequency ultrasound imaging (100 MHz) for dermatologic and ophthalmologic applications. It was shown that virtual point source TD-SAFT (TD-VPS) increases imaging depth and extends the depth of focus when

using a high-frequency and strongly focused transducer. Subsequently, Frazier and O'Brien [62] examined the performance of the virtual point source in terms of lateral resolution, sidelobe levels, sampling frequency, and SNR. The spatial resolution and SNR of conventional B-mode at the focus of the transducer was  $157 \mu\text{m}$  and 39 dB, respectively. The average spatial resolution and SNR at various depths of the TD-VPS was  $195 \mu\text{m}$  and 35 dB, respectively. Apodization was applied to improve contrast resolution since the sidelobe levels were high in SAFT compared to conventional B-mode. Li *et al.* [63] implemented TD-VPS in high-frequency ultrasound imaging, where it was combined with an adaptive weighting technique to suppress sidelobes. Opretzka *et al.* [64] implemented TD-VPS in high-frequency ultrasound imaging for small animal imaging, where it was based on time-domain 2D cross-correlation of measured data with a simulated depth-dependent point spread function (PSF) of the imaging system. For the conventional B-mode, the axial and lateral resolutions at the focus of the transducer were  $52 \mu\text{m}$  and  $150 \mu\text{m}$ , respectively. While for the TD-VPS the axial and lateral resolutions outside the focal region were  $59 \pm 14 \mu\text{m}$  and  $196 \pm 41 \mu\text{m}$ , respectively. In addition, Opretzka *et al.* [65] combined their proposed method in [64] with spatial compounding to improve contrast and reduce speckle noise and other image artifacts, as shown in Fig. 1.9. However, the computational time was significantly higher (by a factor of approximately 500) compared to conventional TD-VPS method.

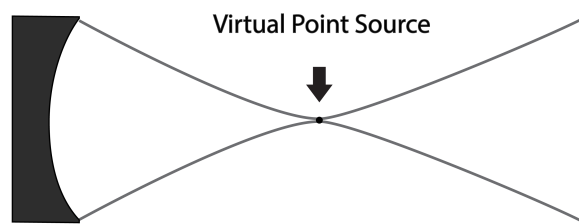


Fig. 1.8. Virtual point source at the focus of a single-element focused transducer.

Frequency-domain SAFT (FD-SAFT) based on spatial-temporal matched filtering was introduced in ultrasound imaging by Ermert and Karg [66]. For a single-element focused transducer, several FD-SAFT implementations have been proposed [56], [60], [67]. Stepinski [56] proposed a FD-SAFT algorithm based on the wavenumber algorithm in SAR [48], [54] for industrial

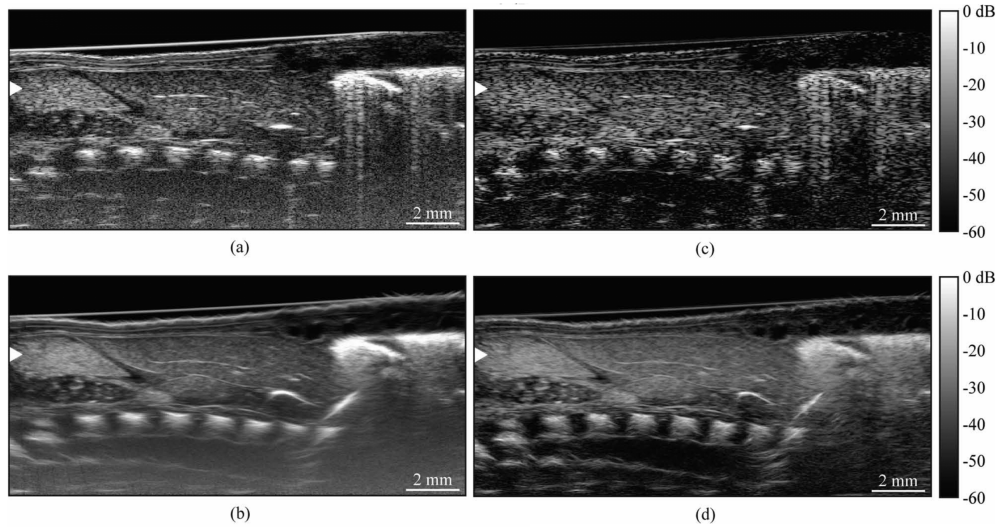


Fig. 1.9. Postmortem images of a rat pup's abdominal region (sagittal plane). In (a) conventional B-mode image, in (b) spatial compound image, in (c) TD-SAFT image, and in (d) TD-SAFT with spatial compounding image are shown. Images were acquired by a 20 MHz single-element focused transducer. Adopted from [65].

applications using a flat circular piston transducer. The algorithm took into consideration the far-field diffraction effects and the electromechanical impulse response of the transducer. It was reported that FD-SAFT improves axial and lateral resolutions by about 40% and 30%, respectively, compared to TD-SAFT. Vos *et al.* [68] presented a virtual point source FD-SAFT (FD-VPS) algorithm, based on the Stolt transformation, for medical imaging using a low frequency (1 MHz) single-element focused transducer and a linear array transducer. Its performance was compared to TD-VPS in terms of spatial resolution, SNR and computationally efficiency. As shown in Fig. 1.10, the size of the point targets was similar between FD-VPS and TD-VPS. The SNR of FD-VPS was lower by about 9 dB compared to TD-VPS. However, FD-VPS was computationally more efficient than TD-VPS.

### 1.3.2 SAFT for Linear Array Transducers

For a linear array, SAFT algorithms mathematically synthesize an effective long aperture (assuming the size of the aperture is the element size) by transmitting with one element of the array and receiving with all the elements

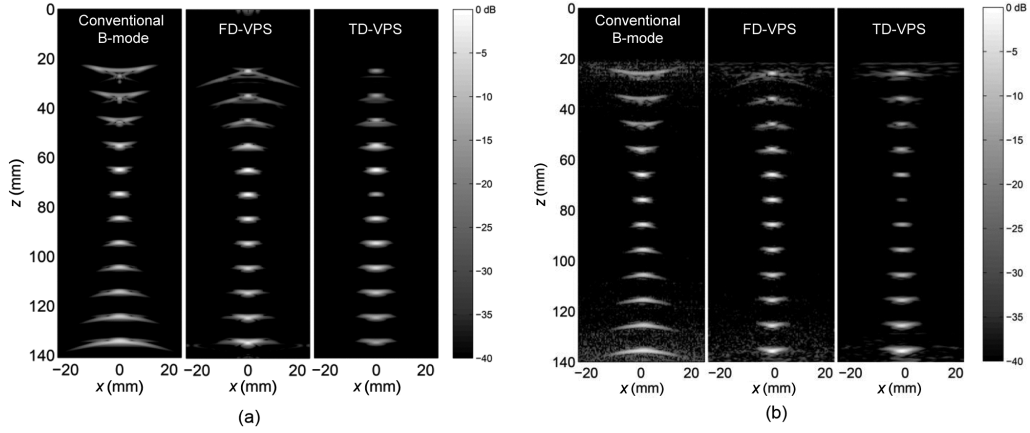


Fig. 1.10. Reconstructed images of point targets at various axial distances using (a) simulated and (b) experimental data. The transducer was 1 MHz single-element focused transducer with a focal distance of 76 mm and a diameter of 38 mm. Adopted from [68].

and iterating with the rest of the array elements while always receiving with all the elements [31]. The process illustrated in Fig. 1.11. The approach is also referred to as synthetic transmit aperture (STA) imaging [69]. The received data from each transmission is stored for off-line processing, where delay-and-sum (DAS) beamforming is applied to construct a low resolution image that is only focused in receive because of unfocused transmission [31]. The low resolution images are combined to form a high resolution image, which is dynamically focused in both transmit and receive. The transmit focusing is synthesized by combining low resolution images and focusing calculation (i.e., DAS) for all the transmit and receive element pairs making the transmit focus dynamic for all the points in the image resulting in improved spatial resolution compared to conventional B-mode. Several simulations, phantom and in vivo studies have confirmed the improvement in overall image quality (including spatial resolution) [70]–[73].

The limitations of TD-SAFT for array transducer are: (1) poor SNR and limited penetration depth because of weak and unfocused transmission from a single element, (2) low frame rate and high sensitivity to motion because of the required long acquisition time to form a single high resolution image, and (3) large number of receiving channels required for processing, transferring and storage of the data [31], [74]. Several methods have been proposed in the literature to address some of these limitations.

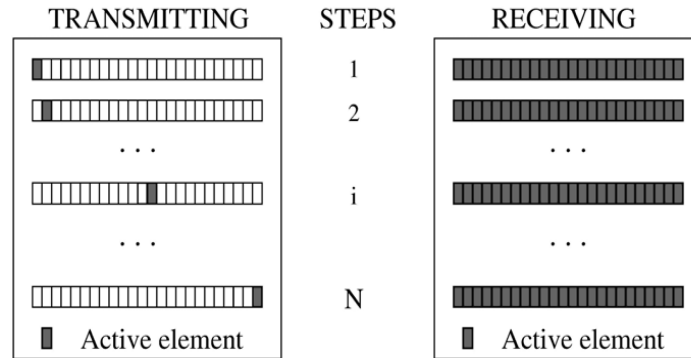


Fig. 1.11. Data acquisition in SAFT using an array transducer. Adopted from [32].

To overcome the issue of poor SNR and limited penetration depth, O'Donnell and Thomas [58] proposed the use of multi-element subaperture for intravascular imaging using a circular array transducer. In this method, multiple adjacent elements were excited simultaneously by applying defocusing delays to each element to emulate an extended single-element producing a spherical wave. Subsequently, this method was investigated by Karaman *et al.* [70] for small scale systems (i.e., a system with low channel counts), by Lockwood *et al.* [75] for sparse synthetic aperture systems (i.e., a system which utilizes fewer transmit subapertures compared to STA for each image) for 3D imaging, by Nikolov *et al.* [76] for recursive ultrasound imaging (i.e., a system which updates the high resolution image with each transmission), and by Tasinkevych *et al.* [77] for taking into account the angular directivity function of the transmit and receive subapertures.

In addition, the concept of virtual point source was also implemented for array transducer by several investigators following its introduction by Passmann and Ermert [61] to increase SNR and penetration depth. Subsequently, virtual point source using time-domain SAFT has been studied by Bae and Jeong [78], Nikolov and Jensen [79], [80], and Kortbek *et al.* [74], where all have concluded that images with depth-independent spatial resolution can be obtained. A subset of elements is used to focus the beam at a point by applying appropriate time delays to each element during the transmission, as shown in Fig. 1.12. During the reception, the location of the transmit focus is treated as the (virtual) source of spherical waves and

delay-and-sum (DAS) beamforming is used, which applies appropriate time delays to each element before summing the received signals to generate a scan line. Subsequently, the next set of elements is used to transmit and receive another scan line at the next scan position. Once all the scan lines are acquired then SAFT image reconstruction, based on DAS, is applied to dynamically focus the image at all locations in the ROI.

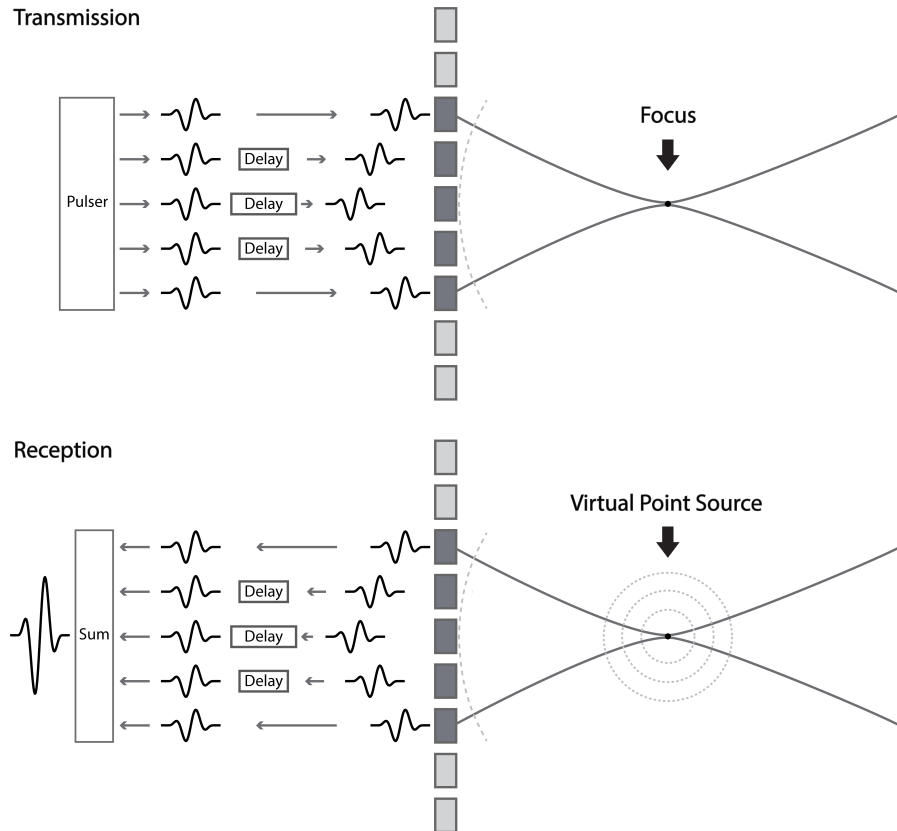


Fig. 1.12. Virtual point source for linear array transducer during transmission and reception.

Nikolov *et al.* [76] have suggested a recursive method to address the issue of low frame rate in synthetic aperture imaging, in which the high-resolution image is updated with each pulse transmission by replacing the low-resolution image of each transmit aperture. This is done recursively resulting in a new image with each transmission. The issue of high motion sensitivity during data acquisition has been investigated by several investigators and techniques to compensate tissue motion have been proposed, which are typically based on time-delay estimation using cross-correlation methods [31], [81], [82].

### 1.3.3 SAFT with Coded Excitation

Several studies have examined performing coded excitation prior to SAFT to increase SNR by around 15 dB. Passmann and Ermert [61] combined chirp coded excitation with TD-VPS for imaging with a 100 MHz single-element focused transducer. It was reported that coded excitation resulted in about a 14 dB increase in SNR and TD-VPS resulted in improved lateral resolution. Chiao and Thomas [83] combined orthogonal Golay coded excitation with STA for imaging with linear array transducer to increase SNR by about 18 dB. Misaridis and Jensen [84] combined chirp coded excitation with Hadamard spatial encoding with a linear array transducer to increase the frame rate 12-fold while maintaining SNR. O'Donnell and Wang [85] combined synthetic aperture imaging with Golay coded excitation for linear array transducer to increase SNR by 14.5 dB in intravascular imaging. These methods used two independent techniques sequentially to improve SNR and lateral resolution. This made the implementation complicated and the reconstruction inefficient.

## 1.4 Thesis Hypothesis and Specific Aims

The hypothesis of this thesis was:

The use of FD-VDS and FD-DC improve the image quality and the computational efficiency compared to TD-VPS in high-frequency ultrasound imaging using single-element focused transducer.

The specific aims of this work were to:

1. Develop two new SAFT image reconstruction methods for imaging with high-frequency single-element focused transducers.
2. Compare the spatial resolution, sidelobe level, SNR, CSR and computational efficiency of the proposed algorithms to TD-VPS using a series of simulated and experimental data.

3. Incorporate coded excitation to further improve the SNR of the developed algorithms without affecting the computational efficiency.

## 1.5 Thesis Organization

The organization of the thesis is as follows:

In Chapter 2, the wavenumber algorithm is derived for a piston transducer. In addition, image quality analysis metrics that are used in Chapter 3 and 4 are explained in details.

In Chapter 3, two new frequency-domain SAFT methods for image reconstruction based on the synthetic aperture radar's wavenumber algorithm and 2D matched filtering techniques are introduced. The image quality and the computational efficiency of the proposed algorithms are compared to the conventional B-mode and TD-VPS imaging techniques using a series of simulations and experiments. This chapter is a journal article published in IEEE Transactions on Ultrasonics, Ferroelectrics, and Frequency Control.

In Chapter 4, a linear frequency modulated chirp coded excitation was used with the proposed frequency-domain SAFT algorithms. The image quality of the proposed methods was compared for both chirp and pulsed excitations using a series of simulations. In addition, the image quality of the proposed algorithms was compared to the conventional B-mode and TD-VPS methods. This chapter is a manuscript submitted for publication in IEEE Transactions on Ultrasonics, Ferroelectrics, and Frequency Control and currently is under review.

In Chapter 5, the discussion and conclusion of the thesis, and future work is presented.

# Chapter 2

## Theory

### 2.1 Wavenumber Algorithm

The wavenumber algorithm was first developed in seismic imaging, where it is known as "range migration" or "omega-k" (or " $\Omega$ - $K$ " or " $\omega$ - $k$ ") algorithm since its key operation takes place in 2D frequency-domain. It was subsequently adopted in synthetic aperture radar (SAR) [86]. The derivation of the wavenumber image reconstruction algorithm for SAR can be found in [48], [54], [87]. In this section, a similar derivation by Stepinski [56] for circular piston transducer is summarized.

#### 2.1.1 Forward Model

The incident pressure wave for a circular piston transducer in the far-field at a general off-axis point  $Q(\vec{R})$  in polar coordinate, as shown in Fig. 2.1, can be expressed as,

$$P_{\text{inc}}(\vec{R}, \omega) = -j\omega\rho v_0 a^2 \frac{\exp(-jk|\vec{R}|)}{|\vec{R}|} \frac{J_1(ka \sin \theta)}{ka \sin \theta}, \quad (2.1)$$

where  $\omega$  is the angular frequency,  $\rho$  is the density of the medium,  $v_0$  is the normal particle velocity at the surface of the transducer,  $k$  is the wavenumber,  $a$  is the radius of the transducer,  $J_1$  is the Bessel function of order one

[56]. The first term represents a frequency-dependent coefficient, the second term represents a spherical spreading wave and the third term represents the angular dependence of the spherical wave. The angular term is also referred to as *jinc* function, which is characterized by a main central lobe and a number of side lobes, as shown in Fig. 2.2.

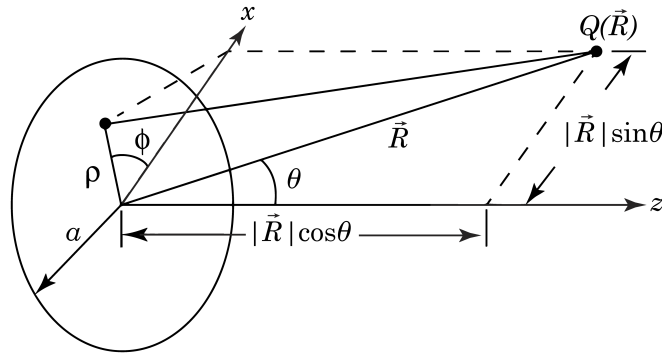


Fig. 2.1. Geometry for calculating the off-axis far-field response of circular transducer. Adopted from [88].

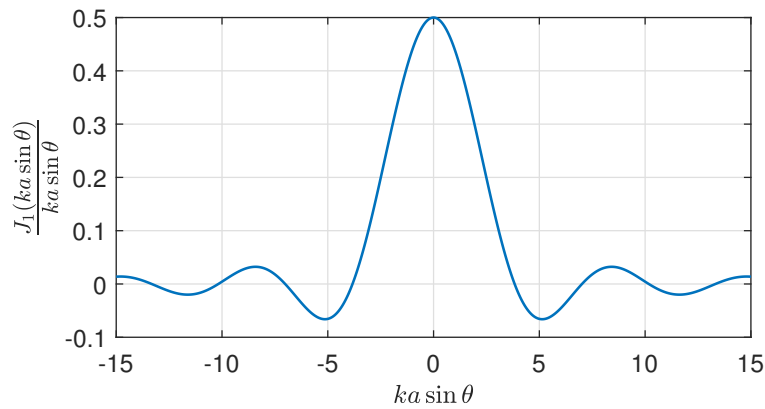


Fig. 2.2. Angular diffraction pattern of a circular plane piston transducer in the far-field.

The incident pressure wave would be scattered back by a point target with elementary surface  $s_e$  at  $Q(\vec{R})$  position. The point target is assumed to be an ideal (broadband) reflector. The pressure integrated over the surface of the transducer  $\langle P_r \rangle(\vec{R}, \omega)$  is the convolution (or product in frequency-domain) of the incident pressure  $P_{\text{inc}}(\vec{R}, \omega)$  and the reflected pressure from

the point target  $P_{\text{refl}}(\vec{R}, \omega)$ ,

$$\begin{aligned} \langle P_r \rangle(\vec{R}, \omega) &= P_{\text{inc}}(\vec{R}, \omega) P_{\text{refl}}(\vec{R}, \omega) \\ &= -\frac{s_e}{2} \omega^2 (\rho v_0 a^2)^2 \frac{\exp(-j2k|\vec{R}|)}{|\vec{R}|^2} \text{jinc}^2(ka \sin \theta). \end{aligned} \quad (2.2)$$

Equation (2.2) is valid for a monostatic configuration where the same transducer is used for the transmission and reception of pressure wave in an isotropic medium. The received signal, assuming that the transducer is a linear time-shift invariant (LTI) system, can be expressed as,

$$S(\vec{R}, \omega) = \langle P_r \rangle(\vec{R}, \omega) H_e(\omega) P(\omega), \quad (2.3)$$

where  $H_e(\omega)$  is the combined transmit and receive electromechanical response of the transducer and  $P(\omega)$  is the excitation signal. By inserting (2.2) into (2.3), the received signal can be expressed as,

$$S(\vec{R}, \omega) = \frac{s_e}{2} (\rho v_0 a^2)^2 \frac{\exp(-j2k|\vec{R}|)}{|\vec{R}|^2} \text{jinc}^2(ka \sin \theta) \omega^2 H_e(\omega) P(\omega). \quad (2.4)$$

Equation (2.4) has five terms. The first term is a constant, the second term represents spherical wave that has travelled to the target and returned, the third term represents the directivity of the transducer, the fourth term represents the electromechanical impulse response of the transducer, and the fifth term represents the excitation signal of the transducer.

If the ROI is confined in the  $xz$ -plane, where  $x$  is the scan (lateral) direction and  $z$  is the axial direction, and assuming  $1/R$  distance compensation is done in the receiver and  $R = \sqrt{x^2 + z^2}$ , then the response of the transducer at position  $x_k$  to a single point scatterer at  $Q(x, 0, z)$  can be expressed as,

$$\begin{aligned} S(\vec{R}, \omega) = S(x_k, \omega) &= \frac{s_e}{2} (\rho v_0 a^2)^2 \exp\left(-j2k\sqrt{z^2 + (x - x_k)^2}\right) \\ &\quad \text{jinc}^2(ka \sin \theta) \omega^2 H_e(\omega) P(\omega), \end{aligned} \quad (2.5)$$

The received signal from an object function  $f(x, z)$  in front of the transducer is obtained by integrating the transducer's response over the whole area,

$$S(x_k, \omega) = \alpha A(k_x) \omega^2 H_e(\omega) P(\omega) \iint_{xz} f(x, z) \exp\left(-j2k\sqrt{z^2 + (x - x_k)^2}\right) dx dz, \quad (2.6)$$

where  $\alpha$  is a constant,  $k_x = k \sin \theta$ , and  $A(k_x) = \text{jinc}^2(ka \sin \theta) = \text{jinc}^2(k_x a)$ .

Using the principle of stationary phase [48], [87], the 1D Fourier transform of (2.6) along the  $x$ -direction can be expressed as,

$$S(k_x, \omega) = \alpha A(k_x) \omega^2 H_e(\omega) P(\omega) \iint_{xz} f(x, z) \exp\left(-j\sqrt{4k^2 - k_x^2}z\right) \exp(-jk_x x) dx dz. \quad (2.7)$$

If a new set of coordinates is defined such that,

$$k_z(k_x, \omega) \equiv \sqrt{4k^2 - k_x^2}, \quad (2.8)$$

then  $S(k_x, \omega)$  can be expressed as,

$$S(k_x, \omega) = \alpha A(k_x) \omega^2 H_e(\omega) P(\omega) F(k_x, k_z). \quad (2.9)$$

As shown in the above equation, the coordinates of  $S(k_x, \omega)$ ,  $A(k_x)$ ,  $H_e(\omega)$  and  $P(\omega)$  are different from  $F(k_x, k_z)$ . Fig. 2.3 shows the distribution of data in  $(k_x, \omega)$  and  $(k_x, k_z)$  coordinates. The coordinate transformation defined in (2.8) is known as the Stolt transformation (or Stolt migration in seismology [89], [90]), which transforms the data from  $(k_x, \omega)$  into  $(k_x, k_z)$  domains, and it is denoted by  $\mathcal{S}\{\cdot\}$ . The above convolution model assumes a LTI system. However, ultrasound imaging systems are spatially variant. Stolt transformation compensates the spatially variant nature of ultrasound imaging [91]. Stolt transformation improves focusing by performing amplitude and phase adjustments to correct for the effects of spreading of ray paths as the waves propagate [90]. This is similar to the time-domain delay-and-sum beamforming which is extensively used in ultrasound imaging.

In general, the forward model is complicated and several assumptions have been made to simplify the model. The ROI is assumed to be in the far-field of the transducer. Total scattered field is assumed to be the superposition of individual scattered field by each point and multiple scattering and shadowing effects are ignored. Speed of sound is assumed to be constant in the medium and shear wave modes are ignored. In addition, the transducer is assumed to be stationary between transmission and reception.

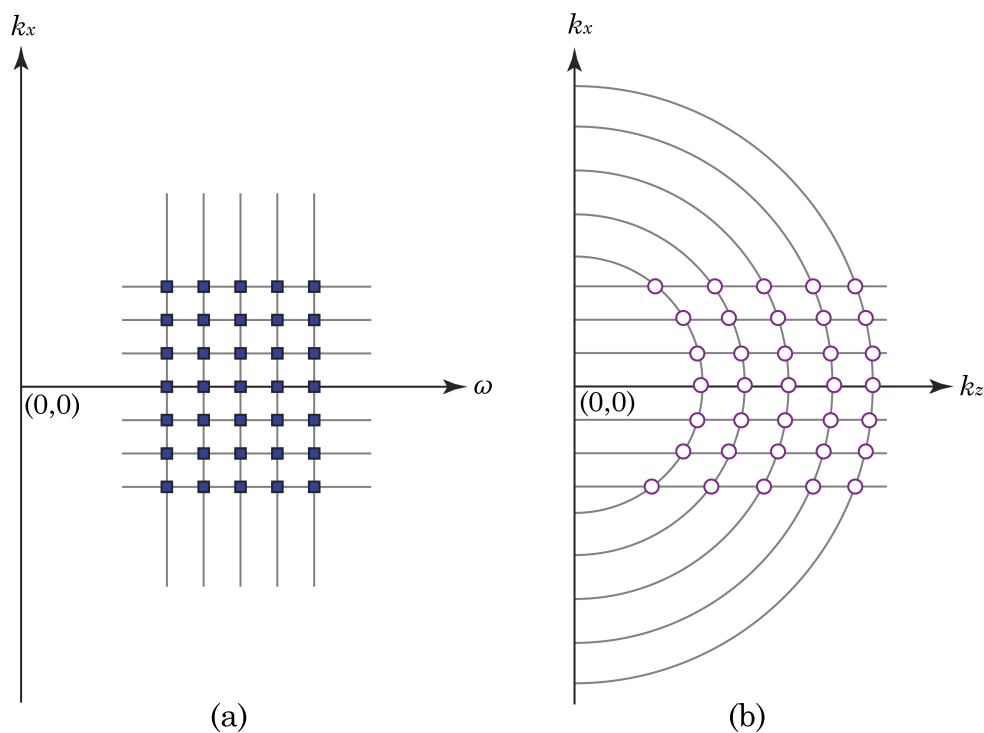


Fig. 2.3. Distribution of the data (a) in  $(k_x, \omega)$  and (b)  $(k_x, k_z)$  coordinates. Adopted from [87].

### 2.1.2 Image Reconstruction

The wavenumber algorithm starts by applying 2D Fourier transform to received data  $s(x_k, t)$  to transform the data into spatio-temporal frequency-domain  $S(k_x, \omega)$ . Image reconstruction is performed by using matched filter

and Stolt transformation as follows,

$$\hat{F}(k_x, k_z) = \mathcal{S} \left\{ \exp \left[ j(\sqrt{4k^2 - k_x^2} - 2k)z_c \right] A^*(k_x)\omega^2 H_e^*(\omega) P^*(\omega) S(k_x, \omega) \right\}, \quad (2.10)$$

where  $z_c$  is the perpendicular distance from the transducer to the midpoint of the ROI and asterisk (\*) denotes complex conjugate. The factor  $\exp[\cdot]$  is a phase shift for adjusting the origin of the data to be centred at  $z_c$ . The final step of the wavenumber algorithm is to apply inverse 2D Fourier transform to the reconstructed image to transform the image into spatial-domain  $\hat{f}(x, z)$ .

Equation (2.10) is considered elegant [54] since it compensates the diffraction effect of the transducer in the far-field, the electromechanical impulse-response of the transducer and the excitation signal of the transducer. In addition, Stolt transformation improves focusing by compensating space-variance nature of the received data [90], [91].

### 2.1.3 Stolt Transformation

As shown in Fig. 2.3(a), the received data  $S(k_x, \omega)$  is evenly spaced samples on a rectangular grid in  $(k_x, \omega)$  domain. The wavenumber image reconstruction maps the received data from  $(k_x, \omega)$  domain into  $(k_x, k_z)$  domain using (2.8). Due to the nonlinear nature of the mapping into the  $(k_x, k_z)$  domain, the resultant data is unevenly spaced in the  $k_z$  domain, as shown in Fig. 2.3(b). In order to generate the reconstructed image in spatial-domain, inverse FFT requires the data to be on a rectangular grid. The data can be mapped into a rectangular grid by 1D interpolation in the  $k_z$  domain. Fig. 2.4 illustrates the distribution of data before and after interpolation. The use of an interpolator to map the data on a rectangular grid is the essence of Stolt transformation.

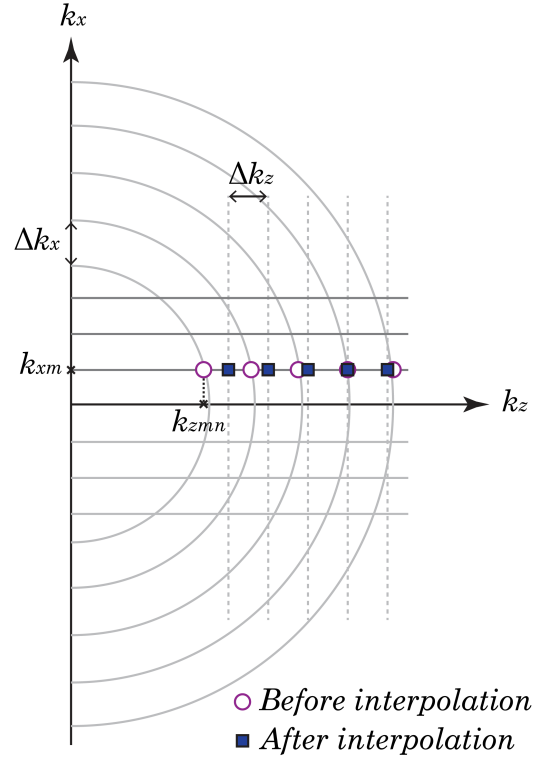


Fig. 2.4. Distribution of discrete data before and after interpolation. Adopted from [48].

The interpolation can be carried out via a windowed (tapered) sinc as following [48],

$$F(k_z, k_{xm}) \approx \sum_{|k_z - k_{zm}| \leq N_s \Delta k_z} F(k_{zm}, k_{xm}) h_w(k_z - k_{zm}), \quad (2.11)$$

where

$$h_w(k_z) = \begin{cases} h(k_z)w(k_z) & \text{for } |k_z| \leq N_s \Delta k_z, \\ 0 & \text{otherwise.} \end{cases} \quad (2.12)$$

The parameter  $N_s$  is a constant chosen by the user which denotes the half-number of sinc side lobes used for interpolation,  $h(k_z)$  is a sinc interpolating function, and  $w(k_z)$  is a Hamming window function (it can be any window function).  $h(k_z)$  and  $w(k_z)$  are defined as,

$$h(k_z) = \text{sinc} \left( \frac{k_z}{\Delta k_z} \right), \quad (2.13)$$

$$w(k_z) = \begin{cases} 0.54 + 0.46 \cos\left(\frac{\pi k_z}{N_s \Delta k_z}\right) & \text{for } |k_z| \leq N_s \Delta k_z, \\ 0 & \text{otherwise.} \end{cases} \quad (2.14)$$

The support of  $h_w(k_z)$  or  $w(k_z)$  in the  $k_z$  domain is  $k_z \in [-N_s \Delta k_z, N_s \Delta k_z]$ .

## 2.2 Image Quality Analysis

The performance of ultrasound image quality is usually characterized by the spatial resolution, the contrast, and the signal-to-noise ratio.

### 2.2.1 Spatial Resolution

Spatial resolution is typically measured from the images of point targets [i.e., point spread function (PSF)]. The size of the PSF is measured by full-width-at-half-maximum (FWHM) in the axial and lateral directions for the quantification of axial and lateral resolutions, respectively. However, as shown in Fig. 2.5, PSF usually have asymmetrical shapes and the values of FWHM measurement varies depending on where the measurement is taken. Moreover, PSF could be affected by multiple peaks due to strong sidelobes, edge wave (i.e., a wave that originates at the edge of the transducer's face and spreads out toroidally as it propagates [92]) or reverberation. Thus, FWHM measurement could be ambiguous and subjective.

A more objective way to measure the overall spatial resolution is to measure the size of the PSF by the area enclosed within the contour area. The spatial resolution can be measured by  $-6$  dB contour area and sidelobe level can be measured by  $-24$  dB contour area, as shown in Fig. 2.5.

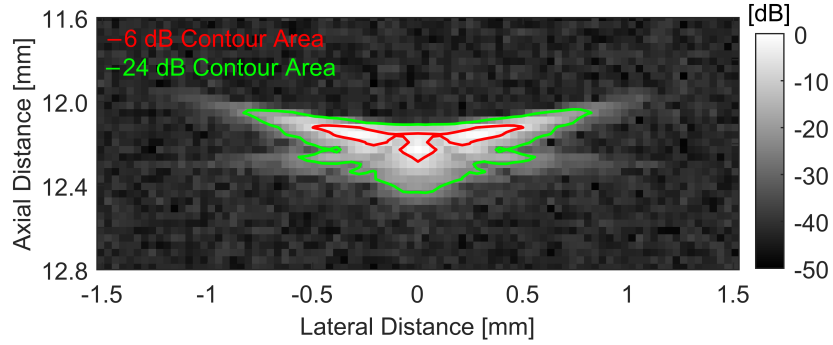


Fig. 2.5. Point spread function (PSF) with  $-6$  dB and  $-24$  dB contour areas for the measurement of spatial resolution and sidelobe level, respectively.

## 2.2.2 Signal-to-Noise Ratio

The signal-to-noise ratio (SNR) can be measured by the ratio of signal root-mean-square (RMS) and noise RMS, as following [70],

$$\text{SNR} = 10 \log_{10} \left( \frac{\text{signal RMS}}{\text{noise RMS}} \right), \quad (2.15)$$

where the signal can be the image data (without logarithmic compression) inside the  $-6$  dB contour area of a PSF and noise can be the image data in a rectangular window in the background at the same axial distance that does not include sidelobes, as shown in Fig. 2.6.

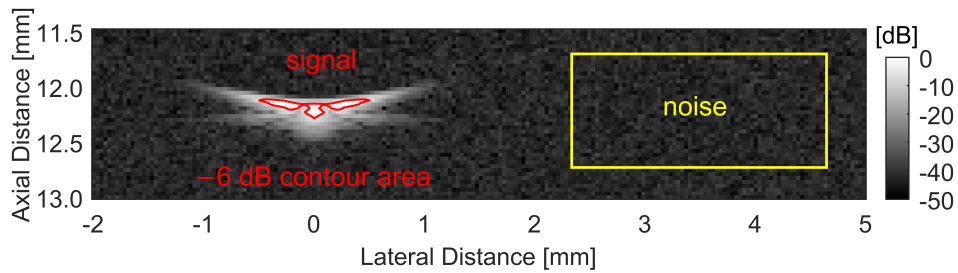


Fig. 2.6. Measurement of the signal-to-noise ratio. The signal is the image data inside the  $-6$  dB contour area and the noise is image data inside a rectangular window in the background.

### 2.2.3 Contrast-to-Speckle Ratio

Tissue contrast can be measured by the contrast-to-speckle ratio (CSR) as following [93],

$$\text{CSR} = \frac{|S_{\text{out}} - S_{\text{in}}|}{\sqrt{\sigma_{\text{out}}^2 + \sigma_{\text{in}}^2}}, \quad (2.16)$$

where  $S_{\text{in}}$  and  $\sigma_{\text{in}}$  are the mean and standard deviation of the image data (magnitude of the reconstructed image prior to logarithmic compression) inside a region of the cyst, respectively, and  $S_{\text{out}}$  and  $\sigma_{\text{out}}$  are the mean and standard deviation of the image data the same-sized region outside the cysts at the same axial distance, respectively. An example is shown in Fig. 2.7. The above equation shows that detectability increases with increasing cyst contrast while it decreases with speckle variance.

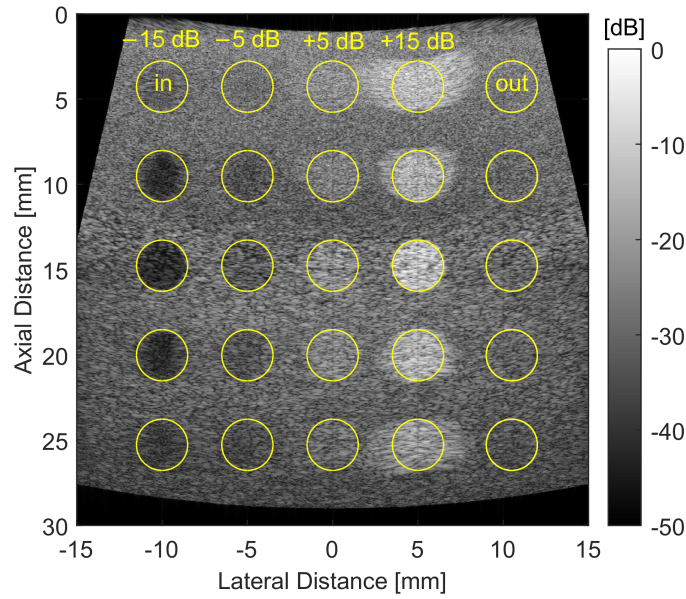


Fig. 2.7. Measurement of the contrast-to-speckle ratio for quantifying tissue contrast between a region inside of a cyst and a region outside the cyst.

### 2.2.4 Clutter Energy to Total Energy Ratio

The contrast resolution of an anechoic object, which describes the ability of the imaging system to detect an anechoic object in a homogeneous scattering

medium, can be measured by clutter energy to total energy ratio (CTR) [94], [95]. CTR is measured by the ratio of the energy of the signal outside a circular region  $R$  with  $5\lambda$  diameter centred on a PSF at  $(x_0, z_0)$  to the total energy of the signal as following,

$$\text{CTR}(x_0, z_0) = 10 \log_{10} \left( \frac{\int_{x,z \notin R} f^2(x_0, z_0, x, z) dx dz}{\int f^2(x_0, z_0, x, z) dx dz} \right). \quad (2.17)$$

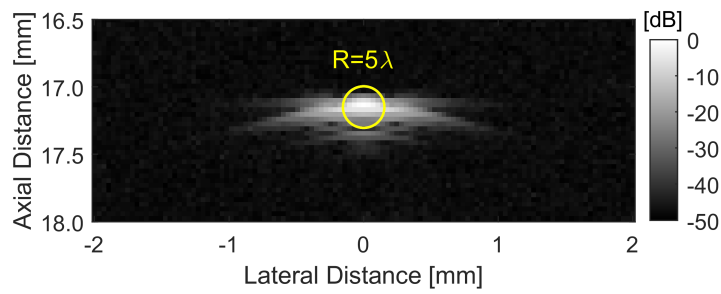


Fig. 2.8. Measurement of the clutter energy to total energy ratio, that is the ratio of the energy of the signal outside a circle of  $5\lambda$  diameter to the total energy of the signal.

## Chapter 3

# Efficient Frequency-Domain Synthetic Aperture Focusing Techniques for Imaging with a High-Frequency Single-Element Focused Transducer

---

*This chapter is a journal article published in IEEE-T-UFFC (E. Shaswary, J. Tavakkoli, and J. C. Kumaradas, Efficient frequency-domain synthetic aperture focusing techniques for imaging with a high-frequency single-element focused transducer, vol. 66, no. 1, pp. 57-70, Jan. 2019, DOI: 10.1109/TUFFC.2018.2881726).*

*In this chapter, the acronyms for TD-SAFT-VPS, FD-SAFT-VS and FD-SAFT-DE has been changed from the journal article to TD-VPS, FD-VDS and FD-DC, respectively, for the sake of consistency with the rest of the thesis.*

## 3.1 Abstract

Synthetic aperture focusing techniques (SAFT) make the spatial resolution of the conventional ultrasound imaging from a single-element focused transducer more uniform in the lateral direction. In this work, two new frequency-domain (FD-SAFT) algorithms are proposed, which are based on the synthetic aperture radars wavenumber algorithm, and 2-D matched filtering technique for the image reconstruction. The first algorithm is the FD-SAFT virtual source (FD-VDS) that treats the focus of a focused transducer as a virtual source having a finite size and the diffraction effect in the far-field is taken into consideration in the image reconstruction. The second algorithm is the FD-SAFT deconvolution (FD-DC) that uses the simulated point spread function of the imaging system as a matched filter kernel in the image reconstruction. The performance of the proposed algorithms was studied using a series of simulations and experiments, and it was compared with the conventional B-mode and time-domain SAFT (TD-VPS) imaging techniques. The image quality was analyzed in terms of spatial resolution, sidelobe level, signal-to-noise ratio (SNR), contrast resolution, contrast-to-speckle ratio, and *ex vivo* image quality. The results showed that the FD-VDS had the smallest spatial resolution and FD-DC had the second smallest spatial resolution. In addition, FD-DC had generally the largest SNR. The computation run time of FD-VDS and FD-DC, depending on the image size, was lower by 4 to 174 times and 4 to 189 times, respectively, compared to the TD-SAFT-virtual point source.

## 3.2 Introduction

High Frequency ultrasound imaging, which typically operates 20-100 MHz [8], is used on skin [36], [96], [97], eye [98]–[100], vascular [99], [101], [102], and small animals [103]–[105]. It provides high spatial resolution to the expense of limited depth of penetration. Conventional ultrasound imaging, in the frequency range of 2-15 MHz, almost entirely relies on array transducers, which offer high frame rates and larger depth of field than

single-element focused transducers [8], [65]. However, fabrication of high-frequency arrays is very challenging since the element pitch (i.e., the distance between the centre of two adjacent elements) must be smaller than 1 wavelength for linear arrays and 0.5 wavelengths for phased arrays, in order to avoid grating lobes [8]. Even though linear array transducers up to 50 MHz have recently become available from FUJIFILM Visualsonics (Toronto, ON, Canada), their pitch is greater than 1 wavelength [8], [106]. The vast majority of high-frequency ultrasound imaging is still carried out using single-element focused transducers since they are technically simple and affordable, and high frame rates [up to 240 frames/s from VEVO 770 scanner (FUJIFILM VisualSonics Inc.)] have been achieved using fast mechanical scanning [8], [65], [104]. A few notable examples of high-frequency clinical scanners that use single-element focused transducers are: Quantel Medical Inc. (Cournon d'Auvergne, France), ArcScan Inc. (Golden, CO, USA), Sonomed Escalon (New Hyde Park, NY, USA), Ellex Medical Lasers Ltd. (Adelaide, Australia), Tomey Corp. (Aichi, Japan) and DGH Technology Inc. (Exton, PA, USA) for imaging of the eye, and Cortex Technology ApS (Hadsund, Denmark), Longport Inc. (Chadds Ford, PA, USA), and Atys Medical (Soucieu-en-Jarrest, France) for imaging of the skin.

A major issue associated with using single-element focused transducer is the short depth of field which leads to invariant and anisotropic spatial resolution. The spatial resolution of ultrasound depends on several parameters including the central frequency, bandwidth, and the size of the active aperture of the transducer [1]. The spatial resolution in the lateral direction is optimal at the focal distance, and it decreases away from the focal distance due to the diffraction effects of the beam. The drawback of short depth of field can be solved using synthetic aperture imaging techniques.

Synthetic aperture imaging techniques can be used to make the spatial resolution of the ultrasound imaging less spatially variant [48]. In synthetic aperture imaging, the effect of a long aperture is mathematically synthesized by moving a smaller aperture. A longer aperture provides images with improved lateral resolution. Numerous synthetic aperture image reconstruction algorithms, which are also referred to as synthetic aperture

focusing techniques (SAFT), have been proposed in both time and frequency domains. Synthetic aperture radar (SAR) and synthetic aperture sonar reconstruction algorithms have been mainly implemented in the frequency domain [48], [54]–[56], which are computationally more efficient as they are based on the fast Fourier transform (FFT). On the other hand, industrial and medical ultrasound imaging fields have generally relied on the time-domain (TD) methods [30], [31], [52], [56]–[59], which are based on well-known delay-and-sum (DAS) beamforming method. The SAFT using DAS is computationally intensive since it involves a large number of operations [68]. As computational power has increased, SAFT using DAS for ultrasound imaging has received renewed attention and several techniques have been proposed for various applications and transducer geometries. In particular, SAFT for linear array and high-frequency single element focused transducers are more common than other type of transducers as they are used in a wide range of biomedical applications.

Although SAFT for array transducers have been extensively studied and several implementations have been reported, such as synthetic transmit aperture [30], [31], [107], multi element synthetic transmit aperture [58], [70], [75]–[77], virtual source [30], [62], [78], [80], and sequential beamforming for synthetic aperture imaging [68], [74], this paper focuses on single-element focused transducers. For single-element focused transducers, SAFT is typically implemented using virtual source techniques. Passmann and Ermert [61] were the first ones who introduced the concept of virtual source SAFT in ultrasound imaging, where the focal point of the transducer was considered as a virtual transducer [also known as a virtual point source (VPS)]. It is assumed that the virtual point source emits a spherical wave propagating toward and away from the transducer. In this technique, the SAFT algorithm is implemented in the time domain, and it was found to increase the penetration depth and depth of focus from a high-frequency (100 MHz) strongly focused single-element transducer [36]. Subsequently, Frazier and O'Brien [62] examined the performance of virtual point source SAFT in terms of lateral resolution, sidelobe level, and signal-to-noise ratio (SNR). It was reported that improved lateral resolution beyond the focal region of the transducer with acceptable SNR can be achieved and that

the sidelobes can be reduced by using source apodization. Nikolov [30] also examined the application of virtual point source SAFT in 3-D ultrasound imaging using a linear array transducer. Li *et al.* [63] and Opretzka *et al.* [64] also implemented virtual point source SAFT in the time domain for imaging with a high-frequency single-element focused transducer. They found that improved lateral and axial resolutions beyond the focus of the transducer with increased SNR can be achieved. In addition, Opretzka *et al.* [65] combined their method with spatial compounding improved contrast and reduced speckle and acoustic noises. However, the computational time of their algorithm was significantly higher (by a factor of about 513) compared to conventional time-domain SAFT (TD-SAFT).

Frequency-domain SAFT (FD-SAFT) based on spatial-temporal matched filtering was first introduced in ultrasound imaging by Ermert and Karg [66]. For single-element transducers, several FD-SAFT implementations have been proposed [56], [60], [67]. Stepinski [56] proposed an FD-SAFT algorithm for industrial applications using a physical circular flat piston transducer. This was a modified version of the well-known wavenumber algorithm in SAR [48], [54], and it was based on the convolution model of an imaging system. The algorithm took into account the electromechanical impulse response and the diffraction effects of the transducers using a far-field approximation. Moreover, Stepinski compared the performance of FD-SAFT and TD-SAFT algorithms, where it was reported that FD-SAFT outperforms TD-SAFT in terms of axial and lateral resolutions, and sidelobe levels. Vos *et al.* [68] presented a virtual point source FD-SAFT algorithm for low-frequency (1 MHz) single-element focused and linear array transducers, which was based on the Stolt transformation. The performance of the algorithm was compared with a virtual point source TD-SAFT algorithm (known as sequential beamforming [74]), and it was reported that it yields similar lateral resolution while being computationally more efficient. However, the effects of the electromechanical impulse response, the excitation pulse, and the transducer diffraction were not taken into account, which would reduce its image quality. Thus, even though virtual point source FD-SAFT method has been shown to be more efficient compared to the virtual

point source TD-SAFT method, its image quality has not better than the virtual point source TD-SAFT.

For focused transducer, virtual point source TD-SAFT has provided improved image quality over conventional B-mode (CONV), but its performance has been much slower, resulting in not being used in clinical applications due to the lack of real-time capability. Even though the use of graphics processing units have been suggested to address the high computation demand of TD-SAFT [68], [108]–[110], the use of efficient SAFT algorithms is still preferred since they can provide higher frame rates and they can be implemented in portable scanners and 3-D scanning methods. To this end, Vos *et al.* [68] have improved the performance while providing similar image quality compared to virtual point source TD-SAFT. For unfocused single-element transducer, Stepinski [56] has improved the image quality over TD-SAFT. Thus, for the single-element focused transducer, SAFT with improved performance and image quality over virtual point source TD-SAFT has not been presented.

In this work, we propose two new FD-SAFT algorithms that are based on a 2-D matched filtering technique. The first algorithm is based on a virtual source (FD-VDS) method and the second algorithm is based on a FD deconvolution (FD-DC) method. FD-VDS is similar to the algorithm presented by Stepinski [56], which was implemented for flat circular transducers, but the FD-VDS approach treats the focal point of a focused transducer as a virtual flat circular source. Since the finite size of the focal zone is considered, the directivity pattern (also known as radiation or beam pattern) of the transducer is taken into account in the image reconstruction. The directivity pattern is a far-field characterization of a transducer, which consists of a central mainlobe and several sidelobes [111]. The diffraction effect of the single-element focused transducers significantly affects the quality of SAFT image if it is not properly taken into the account. FD-DC uses the simulated point spread function (PSF) of the imaging system, which fully characterizes the imaging system, as a filter kernel in matched filtering. It is demonstrated in this work that the proposed algorithms improve image quality and reduce computational time compared to the virtual point source TD-SAFT algorithm.

## 3.3 Theory

### 3.3.1 Frequency-Domain Virtual Source SAFT

The origin of FD-SAFT algorithms can be found in the wavefront reconstruction theory or holography [48]. The wavefront reconstruction is based on the Fourier decomposition of a Green's function, which represents the impulse response of an imaging system.

In SAFT, the data acquisition using a single-element transducer is done in the same way as conventional pulse-echo imaging, where the transducer mechanically scans the region of interest (ROI). At each scan position, a 1-D signal is acquired, which are stacked to form a 2-D ultrasonic reflectivity map of the insonified ROI,  $s(x, t)$ . The recorded echo signal is expressed in FD as a convolution model as [56],

$$S(k_x, \omega) = \alpha A(k_x) \omega^2 H_e(\omega) F(k_x, k_z), \quad (3.1)$$

where  $k_x$  and  $k_z$  are the wavenumbers in the  $x$ -direction (the lateral or scan direction) and  $z$ -direction (the axial direction), respectively,  $\omega$  are the temporal frequencies of the signal,  $\alpha$  is a constant,  $A(k_x)$  is the far-field directivity function,  $H_e(\omega)$  is the combined transmit and receive electromechanical impulse response of the transducer, and  $F(k_x, k_z)$  is the objects reflectivity function. FD-SAFT image reconstruction solves the inverse problem using matched filtering to represent  $F(k_x, k_z)$ . The wavenumber algorithm, which was initially introduced in SAR [48], [54], was derived by Stepinski [56] for ultrasound imaging where the reconstructed image  $\hat{F}(k_x, k_z)$  is expressed as,

$$\hat{F}(k_x, k_z) = \mathcal{S} \left\{ \exp \left[ j(\sqrt{4k^2 - k_x^2} - 2k)z_c \right] A^*(k_x) \omega^2 H_e^*(\omega) S(k_x, \omega) \right\}, \quad (3.2)$$

where  $z_c$  is the perpendicular distance from the transducer to the midpoint of the ROI,  $k = \omega/c$  and asterisk represents complex conjugate.  $\mathcal{S}\{\cdot\}$  is the Stolt transformation, which transforms  $(k_x, \omega)$  into  $(k_x, k_z)$  coordinates defined by:  $k_z(k_x, \omega) = \sqrt{4k^2 - k_x^2}$  (for details, see [48][16]). Equation (2.2),

takes into account the far-field diffraction effects and the electro-mechanical impulse response of the transducer. The initial step of the process is to split the recorded data,  $s(x_n, t)$ , at the focal distance,  $z_f$ , into two regions, namely, the prefocal,  $s_{\text{pre}}(x_n, t) = s(x_n, t_{\text{pre}})$ ,  $t_{\text{pre}} \in \{0 \cdots (2z_f/c_0)\}$ , and postfocal,  $s_{\text{post}}(x_n, t) = s(x_n, t_{\text{post}})$ ,  $t_{\text{post}} \in \{(2z_f/c_0) \cdots (2z/c_0)\}$ , regions. The idea of distinguishing the prefocal and postfocal regions was initially introduced by Nayebi [112] and subsequently by Vos *et al.* [68] and Ameri [113]. The prefocal data,  $s_{\text{pre}}(x_n, t) \rightarrow s_{\text{pre}}(x_n, -t)$ , the electromechanical impulse response,  $h_{\text{pre}}(t) \rightarrow h_e(-t)$ , and the excitation pulse,  $p_{\text{pre}}(t) \rightarrow p(-t)$ , are reversed in the axial direction. A 2-D FFT is used to transform  $s_{\text{pre}}(x_n, -t)$ ,  $s_{\text{post}}(x_n, t)$ ,  $h_{\text{pre}}(-t)$ ,  $h_{\text{post}}(t)$ ,  $p_{\text{pre}}(-t)$ , and  $p_{\text{post}}(t)$  from the spatial-temporal domain to  $S_{\text{pre}}(k_x, \omega)$ ,  $S_{\text{post}}(k_x, \omega)$ ,  $H_{\text{pre}}(\omega)$ ,  $H_{\text{post}}(\omega)$ ,  $P_{\text{pre}}(\omega)$ , and  $P_{\text{post}}(\omega)$ , respectively, in the frequency domain. The far-field directivity pattern of the virtual source was assumed to be  $A(k_x) = \text{jinc}^2(k_x a)$ , where  $a$  is the radius of the flat circular virtual source that can be determined from the simulated beam profile. A schematic of the FD-VDS is shown in Fig. 3.1, which shows the finite size of the virtual source. The image reconstruction is carried out in the prefocal and postfocal regions as follows:

$$F_{\text{pre}}(k_x, k_z) = \mathcal{S} \left\{ \exp \left[ j \sqrt{(4k^2 - k_x^2) - 2k} z_c \right] A^*(k_x) \omega^2 H_{\text{pre}}^*(\omega) P_{\text{pre}}^*(\omega) S_{\text{pre}}(k_x, \omega) \right\}, \quad (3.3)$$

$$F_{\text{post}}(k_x, k_z) = \mathcal{S} \left\{ \exp \left[ j \sqrt{(4k^2 - k_x^2) - 2k} z_c \right] A^*(k_x) \omega^2 H_{\text{post}}^*(\omega) P_{\text{post}}^*(\omega) S_{\text{post}}(k_x, \omega) \right\}, \quad (3.4)$$

where  $F_{\text{pre}}(k_x, k_z)$  and  $F_{\text{post}}(k_x, k_z)$  are the spatial frequency domain image functions in the prefocal and postfocal regions, respectively. The inverse 2-D FFT is used to transform  $F_{\text{pre}}(k_x, k_z)$  and  $F_{\text{post}}(k_x, k_z)$  from frequency domain to spatial domain,  $f_{\text{pre}}(x, z)$  and  $f_{\text{post}}(x, z)$ , respectively. Then, the prefocal region is flipped in the axial direction to its original orientation,  $f_{\text{pre}}(x, z)$ , before stitching it with  $f_{\text{post}}(x, z)$  to get the resultant,  $f_{\text{vs}}(x, z)$  as the reconstructed FD-VDS image.

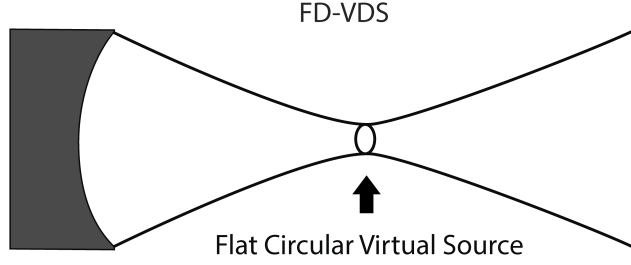


Fig. 3.1. Schematic FD-VDS.

### 3.3.2 Frequency-Domain Deconvolution SAFT

An image,  $S(k_x, \omega)$ , can be modelled as a convolution of the systems PSF( $k_x, \omega$ ), and objects reflectivity function,  $F(k_x, k_z)$  in FD as,

$$S(k_x, \omega) = F(k_x, k_z(k_x, \omega))\text{PSF}(k_x, \omega). \quad (3.5)$$

The PSF represents the response of the system to a point scatterer, and it takes into account all the characteristics of the imaging system, including the diffraction effects, electromechanical impulse response, and the excitation pulse of the system. However, the PSF depends on the relative position between the transducer and point scatterer. As it is shown in the results section, for a single-element focused transducer, the PSF at the focal point of the transducer is distorted the least because the diffraction effect at that position is minimal. Thus, for a focused transducer, the PSF at the focal point is more appropriate. In this work, we propose a PSF function expressed as,

$$\text{PSF}(k_x, \omega) = P(\omega)H_e(\omega)D(k_x, \omega), \quad (3.6)$$

where  $P(\omega)$  is the excitation pulse,  $H_e(\omega)$  is the electromechanical impulse response, and  $D(k_x, \omega)$  is the diffraction effects of the transducer.

In this work, the wavenumber algorithm is implemented by using the PSF of the system as a filter kernel in the matched filtering operation. The PSF of the system can be either simulated or determined experimentally. The former is preferred since it is not corrupted by noise. A simulated PSF can be determined by using a simulation software, such as Field II [114], to acquire RF data from a region with a point scatterer at the focal distance of

the transducer using the transducer's parameters and response (see Section 2.4 for how a transducer response can be determined experimentally). The image reconstruction is performed by deconvolving the simulated PSF of the system from the recorded RF echo data via matched filtering, and then applying the Stolt transformation as,

$$F(k_x, k_z) = \mathcal{S} \{ \text{PSF}^*(k_x, \omega) S(k_x, \omega) \}. \quad (3.7)$$

We refer to this algorithm as the FD deconvolution SAFT (FD-DC). In the initial step, the experimentally recorded echo signal and the simulated PSF are transformed into FD via 2-D FFT. FD-DC is a simple and efficient image reconstruction technique. The simulated PSF can be calculated once for a specific transducer and excitation source, and then reused each time the image reconstruction is performed. It should be noted that the FD-DC method is different from established conventional and blind deconvolution methods, such as those introduced in [4], [115], [116]. It is based on the wavenumber algorithm, which performs the Stolt transformation following the inversion operation.

### 3.3.3 Time-Domain SAFT

TD-SAFT is based on DAS beamforming methods. TD-SAFT assumes that the transducer is a point source, which emits spherical waves. The image reconstruction is done by delaying the recorded echo signals according to the relative positions of the image pixel and the transducer, which is then followed by a coherent summation. Each point  $(x, z)$  in the image is brought into focus by applying appropriate time delays to the recorded echo data  $s(x_n, t)$  for all the transducer positions  $x_n (n \in \{0 \cdots L-1\})$  in the synthetic aperture and then performing summation, as follows [64],

$$f_{\text{TD}}(x, z) = \sum_{n=0}^{L-1} s \left( x_n, \frac{2}{c_0} \sqrt{(x - x_n)^2 + z^2} \right), \quad (3.8)$$

where  $c_0$  is the speed of sound and  $f_{\text{TD}}(x, z)$  is the reconstructed TD-SAFT image.

The TD virtual point source SAFT (TD-VPS) treats the focus of the transducer as a point source where (3.8) is applied in the prefocal and postfocal regions separately. In the prefocal region, the recorded echo data are flipped in the axial direction and (3.8) is applied. In the postfocal region, (3.8) is applied to the recorded echo data without changing the orientation of the data. After applying (3.8), the prefocal region is flipped back to its original orientation before joining it with the postfocal region. In addition, the image intensity of each point can be normalized by dividing the square root of the number of scanlines used at each point (for details, see [78], [117]).

### **3.4 Methods**

The image quality of the proposed FD-VDS and FD-DC methods was evaluated using a series of simulated and experimental radio frequency (RF) data. The image quality was measured quantitatively in terms of spatial resolution (measured by contour area above  $-6$  dB), sidelobe level (measured by contour area above  $-24$  dB), SNR, contrast resolution [measured by clutter energy to total energy ratio (CTR)] and contrast-to-speckle ratio (CSR), and qualitatively in terms of the appearance of boundaries and structures. Spatial resolution and sidelobe level were also measured by measuring the width of the point scatterers at  $-6$  and  $-24$  dB, respectively, (for results refer to the supplementary content in Appendix A). A high-frequency commercial ultrasound scanner VEVO 770 (FUJIFILM VisualSonics Inc., Toronto, ON, Canada) with a 25-MHz central frequency, 7-mm diameter, 15-mm focal length, and 2.7-mm depth-of-field probe (Model# RMV-710B) was used to acquire RF data. The transducer had a bandwidth of 12-38 MHz, and it was capable of performing fast mechanical sector scanning. All simulated data were generated using Field II simulation software [114], [118] with an experimentally measured transducer response. The response of the transducer was determined by placing a flat plexiglass reflector at the focal distance of the transducer and the reflected signal was recorded when the transducer was excited by a single cycle pulse. The response of the transducer represented the electromechanical impulse response of the transducer during emission and reception of an excitation pulse [119].

The sampling frequency of the RF signal for SAFT image reconstruction must satisfy the Nyquist sampling criterion to avoid aliasing. The sampling frequency ( $f_s$ ) in the axial direction must satisfy,  $f_s \geq 2f_{\max}$ , where  $f_{\max}$  is the maximum frequency in the bandwidth of the transducer [48]. The sampling criterion in the lateral (scan) direction for a focused transducer is,  $\Delta_x \geq c_0/(4f_{\max} \sin(\phi_d))$ , where  $c_0$  is the speed of sound in water and  $\phi_d$  is the divergence angle of the transducer that is defined as,  $\phi_d = \tan^{-1}(D/2z_f)$ , where  $D$  and  $z_f$  are the diameter and focal length of the transducer, respectively. For a  $f_{\max}$  of 38 MHz,  $\Delta_x \geq 0.043$  mm. All image characterization was carried out in MATLAB version 8.5 (The MathWorks Inc., Natick, MA, USA). The performance of the new algorithms was compared to CONV and TD-VPS reconstructions. The CONV reconstruction was done by taking the Hilbert transform of the acquired RF data and then taking its absolute value. The dynamic range of the reconstructed images was adjusted by a logarithmic compression function as,

$$f_{\text{db}}(x, z) = 20 \log_{10} \left( 10^{\left(\frac{-R}{20}\right)} + \left(1 - 10^{\left(\frac{-R}{20}\right)}\right) \left( \frac{f(x, z) - \min(f(x, z))}{\max(f(x, z)) - \min(f(x, z))} \right) \right), \quad (3.9)$$

where  $f(x, z)$  was the original image and  $R$  was the range of compression (in dB).

### 3.4.1 Simulations

Two different virtual phantoms were used to analyze the image quality in this study. The first virtual phantom with point scatterers placed in water was used for the quantification of spatial resolution. The values of the simulation parameters are shown in Table 3.1. White Gaussian noise mimicking electronic noise was added to the generated RF data prior to image reconstruction, where its magnitude and spectrum of the noise was matched to the RF data that was recorded experimentally. The point scatterers were distributed from 2 to 29.5 mm from the top surface of the phantom in increments of 2.5 mm in the axial direction. The generated RF data were

then used to reconstruct CONV, TD-VPS, FD-VDS, and FD-DC images. The area enclosed by the  $-6$  dB contour of each point scatterer in the reconstructed images was measured for the quantification of the spatial resolution. The area enclosed by the  $-24$ -dB contour was measured for the quantification of the sidelobes. In the literature, the size of the point scatterer is typically measured by the full-width-at-half-maximum (FWHM) in the axial and lateral directions. However, the images of point scatterer typically have asymmetrical shapes and magnitude of the FWHM measurements varies depending on where it is measured. In addition, they could occasionally have multiple peaks (due to strong sidelobes, edge wave or reverberation), which could make the FWHM measurement ambiguous and subjective. Thus, in this work, the overall spatial resolution was measured by the contour area, which is a more objective way to measure the size of the point scatterer. For comparison purposes, measurements of FWHM are included in the supplementary content in Appendix A.

TABLE 3.1: Simulation parameters for the point scatterer and tissue-mimicking phantoms.

Parameter	Point Scatterer Virtual Phantom	Tissue-Mimicking Virtual Phantom
Scan type	Sector	Sector
Speed of sound	1500 m/s	1540 m/s
Attenuation coefficient	0.0022 dB/(cm MHz)	0.5 dB/(cm MHz)
Sampling frequency	420 MHz	420 MHz
Scan step size	0.03 mm	0.03 mm
Excitation pulse	1 cycle pulse	1 cycle pulse
SNR	22 dB	22 dB

The SNR of each point scatterer was also calculated from the reconstructed images similar to [70], where the signal was the root-mean-square (RMS) of image data within the  $-6$ -dB contour of the point scatterer and noise was the RMS of the image data in a  $1.8 \times 1.4$  mm<sup>2</sup> rectangular window located in the background at the same axial distance that did not include sidelobes. The rectangular window size was chosen based on the size of the image and location of the point scatterer. The SNR was expressed in a logarithmic scale as,

$$\text{SNR} = 10 \log_{10} \left( \frac{\text{Signal RMS}}{\text{Noise RMS}} \right). \quad (3.10)$$

The contrast resolution of an anechoic object, which describes the ability to detect an anechoic object in a homogeneous scattering medium, was measured by the CTR similar to [94], [95]. CTR was calculated as the energy of the signal outside the circular region,  $R$ , with  $5\lambda$  diameter centred on the point scatterer at  $(x_0, z_0)$  to the total energy of the signal,

$$\text{CTR}(x_0, z_0) = 10 \log_{10} \left( \frac{\int_{x,z \notin R} f^2(x_0, z_0, x, z) dx dz}{\int f^2(x_0, z_0, x, z) dx dz} \right). \quad (3.11)$$

Virtual tissue-mimicking phantoms with cylindrical inclusions of varying contrast were used for the quantification of image contrast. The simulation parameters are tabulated in Table 3.1. The dimension of the phantom was  $30 \times 27.5 \times 3 \text{ mm}^3$  (axial  $\times$  lateral  $\times$  elevation) and the scatterer density was 160 scatterer/ $\text{mm}^3$ . The point scatterers were distributed uniformly in the ROI and their scattering strength was distributed normally. The contrasts of the inclusions were  $-15$ ,  $-5$ ,  $+5$ , and  $+15$  dB relative to the background, where the contrast was defined as,

$$C = 20 \log_{10} \left( \frac{\text{Inclusion scatterer strength}}{\text{Background scatterer strength}} \right). \quad (3.12)$$

The diameter of the inclusions was 3 mm. The inclusions were placed at five different axial distances and the CSR was defined as [93],

$$\text{CSR} = \frac{|S_{\text{out}} - S_{\text{in}}|}{\sqrt{\sigma_{\text{out}}^2 + \sigma_{\text{in}}^2}}, \quad (3.13)$$

where  $S_{\text{in}}$  and  $\sigma_{\text{in}}$  were the mean and standard deviation of the image data (magnitude of the reconstructed signal prior to log compression), respectively, in a region inside the inclusion and  $S_{\text{out}}$  and  $\sigma_{\text{out}}$  are the mean and standard deviation of the image data, respectively, in a region outside the inclusion at the same axial distance. The selected regions were circles with the same diameter as the inclusions. A total of five virtual phantoms with a different scatterer distribution and strength were scanned and the measured CSR values were averaged. Time gain compensation (TGC) was applied to the RF data prior to the image reconstruction to make their magnitude uniform in the axial direction.

For the analysis of the computation time, images of various dimensions, in the range of  $1023 \times 63$  (samples  $\times$  lines) to  $8182 \times 1000$ , were reconstructed by changing the sampling rate of the data. To this end, 10 different data sets were processed and the average computation time was measured using the stopwatch timer function in MATLAB. A PC workstation, equipped with Intel Core i7-920 CPU (Intel Corp., Santa Clara, CA) running at 3.6 GHz, and 12-GB RAM, was used for processing the data and all computations were done using MATLAB (version 8.5). The theoretical order of the computation complexity of each reconstruction algorithm was also analyzed.

### **3.4.2 Experiments**

A phantom made of nylon threads of 0.1-mm diameter immersed in water was used for the quantification of the spatial resolution. The threads were arranged diagonally with the increments of 3.2 and 2.8 mm in the axial and lateral directions, respectively, as shown in the schematic in Fig. 3.2(a). The ROI was divided into the prefocal and postfocal regions due to the limitation in the axial dimension of the ultrasound scanner and two separate scans were performed. The transducer performed a sector scan of the ROI with a scan angle of about  $15^\circ$  and each frame consisted of 301 scanlines, where each line was an average of 20 consecutive acquisitions. The data were acquired with a sampling frequency of 420 MHz. Scan conversion was performed on the data prior to the image reconstructions.

In addition, an *ex vivo* chicken heart [as shown in Fig. 3.2(b)] was scanned and the reconstructed image quality was analyzed qualitatively. The fresh chicken heart was obtained from the local market, and it was kept in water for about 24 h prior to scanning in order to reduce the amount of air within the tissue. The scans were performed in the transverse (cross-sectional) plane through the left ventricle near the apex of the heart [as shown by the drawn line and an arrow in Fig. 3.2(b)] at three different axial distances (i.e., prefocal, focal, and postfocal regions) from the transducer. The transducer was excited with a single-cycle pulse, and the RF data were acquired with a sampling frequency of 420 MHz. Each scan consisted of 251 scanlines, where each line was an average of 20 consecutive acquisitions. Prior to the image

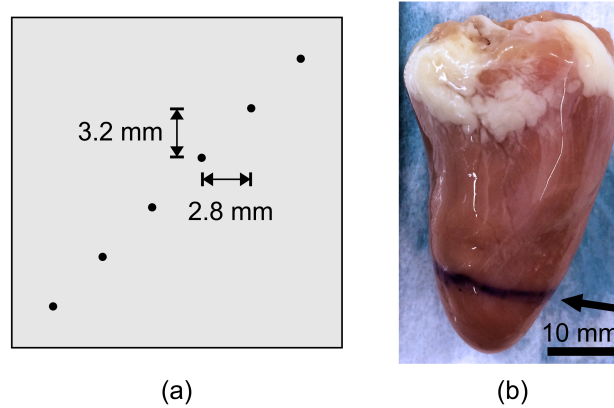


Fig. 3.2. Schematic diagrams of the phantom and image of the ex vivo tissue sample. (a) Custom-built nylon thread phantom. (b) Image of the *ex vivo* chicken heart.

reconstruction, scan conversion and TGC were applied to the acquired RF data.

## 3.5 Results and Discussion

### 3.5.1 Spatial Resolution and Sidelobe

The reconstructed images of the CONV, TD-VPS, FD-VDS, and FD-DC of the virtual point scatterer phantom and the nylon thread phantom in water are shown in Figs. 3.3 and 3.4, respectively. In the CONV, the size of the scatterer was the smallest at the focus of the transducer (i.e., 15-mm axial distance) and the size of the scatterer increased away from the focus. This was expected from a focused transducer since it generates focused wavefronts that converge and result in a narrower beamwidth at the focus. The narrower the beamwidth, the better is the lateral resolution. In Fig. 3.4 (a)-(d), the horizontal lines at axial distances of 2.9 and 4.3 mm were due to the reverberation from the membrane of the plastic enclosure of the transducer that was about 1.4 mm in front of the transducer. In addition, there were other artifacts which appeared as weaker replicas of the point scatterers below each point scatterer possibly due to vibration of the nylon

threads or coincidence of the incident waves frequency with one of the nylon threads resonant mode, which was also observed in [120].

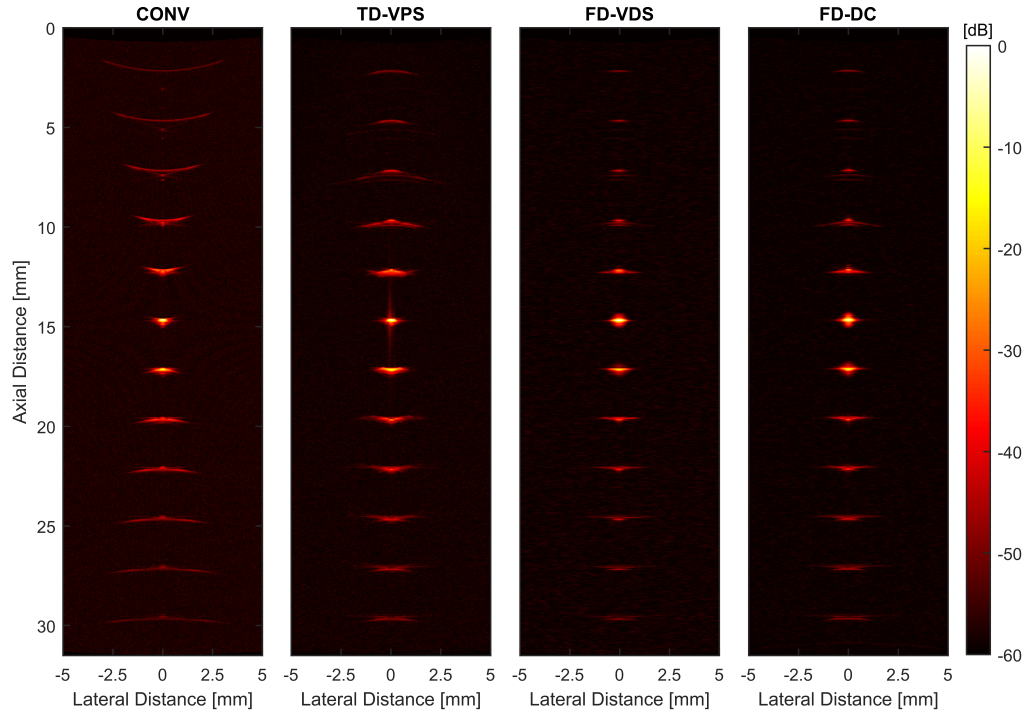


Fig. 3.3. Reconstructed images of the virtual point scatterer phantom in water. The focal distance of the transducer was 15 mm.

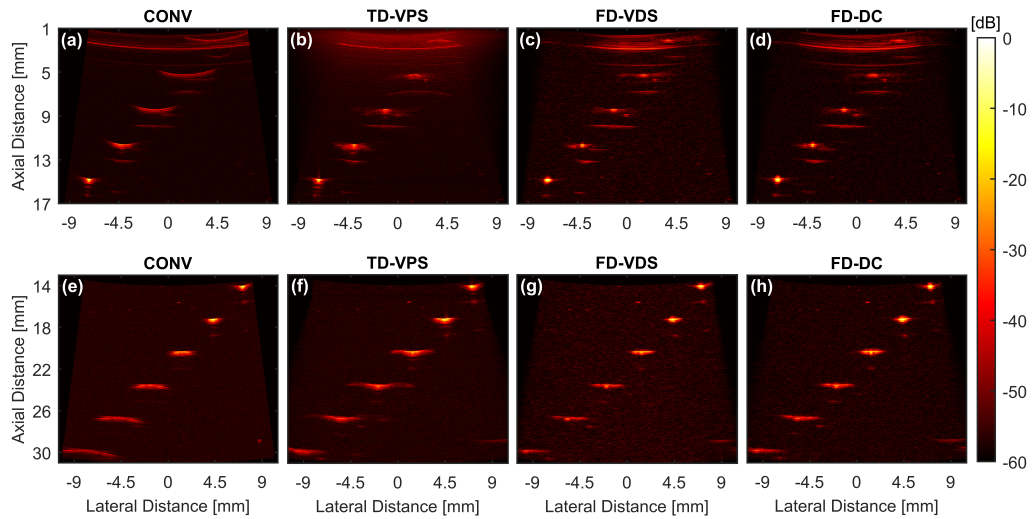


Fig. 3.4. Reconstructed images of the nylon thread in a water phantom. The focal distance of the transducer was 15 mm. The prefocal region of (a) CONV, (b) TD-VPS, (c) FD-VDS, and (d) FD-DC. The postfocal region of the (e) CONV, (f) TD-VPS, (g) FD-VDS, and (h) FD-DC.

In TD-VPS, the size of the scatterer was the smallest at the focus and it became slightly wider away from the focus but still, they were smaller than the CONV. FD-VDS and FD-DC had smaller scatterer size at all axial distances compared to the CONV and TD-VPS. In addition, in FD-VDS and FD-DC, the size of the scatterers remained relatively constant at all axial distances.

The contour area of above  $-6$ - and  $-24$ -dB levels are shown in Fig. 3.5. The CONV (shown by asterisk) had the largest contour areas at both  $-6$  and  $-24$  dB and the contour areas decreased around the focal distance of 15 mm. This confirms the short depth of field of 2.7 mm reported by the manufacturer of the transducer. TD-VPS (shown by the circle) had smaller contour areas compared to the CONV, which confirms previous studies [56], [63], [65]. FD-DC (shown by the star) had generally smaller contour areas compared to the CONV and TD-VPS. In addition, FD-VDS (shown by the diamond) had generally the smallest contour areas.

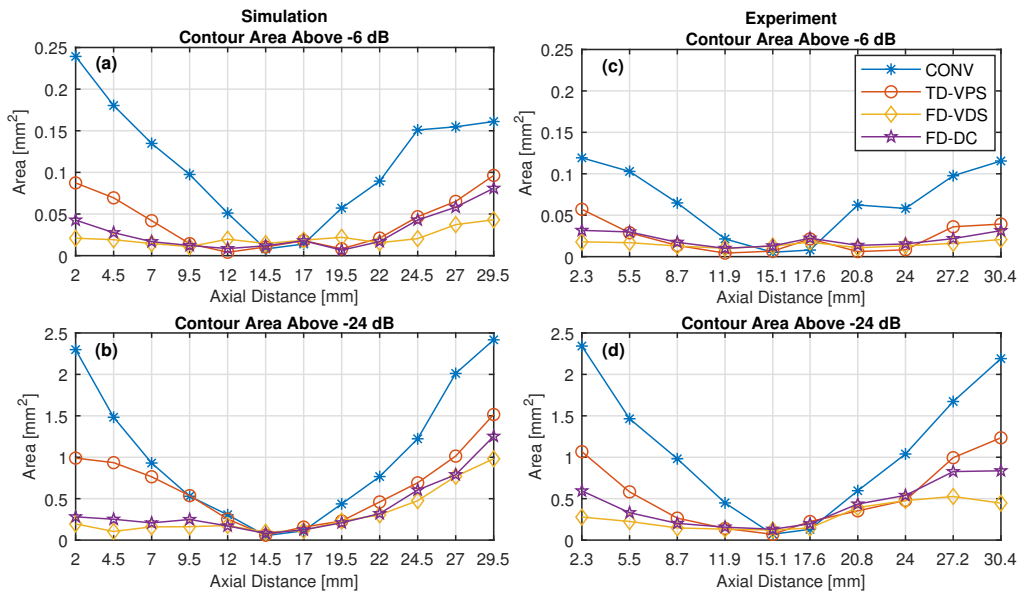


Fig. 3.5. Contour area of the simulated data above (a)  $-6$  and (b)  $-24$  dB, and the contour area of the experimental data above (c)  $-6$  and (d)  $-24$  dB as a function of depth. The focal distance of the transducer was at 15 mm.

A statistical test was also carried out (for results refer to the supplementary content in Appendix A), using permutation test based on paired t-statistic, to determine if the average differences between each method are statistically

significant in a 95% confidence interval. For both the simulated and experimental data in the prefocal and postfocal regions, the  $-6$ - and  $-24$ -dB contour areas of TD-VPS, FD-VDS, and FD-DC were significantly smaller compared to the CONV. In addition, for the simulated data in the prefocal and postfocal regions, the contour area above  $-24$  dB of FD-VDS and FD-DC was significantly smaller compared to TD-VPS. For the experimental data, FD-VDS had significantly smaller contour area above  $-24$  dB compared to TD-VPS in the prefocal region.

These results show that all SAFT algorithms were able to extend the depth of field beyond the CONV. Moreover, FD-VDS and FD-DC had smaller spatial resolutions and sidelobes compared to CONV and TD-VPS. The reason for these improvements is that the FD-VDS and FD-DC compensate for the transducers diffraction effects, the electromechanical impulse response and the excitation pulse of the transducer. FD-VDS compensates the diffraction effect of the transducer in the far-field by assuming the finite-sized virtual source has a flat circular shape. On the other hand, FD-DC compensates the diffraction effect by filtering the simulated PSF of the imaging system from the acquired RF data. The spatial resolution and sidelobe level of FD-DC were not smaller than FD-VDS. This could be attributed to the fact that the simulated PSF in FD-DC is an approximation to a spatially variant PSF of the imaging system and thus it might not have effectively compensated the diffraction effects.

### **3.5.2 Signal-to-Noise Ratio and Contrast Resolution**

The SNR measurements are shown in Fig. 3.6, and the axial beam profiles obtained from Figs. 3.3 and 3.4 are shown in Fig. 3.7.

As it was expected, the SNR of all methods was highest at the focal distance (since the intensity of the ultrasound beam is highest at the focal distance) and they decreased with increasing distance from the focal distance. The CONV had relatively the lowest SNR at all axial distances. All SAFT methods had higher SNR compared to the CONV. A statistical test was carried out to determine if the average difference in SNR between each method is

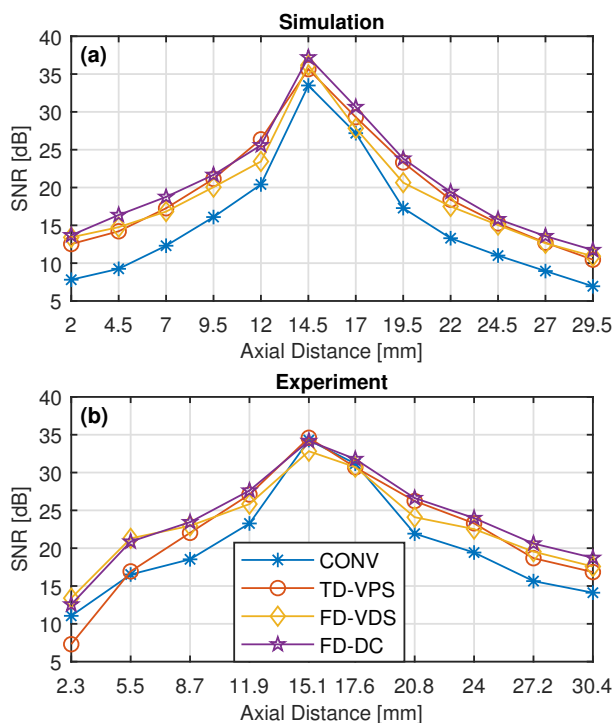


Fig. 3.6. SNR of the (a) simulated and (b) experimental data as a function of depth.

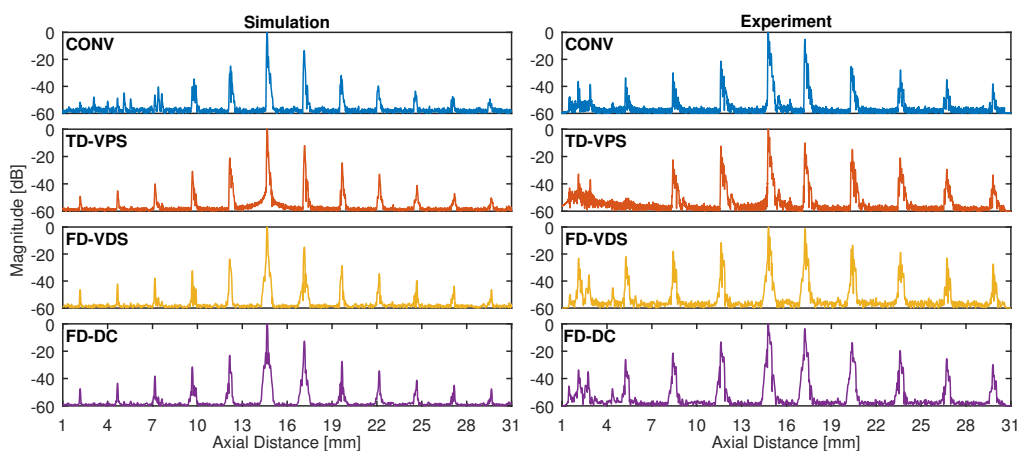


Fig. 3.7. Axial beam profiles for the simulated (left) and experimental (right) data.

statistically significant in a 95% confidence interval (for results refer to the supplementary content in Appendix A), TD-VPS, FD-VDS, and FD-DC had significantly higher SNR for both simulated and experimental data in the prefocal and postfocal regions. In addition, FD-DC had significantly higher SNR compared to TD-VPS in the prefocal and postfocal regions of the simulated and experimental data (except in the prefocal region of the

simulated data). TD-VPS, FD-VDS, and FD-DC had higher SNR compared to the CONV, in the prefocal and postfocal regions, by an average of 1.1 to 5.3 dB, 3.2 to 4.5 dB and 3.8 to 6 dB, respectively. It was expected that both FD-VDS and FD-DC would yield higher SNRs compared to the CONV and the TD-VPS since they both use matched filtering which is effective at filtering out additive white noise [48]. However, only the FD-DC had higher SNR, by an average of 0.8 to 2.7 dB, compared to TD-VPS. FD-VDS had higher SNR compared to TD-VPS in the prefocal and focal region of the experimental data. A possible reason for which the FD-VDS had lower SNR compared to the FD-DC could be due to the use of experimentally measured transducer response in the FD-VDS that is affected by the electronic noise and artifacts of the imaging system.

The measurement of CTR for the simulated and experimental data is shown in Fig. 3.8. The CTR of all methods was lowest at the focal distance, and it degraded outside the focal zone. This trend was expected from a focused transducer since at the focal distance the SNR is highest and spatial resolution is smallest. Generally, all SAFT methods had lower CTR compared to the CONV, except at the focal distance. The CTR of the proposed methods were generally the same and they were smaller than TD-VPS.

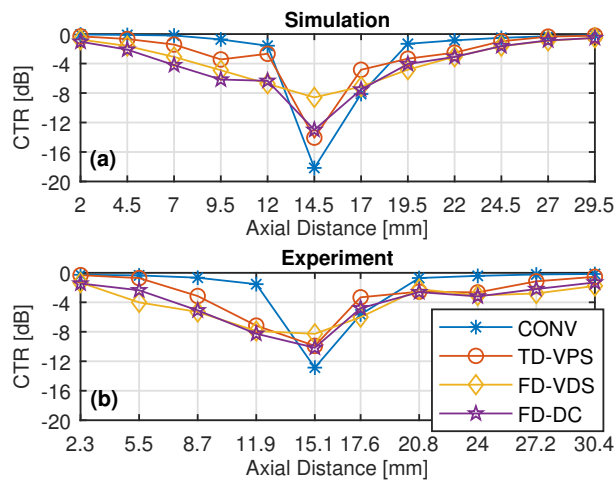


Fig. 3.8. Contrast resolution, measured by the CTR, of the (a) simulated and (b) experimental data as a function of depth.

### 3.5.3 Contrast-to-Speckle Ratio

The reconstructed images of the virtual tissue-mimicking contrast phantom are shown in Fig. 3.9. In the CONV image, the circular shape of the inclusions became deformed at increasing distance from the focal distance of the transducer, due to the short depth of field of the CONV imaging. On the other hand, in TD-VPS, FD-VDS, and FD-DC, the shape of the inclusions was not deformed, due to the improvement of spatial resolution and extension of the depth of field. At the furthest axial distance (i.e., 25.5 mm), the inclusions with the contrast of  $-15$ ,  $-5$ , and  $+5$  dB were not clearly visible due to the high overall attenuation of the medium. The measurements of the contrast of the inclusions, in terms of CSR, are shown in Fig. 3.10, where the average CSR of each inclusion at various axial distances was calculated. In general, the average CSR values of the CONV were the lowest, except for the  $-5$ -dB inclusions. This could be due to the high sidelobe levels and the low SNR of the CONV as shown in Figs. 3.5(b) and 3.6(a). For the  $-15$ -,  $+5$ -, and  $+15$ -dB inclusions, the average CSR values of all SAFT methods were significantly higher compared to the CONV. The CSR of all SAFT methods was similar. The average CSR values of all contrast inclusion of TD-VPS, FD-VDS, and FD-DC were higher by 12%, 13%, and 13%, respectively, compared to the CONV.

### 3.5.4 *Ex vivo* Tissue Image Quality

In Fig. 3.11, the reconstructed images of the *ex vivo* chicken heart tissue in the prefocal, focal, and postfocal regions are shown. In Fig. 3.11(a), a cross-sectional image of the chicken heart slice at approximately the location where the scans were performed is shown. The left ventricle of the heart was at the center of the tissue where the scans were performed. It should be noted that the cross-sectional image [i.e., Fig. 3.11(a)] is not meant to be used for one-on-one comparison with reconstructed images but for a qualitative comparison. Also, the scanning was performed when the chicken heart was in the water while the cross-sectional image was captured when it was in the air after it was cut at the approximate location where the scanning

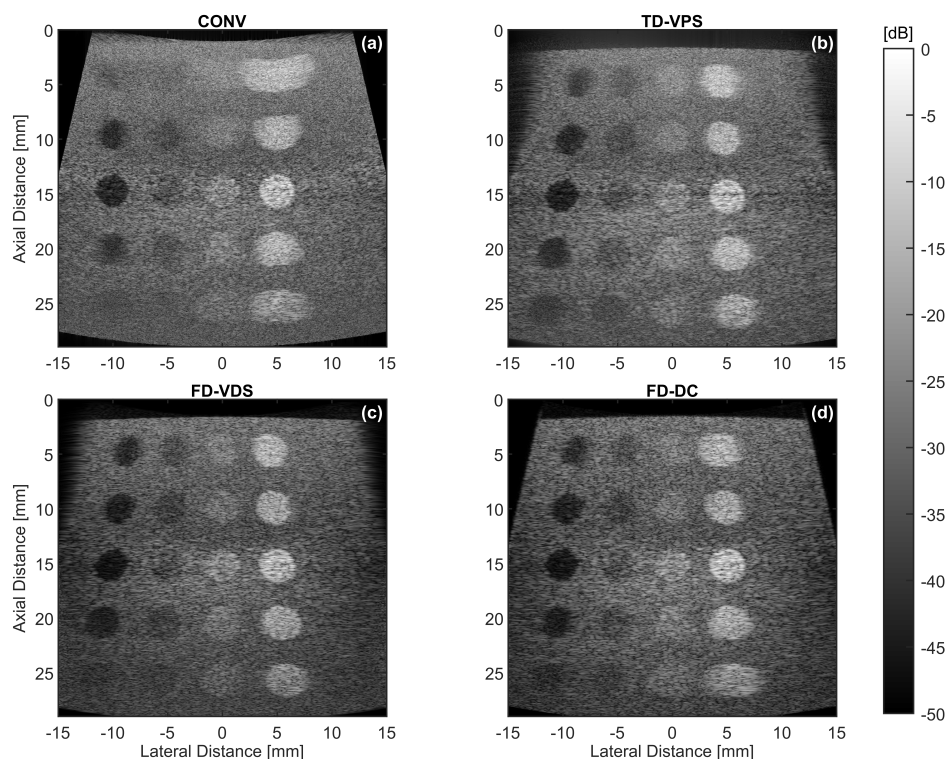


Fig. 3.9. Reconstructed images of the virtual tissue-mimicking contrast phantom. The diameter of the inclusions was 3 mm. The contrast of the inclusions (from left to right) were  $-15$ ,  $-5$ ,  $+5$ , and  $+15$  dB relative to the background. (a) CONV, (b) TD-VPS, (c) FD-VDS, and (d) FD-DC are shown. The focal distance of the transducer was at 15 mm.

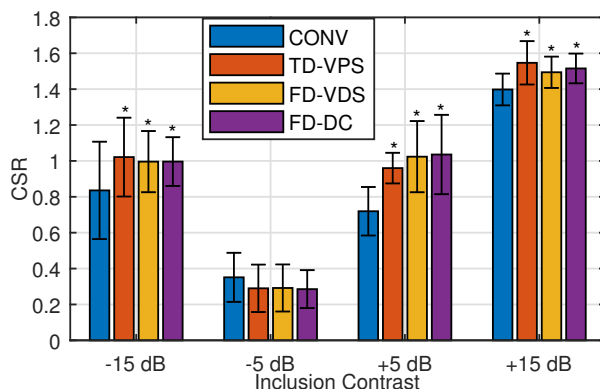


Fig. 3.10. Measurement of the CSR of the inclusion contrast. Five different virtual tissue-mimicking contrast phantoms were scanned and the average contrast was calculated for each inclusion at various depths. The error bars represent the standard deviation. \* represents  $p$ -value  $< 0.05$  compared to CONV.

was performed. It should also be noted that the lateral extent of the tissue in the B-mode images increased slightly from prefocal to postfocal scans,

which could be due to scanning a slightly different slice when the position of the transducer was changed. This issue could also be augmented due to a slight angle in the transducer positioning system or slight movement of the transducer along the tissue.

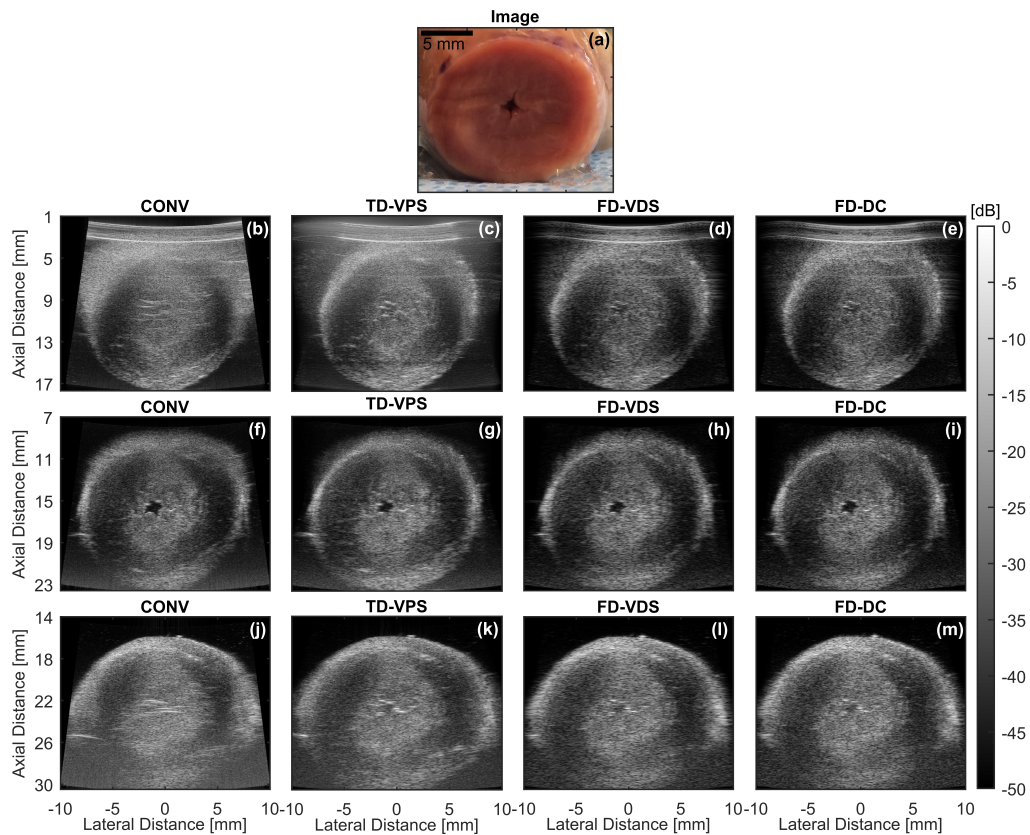


Fig. 3.11. Reconstructed images of the *ex vivo* chicken heart tissue in water in the prefocal, focal, and postfocal regions of the transducer. (a) Cross-sectional image of the approximate scan region. The CONV images are shown in (b), (f), and (j), the TD-VPS images are shown in (c), (g), and (k), FD-VDS images are shown in (d), (h), and (l), and the FD-DC images are shown in (e), (i), and (m).

In CONV images in the prefocal and postfocal regions of the transducer, as shown in Fig. 3.11(b) and (j), the boundary of the tissue and the shape of the ventricle were not clearly visible due to poor lateral spatial resolution. In the prefocal region, the horizontal lines close to the transducer were due to the reverberation of the wave from the membrane of the transducers enclosure, as it was the case in Fig. 3.4. In the focal region, as shown in Fig. 3.11(f), the boundaries of the tissue and the shape of the ventricle were clear and distinct. Thus, if the ROI lays in the prefocal or postfocal regions of the

transducer, then visualization of even high contrast structures becomes quite challenging and the need for improving the lateral resolution in those regions becomes apparent. In all the SAFT reconstructed images, the boundaries of the tissue and ventricle were more clearly visible in the prefocal and postfocal regions compared to the CONV images. Also, the background noises of FD-VDS and FD-DC in the prefocal region were marginally less than TD-VPS.

The measurement of CSR between the left ventricle (at the center of tissue as shown in Fig. 3.11) and background (at the same axial distance) is shown in Fig. 3.12. The CSR of the proposed methods was higher compared to the CONV and TD-VPS, especially in the prefocal and postfocal regions. This could be due to the combined effect of low sidelobe levels and high SNR of the proposed methods compared to the CONV and TD-VPS. All the SAFT reconstruction methods extended the depth of field of the focused transducer which improved visualization of structures in the prefocal and postfocal regions of the transducers. In addition, the proposed methods yielded higher CSR compared to the CONV and TD-VPS.

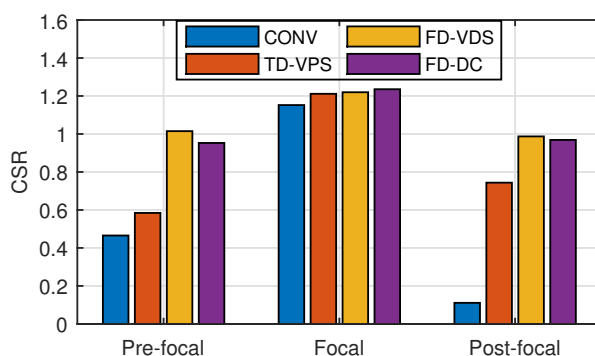


Fig. 3.12. CSR measurement of the left ventricle of the heart (center of the tissue) at various depths.

The speckle pattern of the FD-VDS and FD-DC appears coarser and smoother compared to the CONV and TD-VPS due to matched filtering. The average speckle size, using second-order statistic [121], was measured at  $-6$ -dB contour area. For the experimental data (as shown in Fig. 3.11), the average speckle size of the CONV, TD-VPS, FD-VDS, and FD-DC was 0.010, 0.019, 0.016, and 0.016  $\text{mm}^2$ , respectively. For the simulated data shown in Fig. 3.9, the average speckle size of the CONV, TD-VPS, FD-VDS, and

FD-DC was 0.013, 0.038, 0.038, and 0.041 mm<sup>2</sup>, respectively. The speckle size is typically associated with the spatial resolution of the imaging system [121]. SAFT image reconstruction changes the speckle pattern of the image, and therefore for SAFT image reconstructions, there seems to be a discrepancy in the measurement of spatial resolution using point scatterers and scattering medium.

### **3.5.5 Reconstruction Performance**

The average computation time as a function of pixel numbers in an image is shown in Fig. 3.13. The computation time of the CONV was also measured as a baseline, which included loading into memory (RAM), time-gain compensation, Hilbert transformation, and logarithmic compression of the RF data, and displaying the image on the screen. As expected, the computation time of all algorithms increased as the number of pixels in an image increased. The computation time of the TD-VPS was the highest and it was significantly higher than FD-VDS and FD-DC. The computation time of the proposed algorithms, i.e., FD-VDS and FD-DC, was similar. The ratios of the computation time between CONV and the SAFT algorithms are shown in Fig. 3.14. It showed that the computation run times of TD-VPS, FD-VDS, and FD-DC were higher by 5.7 to 870.7 times, 1.5 to 5 times, and 1.4 to 4.6 times, respectively, compared to CONV. In comparison with the TD-VPS, the computation run times of the FD-VDS and FD-DC were lower by 3.8 to 174.1 times and 4.1 to 189.3 times, respectively. For a typical image size of 500 × 500, the computation run times of TD-VPS, FD-VDS, and FD-DC were higher by 25.7, 2.1, and 2 times, respectively, compared to the CONV. In addition, the computation runtime ratios of proposed algorithms did not increase as rapidly as TD-VPS as the number of pixels increased, which indicated that the proposed algorithms have lower order of computation complexity compared to TD-VPS. It should be noted that the computation time is dependent on the performance of MATLAB and the efficiency of the program.

In terms of theoretical order of computation complexities, TD-VPS has an order of  $\mathcal{O}(MN^2)$  [122], where  $M$  and  $N$  are the number of sample and

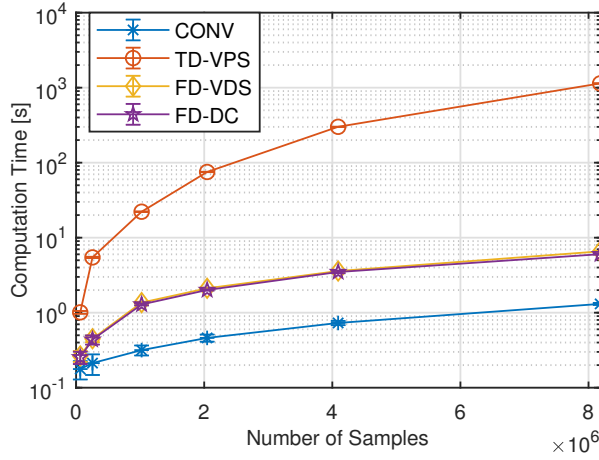


Fig. 3.13. Average computation time to reconstruct and display an image as a function of image size. For each image size. (The 10 data set was processed and all calculations were carried out in MATLAB.)

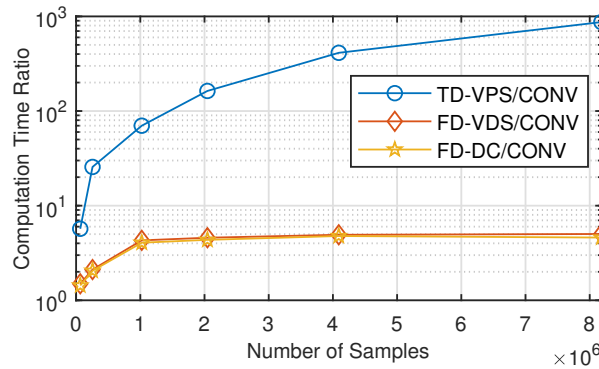


Fig. 3.14. Average computation time ratios between SAFT algorithms and the CONV as a function of image size.

number of lines, respectively. The proposed algorithms, transform the RF data into the Fourier domain using 2-D FFT,  $\mathcal{O}(MN \log_2(MN))$ , perform matched filtering,  $\mathcal{O}(MN)$ , remap and interpolate the data by a factor of  $I$  using Stolt transformation,  $\mathcal{O}(MNI)$ , and transform the data back to the spatial domain using 2-D inverse FFT,  $\mathcal{O}(MN \log_2(MN))$ . Note that the fast Fourier transformation and complex conjugation of the impulse response, directivity function, excitation pulse of the transducer, and PSF of the system have not been taken into account since they can be done prior to image reconstruction. Thus, the total complexity of the proposed algorithms is  $\mathcal{O}(MN \log_2(MN))$ .

## **3.6 Conclusion**

In this work, two FD-SAFT algorithms, namely, FD-VDS and FD-DC, were proposed based on the well-known SARs wavenumber algorithm. FD-VDS treats the focus of the transducer as a virtual source of finite size in which the diffraction effect of the transducer in the far-field was taken into account in the image reconstruction. FD-DC filters out the simulated PSF of the imaging system from the recorded echo signal.

Among the four image reconstruction algorithms studied in this work, FD-VDS had the smallest spatial resolution and FD-DC had the second smallest spatial resolution. In addition, FD-DC had the highest SNR, while FD-VDS had higher SNR compared to the CONV but lower than the TD-VPS. Moreover, FD-DC and FD-VDS had generally lower CTR compared to CONV and TD-VPS. However, the CSR of FD-VDS and FD-DC was similar to the TD-VPS. Furthermore, the proposed algorithms are significantly more efficient compared to the TD-VPS without sacrificing the image quality. Thus, the proposed algorithms offer efficient and robust solutions to make the lateral spatial resolution of ultrasound more uniform and extend the depth of field of the CONV imaging.

As a possible next-step study, the proposed algorithms can be implemented for harmonic imaging, where harmonics are generated due to nonlinear ultrasound wave propagation in tissue, and for imaging with array transducers. In addition, the proposed algorithms can be implemented with coded excitations, which is currently an ongoing research in our group.

## **3.7 Acknowledgements**

The authors would like to thank M. C. Kolios from the Department of Physics, Ryerson University, Toronto, ON, Canada, for providing access to the high-frequency ultrasound scanner, and A. Worthington, B. Maraghechi, and G. Ferrier from the Department of Physics, Ryerson University, for providing technical assistance.

## Chapter 4

# The Use of Coded Excitation for Frequency-Domain Synthetic Aperture Focusing Techniques in Single-Element Ultrasound Imaging

---

*This chapter is a journal article under review for publication to IEEE-T-UFFC (E. Shaswary, J. C. Kumaradas, and J. Tavakkoli, The use of coded excitation for frequency-domain synthetic aperture focusing techniques in single-element ultrasound imaging, submitted on Feb 27, 2019.)*

## 4.1 Abstract

Synthetic aperture focusing techniques (SAFT) make the spatial resolution of the conventional ultrasound imaging from a single-element focused transducer more uniform in the lateral direction. Previously, two new frequency-domain SAFT algorithms referred to as frequency-domain SAFT virtual source (FD-VDS) and frequency-domain SAFT deconvolution (FD-DC) were proposed for high-frequency single-element focused transducers [123]. These algorithms used the conventional pulsed excitation. Here we present the use of linear frequency modulated chirp excitation for the two previously presented frequency-domain SAFT algorithms. The performance of these methods was studied using a series of simulations and it was compared with the conventional B-mode and time-domain SAFT methods for both pulsed and coded excitations. Image quality was analyzed in terms of signal-to-noise ratio (SNR), spatial resolution, sidelobe level and contrast-to-speckle ratio (CSR). The results showed that coded excitation improves the SNR of all methods by about 8 dB. For both pulsed and coded excitations, the SNR of FD-DC was higher than the conventional B-mode, time-domain virtual point source and FD-VDS by an average of 5.2 dB, 1.3 dB and 1.2 dB, respectively. For all the methods, the spatial resolution, sidelobe level and CSR were the same between the pulsed and coded excitations. In addition, the CSR of all SAFT methods were higher than the conventional B-mode.

## 4.2 Introduction

Synthetic aperture focusing techniques (SAFT) have been originally used in synthetic aperture radar, to improve the lateral spatial resolution of the images of remote objects on terrains or planets [48]. SAFT uses signal-processing techniques to synthesizes an effective long aperture instead of using a physically long aperture. The size of the aperture and lateral spatial resolution are inversely propositional. Subsequently, SAFT has been used in synthetic aperture sonar [51], non-destructive evaluation [52] and ultrasound imaging [53]. In ultrasound imaging, SAFT has been used to make

the lateral spatial resolution of the conventional B-mode imaging from a single-element focused transducer more uniform. Unlike synthetic aperture radar where chirp coded excitations are typically used, ultrasound imaging typically relies on pulsed excitation. For ultrasound imaging, numerous SAFT algorithms have been proposed in the literature in both time [61]–[64] and frequency [56], [60], [66]–[68], [124] domains. For a single-element focused transducer with pulsed excitation, the virtual point source technique is typically used. This technique treats the geometric focus of the transducer as a virtual point source in the image reconstruction process. Virtual point source techniques are simple since the diffraction effect of focused transducers is neglected. Time-domain virtual point source SAFT (TD-VPS-PLSD) is based on delay-and-sum (DAS) beamforming methods. It assumes that the geometric focus of the transducer emits a spherical wave which propagates both towards and away from the transducer. Hence, the geometric focus is called the virtual source. The image reconstruction is done separately in the pre-focal and post-focal regions by delaying the recorded echo signals according to the relative image position and the virtual source. This is then followed by summation (see [64] for more details). Frequency-domain SAFT is based on the wavenumber algorithm from synthetic aperture radar (SAR) [48], [54], [91], [125]. The algorithm performs a 2D Fourier transformation on the echo data, followed by a 2D matched filtering, a coordinate transformation (known as Stolt migration in seismic imaging [89]) and an inverse Fourier transformation.

Attenuation of the ultrasound wave in tissue deteriorates the ultrasound SNR and image quality with depth, which limits the imaging depth. The imaging depth can be increased either by increasing the amplitude or the duration of the excitation pulse of the transducer. The amplitude of the excitation pulse has safety regulatory limits to avoid potential harmful effects (e.g., acoustic cavitation and thermal heating) [9] and increasing the excitation pulse duration decreases axial resolution. Thus, there is a trade-off between the SNR/penetration depth and axial resolution. Coded excitation can be used to increase SNR without decreasing the axial resolution. Coded excitation uses long duration, but broadband, excitation signals. They are typically encoded by a frequency-modulated chirp [21], [126], [127] or binary

codes, such as Golay [128], Barker [129] and M-sequence [130] codes. The reflected signal is typically decoded by matched filtering in the time-domain by convolving the reflected signal with the time-reversed excitation signal [20].

Coded excitation has been used to increase the SNR by around 15 dB in synthetic aperture ultrasound imaging. In these cases, a coded pulse was transmitted and the received signal was decoded to increase the SNR before time-domain synthetic aperture reconstruction techniques were used. Passmann and Ermert used chirp coded excitation for a 100 MHz single-element focused transducer [61]. Thomas and Chiao [83], O'Donnell and Wang [85] and Lashkiari *et al.* [131], [132] used Golay encoding with a linear array [83]. Misaridis and Jensen used chirp coded excitation and Hadamard spatial encoding with a linear array to increase frame rates 12-fold while maintaining SNR [84]. All these methods used a two-step process, which limits the computation efficiency of the imaging and complicates its implementation.

Recently, in [123] we presented two frequency-domain SAFT algorithms for pulsed excitation based on 2D matched filtering for single-element focused transducers. The first algorithm was a frequency-domain SAFT with a virtual source that treated the focal point of the transducer as a virtual flat disk source (FD-VDS-PLSD). In the image reconstruction, it compensated for the diffraction effects in the far-field, the electromechanical impulse response and the shape of the excitation signal. The second algorithm was a frequency-domain SAFT deconvolution with a simulated point-spread-function (PSF) of the imaging system as a filter kernel for the matched filter used in the image reconstruction (FD-DC-PLSD). The performance of both algorithms was compared with the conventional B-mode (CONV-PLSD) and TD-VPS-PLSD in terms of spatial resolution, electronic signal-to-noise ratio (SNR), contrast to speckle ratio (CSR) and computational efficiency. The results showed that compared to CONV-PLSD all tested SAFT algorithms had better spatial resolution and higher SNR and CSR. The frequency-domain SAFT generally had better spatial resolution and higher SNR and CSR compared to TD-VPS-PLSD. In addition, the computational efficiency of both algorithms was between 4 and 190 times higher than TD-VPS-PLSD (depending on image dimension).

In this work, the results from using a linear frequency modulated (FM) chirp excitation signal is presented with frequency-domain virtual disc source (FD-VDS-CHRP) and with frequency-domain deconvolution (FD-DC-CHRP) methods for a high-frequency single-element focused transducer. Since both algorithms account for the excitation signal, the two-step process used in previous studies can be reduced to a one-step process where the decoding of the coded signal is done during image reconstruction. The computational efficiency of FD-VDS-CHRP and FD-DC-CHRP are the same as FD-VDS-PLSD and FD-DC-PLSD, respectively, since in the image reconstruction the pulsed excitation signal is simply replaced with the chirp excitation signal. The additional computational requirement to generate and transmit a chirp excitation signal is small compared to the total computational requirement. In addition, the use of coded excitation is expected to improve the SNR beyond conventional B-mode with coded excitation (CONV-CHRP) and TD-VPS-CHRP.

### 4.3 Methods

A series of simulations were performed to evaluate the performance of the proposed algorithms. Since the results of simulated data were very similar to the experimental data in our previous study [123], in this study only simulated data was used. In addition, commercial high-frequency ultrasound scanners that are available to us do not currently offer coded excitation capabilities. All radio-frequency (RF) data was generated using the Field II simulation software [114], [118] that simulated a commercially-available single-element spherically focused transducer with a 25 MHz central frequency, a 7 mm diameter and a 15 mm focal length (RMV-710B, FUJIFILM Visualsonics, Toronto, Canada). The electromechanical impulse response of the transducer was determined experimentally and was used in all the simulations. The excitation signal was a linear FM chirp, where the frequency was swept within the bandwidth of the transducer, from 5 MHz to 35 MHz, as shown in Fig. 4.1. A Tukey window [21], [127] with 75% tapering was also applied to the excitation signal to reduce the sidelobes. White Gaussian noise, mimicking electronic noise, equivalent to  $-21$  dB was added to

the generated RF data. The performance of the proposed algorithms was compared to conventional B-mode and TD-VPS reconstructions and image quality was measured in terms of spatial resolution, SNR and CSR. All calculations were carried out in Matlab (The MathWorks Inc., Natick, MA).

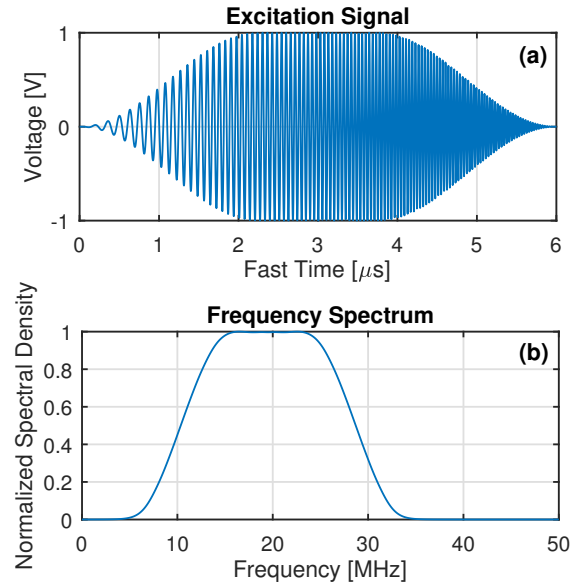


Fig. 4.1. Excitation signal (a) and its frequency spectrum (b).

A virtual phantom with point scatterers in water was sector scanned for the quantification of the spatial resolution and SNR. The spatial resolution and sidelobe size were defined as the area inside the  $-6$  dB and  $-24$  dB contours around each point scatterer, respectively. SNR was measured similar to [70], where the signal was the root-mean-square (RMS) of the image data (without logarithmic compression) inside the  $-6$  dB contour around each point scatterer and noise was the RMS of the image data in a rectangular region located in the background of the image, where no scatterers or sidelobes were present, at same axial distance. The point scatterers were distributed along the transducer axis, between 2 mm and 29 mm from the transducer surface in increments of 2 mm. The parameters used for this phantom are in Table 4.1. The phantom was scanned with various chirp excitation lengths ranging from 0.1  $\mu\text{s}$  to 18  $\mu\text{s}$  in order to determine the optimal excitation length by measuring the contour area above  $-6$  dB and SNR at 4 mm, 16 mm and 26 mm axial distances.

TABLE 4.1: The values of the simulation parameters for the point scatterer phantom.

Parameter	Values
Speed of sound	1500 m/s
Attenuation coefficient	$2.17 \times 10^{-3}$ dB/(cm MHz)
Fast time sampling frequency	420 MHz
Lateral scan step size	$0.02^\circ$

A second type of virtual tissue-mimicking phantom containing cylindrical inclusions of various contrast was used for the quantification of the CSR. Point scatterers were distributed randomly in the inclusions and surrounding regions at the same spatial density. The magnitude of the scattering coefficient of each point scatterer was normally distributed, with a mean,  $\mu$ , and standard deviation,  $\sigma$ . The sign (phase) of the scattering coefficient of each scatterer was randomly distributed between positive and negative with equal probability. The macroscopic scattering strength of the inclusions relative to the background was set to  $-15$  dB,  $-5$  dB,  $+5$  dB and  $+15$  dB by scaling and accordingly. The diameter of the inclusions was 3 mm and the inclusions of each contrast were placed at 5 different depths. The values of the simulation parameters are shown in Table 4.2.

The CSR was measured as [93]:

$$\text{CSR} = \frac{|S_{\text{out}} - S_{\text{in}}|}{\sqrt{\sigma_{\text{out}}^2 + \sigma_{\text{in}}^2}}, \quad (4.1)$$

where  $S_{\text{in}}$  and  $\sigma_{\text{in}}$  were the mean and standard deviation, respectively, of the magnitude of the reconstructed signal prior to log compression in a region inside the inclusion and  $S_{\text{out}}$  and  $\sigma_{\text{out}}$  are the mean and standard deviation, respectively, in a region outside the inclusion at the same axial distance. An entire inclusion was used for calculating the CSR of that inclusion. The CSR was averaged over 5 independent realizations of the virtual phantom (5 phantoms with randomized scattering strength and position distributions were used, each with a different random number seed). Time gain compensation (TGC) was also applied to the RF data, prior to image reconstruction.

TABLE 4.2: The values of the simulation parameter for tissue-mimicking contrast phantom.

Parameter	Values
Speed of sound	1540 m/s
Attenuation coefficient	0.5 dB/(cm MHz)
Fast time sampling frequency	420 MHz
Lateral scan step size	0.06°
Scatterer density	160 mm <sup>-3</sup>
$\mu$	4.7
$\sigma$	1.0
Dimensions of the phantom	30×27.5×3 mm <sup>3</sup> (axial×lateral×elevation)

A statistical test using permutation test based on paired t-statistics was carried out to determine if the average differences between each method are statistically significant in a 95% confidence interval.

## 4.4 Results and Discussion

### 4.4.1 Chirp Excitation Length

The  $-6$  dB contour area and SNR at 3 different depths for various chirp excitation lengths are shown in Fig. 4.2. The  $-6$  dB contour area varied by at most 16% for all methods at all depths except for the CONV-CHRP at 4 mm depths, the FD-VDS-CHRP at 16 mm depth and FD-DC-CHRP at 16 mm depth, where the variation was at most 21%, 29% and 20%, respectively. The SNR increased by about 7.5 dB for all reconstruction algorithms when the length of the chirp excitation increased from 0.1  $\mu$ s to 6  $\mu$ s after which it plateaued.

### 4.4.2 Spatial Resolution and Sidelobe Level

Fig. 4.3 shows the reconstructed images of the virtual point scatterer phantom and Fig. 4.4 shows the measurements of the area inside the  $-6$  dB and  $-24$  dB contours for all the method with both pulsed and chirp excitations.

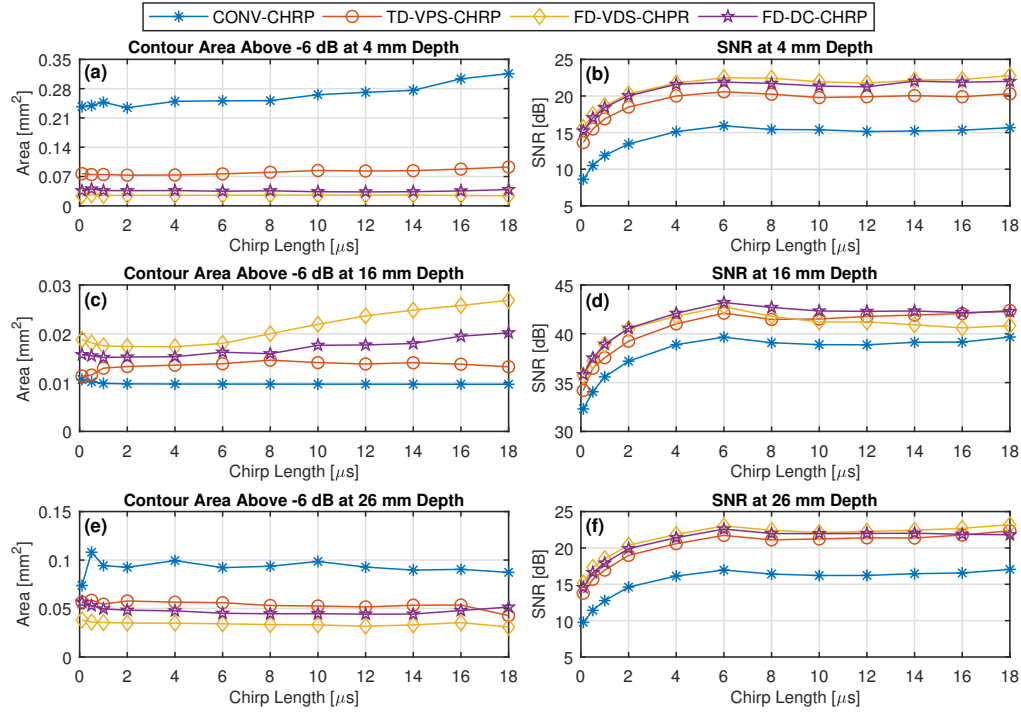


Fig. 4.2. Dependence of image quality parameters on chirp length.

The ratio of the contour areas of chirp to pulsed excitations is shown in Fig. 4.5.

The  $-6$  dB and  $-24$  contour areas for the chirp excitation were larger than the pulsed excitation by an average of 13%,  $-1\%$ , 16% and 1% for the CONV, TD-VPS, FD-VDS and FD-DC, respectively. However, these differences were statistically insignificant. Thus, the difference in contour areas between chirp and pulsed excitations were the same for all the methods showing that chirp excitation does not affect the spatial resolution and sidelobe level.

In the CONV-PLSD and CONV-CHRP (as shown in Fig. 4.3), the size of the PSFs was smallest at the focal distance (15 mm) and it increased away from the focal distance, which was expected for a focused transducer. The measurement of the contour areas (as shown in Fig. 4.4) confirms that the contour areas are smallest at the focal distance. A comparison between each method for both pulsed and chirp excitations are shown in Fig. 4.6. The  $-6$  dB and  $-24$  dB contour areas of the CONV-PLSD and

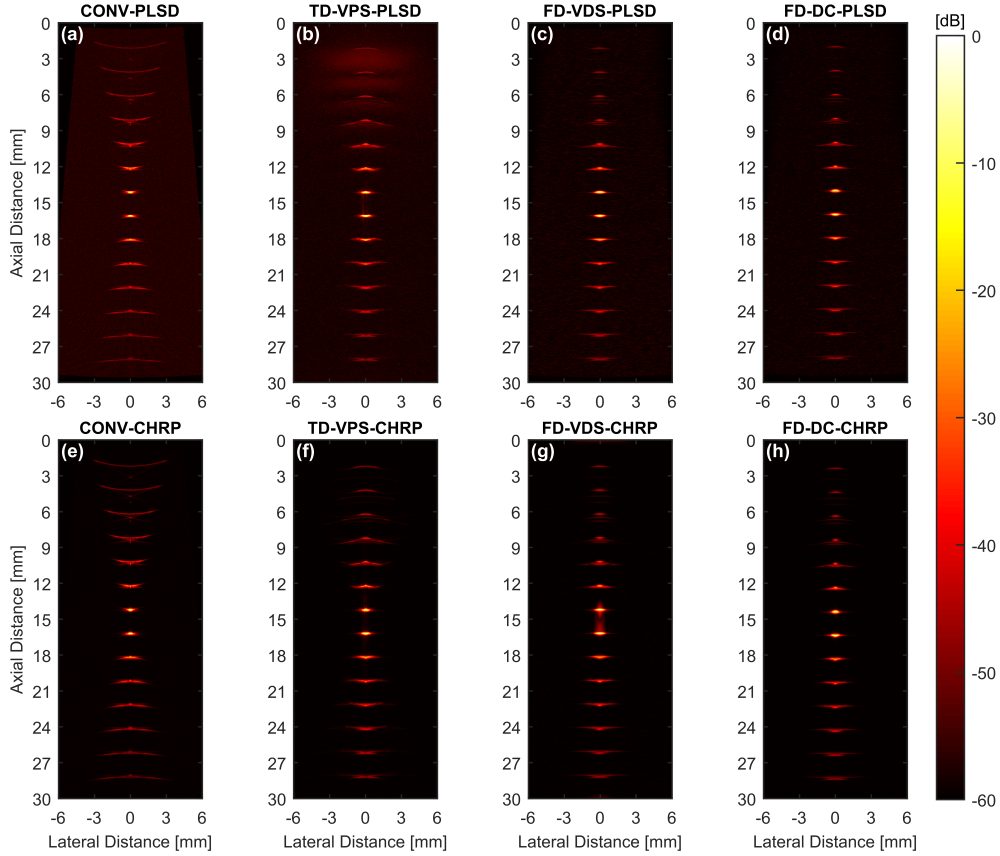


Fig. 4.3. The reconstructed images of the virtual point scatterer phantom in water for the pulsed (top row) and coded (bottom row) excitations. The focal distance of the transducer was 15 mm.

CONV-CHRP were significantly higher than the SAFT methods in the pre-focal and post-focal regions. In TD-VPS-PLSD [Fig. 4.3 (b)], the bright background in the pre-focal region was possibly due to artifacts in the RF data that was generated by the simulation software caused by edge waves. The bright background in TD-VPS-PLSD seems to be more pronounced due to the image reconstruction method. The  $-6$  dB contour area for FD-VDS and FD-DC was smaller by an average of 1.6 and 1.3 times, respectively, compared TD-VPS for both pulsed and chirp excitations at all the depths. However, these differences were not statistically significant. The  $-24$  dB contour area of FD-VDS and FD-DC was smaller by an average of 2.0 and 1.7 times, respectively, compared with TD-VPS for both pulsed and chirp excitations at all the depths. These differences were statistically significant in the pre-focal region of both FD-VDS and FD-DC and only in the post-focal region of FD-VDS.

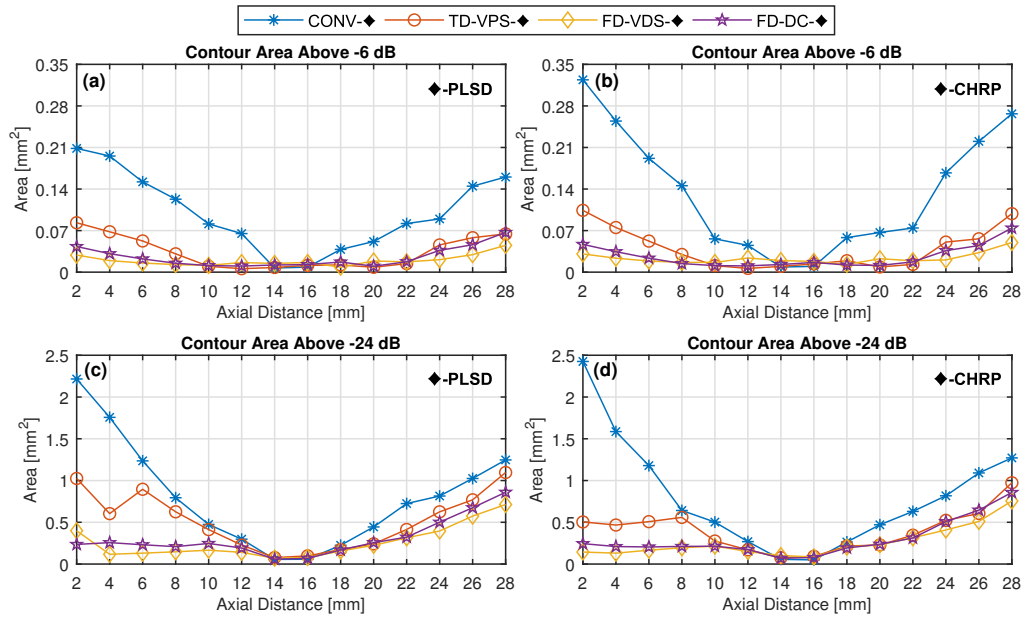


Fig. 4.4. The contour area of the pulsed excitation above  $-6$  dB (a) and  $-24$  dB (c), and the contour area of the coded excitation above  $-6$  dB (b) and  $-24$  dB (d) as a function of depth.

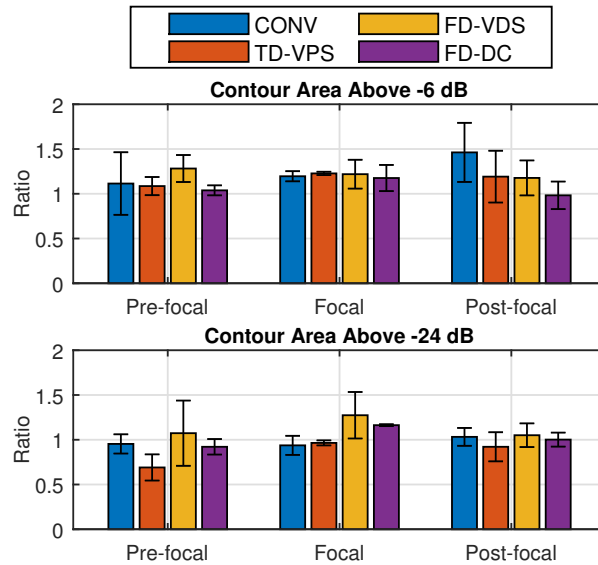


Fig. 4.5. The ratio of the contour areas of chirp to pulsed excitations.

### 4.4.3 Signal-to-Noise Ratio

The measurement of the SNR for both the pulsed and coded excitations is shown in Fig. 4.7. The SNR of all methods was higher in the focal region since the intensity of the ultrasound beam is higher in the focal region. Fig.

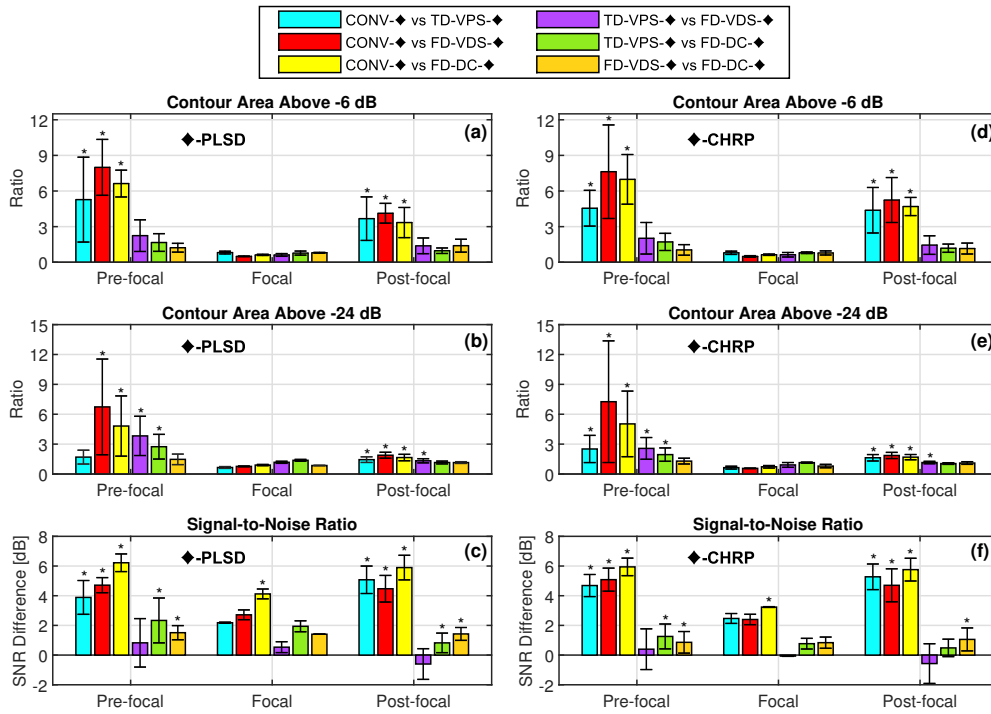


Fig. 4.6. The average ratio of  $-6$  dB and  $-24$  dB contour areas between various methods and the average difference in SNR between the various methods in the pre-focal, focal and post-focal regions for the pulsed (left column) and chirp (right column) data. The error bars represent the standard deviation of the ratios and difference and \* represents a p-value  $< 0.05$ .

4.6 (c) and (f) shows the average difference in SNR between each method for pulsed and chirp excitations, respectively.

For both pulsed and coded excitations, TD-VPS, FD-VDS and FD-DC had higher SNR compared to CONV by an average of 3.9 dB, 4.0 dB and 5.2 dB, respectively. In the pre- and post-focal regions these differences were statistically significant. The SNR of FD-VDS and TD-VPS was about the same. It was expected that both FD-VDS and FD-DC would yield in higher SNR compared to TD-VPS since they both use matched filtering, which is effective at filtering out additive white noise [48]. This could have been due to the use of experimentally measured transducer response in the FD-VDS that was affected by the electronic noise and artifacts of the imaging system.

The SNRs of the chirp excitation of all methods were higher by about 8 dB compared to pulsed excitation, as shown in Fig. 4.8. The difference between chirp and pulsed excitations is statistically significant for all the

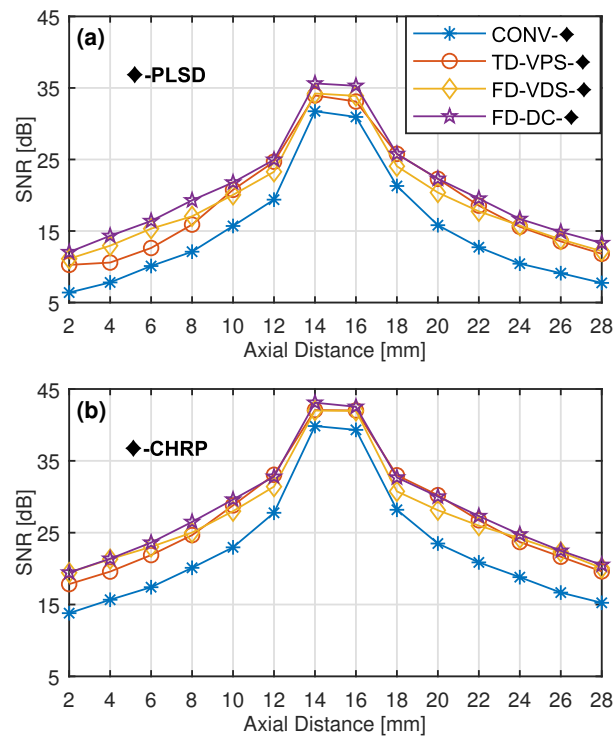


Fig. 4.7. The signal-to-noise ratio (SNR) of the pulsed (a) and chirp (b) excitations as a function of depth.

methods showing that chirp excitation significantly improves the SNR of the reconstructed images.

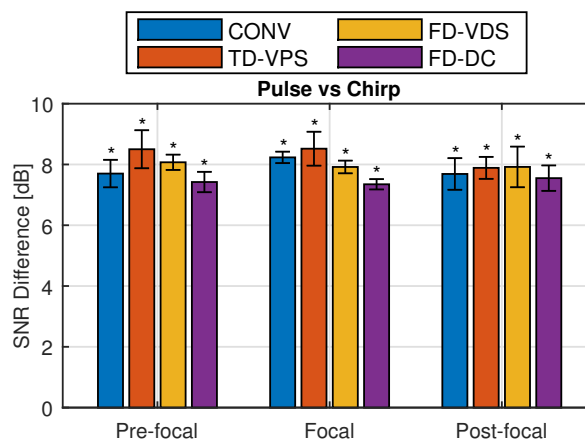


Fig. 4.8. SNR difference between chirp and pulsed excitations. The error bars represent the standard deviation of the difference in SNR between the regions around the point scatterers and \* represents a p-value < 0.05

#### 4.4.4 Contrast-to-Speckle Ratio

The reconstructed images of the virtual tissue-mimicking phantom are shown in Fig. 4.9. In contrast to the CONV method, the shape of circular inclusions was not deformed with increasing distance from the focal region of the transducer in the TD-VPS, FD-VDS and FD-DC methods due to the extension of the depth of field and improvement of the spatial resolution.

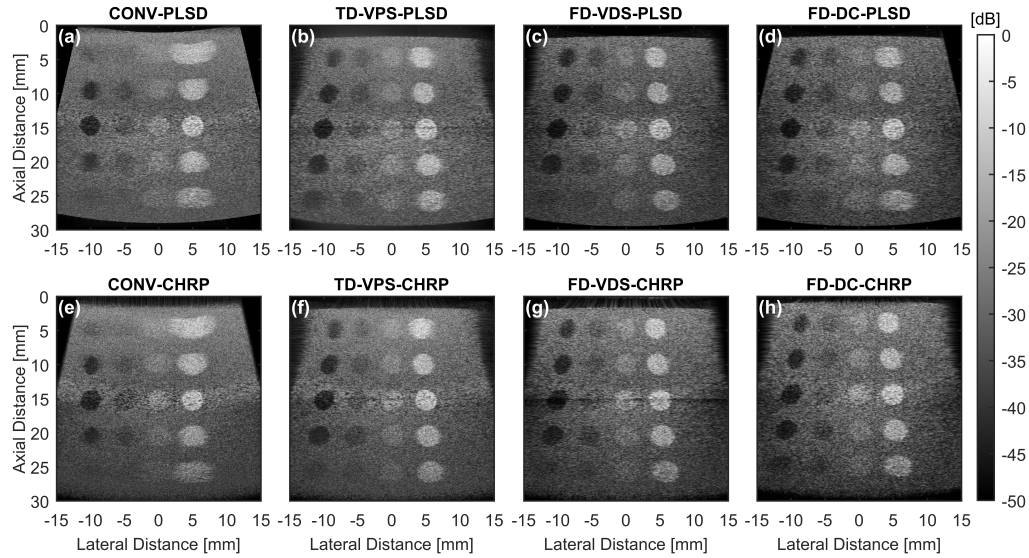


Fig. 4.9. The reconstructed images of the virtual tissue-mimicking contrast phantom for the pulsed (top row) and coded (bottom row) excitations. The diameter of the inclusions was 3 mm. The contrast of the inclusions (from left to right) was  $-15$  dB,  $-5$  dB,  $+5$  dB, and  $+15$  dB relative to the background. The focal distance of the transducer was at 15 mm.

The measurement of the average CSR for each contrast inclusion at various depths for both pulsed and chirp excitations are shown in Fig. 4.10. Generally, the CONV method had lower CSR compared to the SAFT methods for both pulsed and chirp excitations. The CSR of the TD-VPS-PLSD, FD-VS-PLSD and FD-DC-PLSD was higher than the CONV by an average of 12%, 13% and 13%, respectively. The average CSR of the TD-VPS-CHRP, FD-VS-CHRP and FD-DC-CHRP was higher than the CONV by 12%, 17% and 20%, respectively. These differences were in general statistically significant for both pulsed and chirp excitations. FD-VDS had higher CSR compared TD-VPS by an average of 3% for both pulsed and chirp excitations. FD-DC had higher CSR compared to TD-VPS by an average

of 4% for pulsed and chirp excitations. In general, the CSR of all methods was the same between the pulsed and chirp excitations. It was expected that chirp excitation would yield higher CSR compared pulsed excitation since the SNR of all methods was higher by an average of 8 dB in chirp excitation.

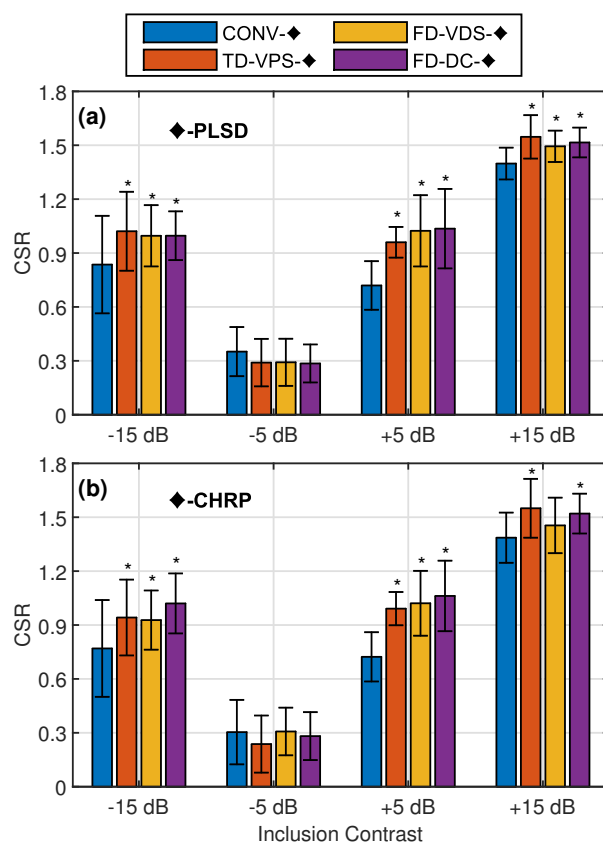


Fig. 4.10. The measurement of the CSR of the inclusion contrast. 5 different virtual tissue-mimicking contrast phantoms were scanned and the average contrast was calculated for each inclusion at various depths for both (a) pulsed and (b) coded excitations. The error bars represent the standard deviation of CSR and \* represents p-value < 0.05 compared to conventional B-mode.

## 4.5 Conclusion

In this paper, the FD-VDS and FD-DC methods were used with chirp coded excitation. Since both of these algorithms compensates the excitation signal and they simplify the use of coded excitation without affecting their

efficiency.

Chirp excitation improved the SNR of all methods by about 8 dB. FD-DC-PLSD and FD-DC-CHRP had the highest SNR. For both pulsed and chirp excitation, the SNR of FD-DC was higher than CONV, TD-VPS and FD-VDS by an average of 5.2 dB, 1.3 dB and 1.2 dB, respectively. FD-VDS and TD-VPS had higher SNR compared to the CONV by an average of 4.0 dB and 3.9 dB, respectively for both pulsed and chirp excitations. The SNR of FD-VDS and TD-VPS was about the same.

The spatial resolution (measured by the  $-6$  dB contour area) and the sidelobe level (measured by the  $-24$  dB contour area) were the same between pulsed and chirp excitations for all the methods. All SAFT methods had significantly smaller spatial resolution and sidelobe level compared to the CONV for both pulsed and chirp excitations. In addition, the sidelobe level of FD-VDS was significantly smaller compared to TD-VPS outside the focal regions. FD-DC had significantly smaller sidelobe level compared to TD-VPS in the pre-focal region. The CSR of the SAFT methods for both pulsed and chirp excitations were generally the same, but they were higher than the CONV.

Chirp excitation significantly improved SNR of pulsed excitation of all methods without significantly affecting the spatial resolution and sidelobe levels. FD-VDS-CHRP and FD-DC-CHRP offer an efficient solution to improve SNR and improve the spatial resolution of the CONV method.

## 4.6 Acknowledgements

Research funding for this work was partially provided by Natural Sciences and Engineering Research Council of Canada (NSERC) Discovery Grants that were awarded to C. Kumaradas and J. Tavakkoli.

# Chapter 5

## Discussion, Conclusions, and Future Work

### 5.1 Discussion

The work in this dissertation describes two new frequency-domain (FD) synthetic aperture focusing technique (SAFT) algorithms for imaging with single-element focused transducers.

The two new FD-SAFT algorithms were both based on the wavenumber algorithm from synthetic aperture radar, and 2D matched filtering. The first was a FD SAFT virtual source algorithm which treated the focus of transducer as a virtual disk source (FD-VDS) having a finite size and the diffraction effect in the far-field was taken into account in the image reconstruction. The rationale for treating the focus of the transducer as a virtual disk source is that the field variation at the focal plane of a focused transducer is the same as the far-field region of a plane piston transducer [133]. Previously, the focus of the transducer was assumed to be a virtual point source (VPS) [30], [61]–[64], [68], however, as shown in Fig. 5.1, the pressure field of a point source is quite different from a focused source. The pressure field of a disk source is also shown in Fig. 5.1, which more resembles the pressure field of a focused source compared to a point source. Therefore, a disk source is a better assumption to a focused source compared to a point

source. The second algorithm was a FD SAFT deconvolution (FD-DC), which used the simulated point spread function of the imaging system as a filter kernel in the image reconstruction.

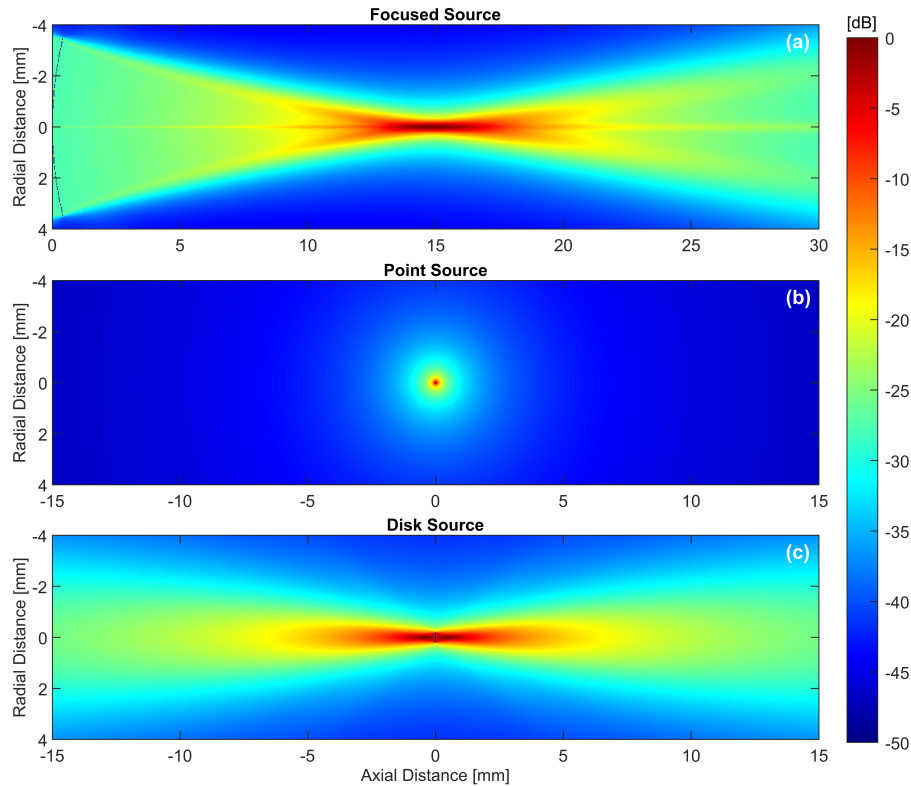


Fig. 5.1. Simulated pressure field for pulsed excitation of (a) a focused source, (b) a point source, and (c) a disk source.

The susceptibility of the proposed methods to tissue motion is the same as conventional B-mode since the data acquisition is done in the same exact way and only the applied image reconstruction on the received data is different. In this work, the data was acquired by sector scanning a single-element transducer, however, the proposed method can be applied to linear or curvilinear scan trajectories. For curvilinear scan trajectory, scan conversion has to be applied to the received data prior to the image reconstruction. In addition, the proposed methods can be applied to transducers with different f-numbers. The improvement of the spatial resolution will be greater for the transducer with smaller f-number since the angle of the wave divergence from the focal point is larger and the proposed methods take into account the diffraction effects.

Linear frequency modulated (FM) chirp excitation was also used for FD-VDS and FD-DC. Unlike other SAFT methods that are combined with coded excitation, FD-VDS and FD-DC incorporated decoding of the coded signal into the image reconstruction and do not require additional computational resources. Typically, when linear FM chirp is decoded it results in time or (range) sidelobes which can have comparable amplitudes to the main lobe degrading axial resolution and masking weaker echoes [9], [127]. There are a number of devising schemes for reducing the range sidelobes. In this work, the transmitted linear FM chirp was tapered by a Tukey window to avoid the sharp edges associated with a rectangular shape waveform. However, it causes some reduction in SNR.

## 5.2 Conclusion

In conclusion, FD-VDS had the highest spatial resolution and FD-DC had the second highest spatial resolution. FD-DC had the highest SNR and FD-VDS had higher SNR compared to the CONV but lower than TD-VPS. In addition, FD-VDS and FD-DC had generally lower CTR compared to CONV and TD-VPS. The CSR of FD-VDS, FD-DC and TD-VPS was generally higher than CONV. However, the CSR of FD-VDS and FD-DC was similar to the TD-VPS. Furthermore, the computational run time of FD-VDS and FD-DC (depending on image size) was lower by 4 to 174 times and 4 to 189 times, respectively, compared to the TD-VPS. Since the proposed methods are computationally more efficient than TD-VPS, they can accelerate the implementation of synthetic aperture imaging for real-time imaging and they can provide images with higher frame rates.

Linear FM chirp excitation improved the SNR of all methods by about 8 dB (it should be noted this improvement is depended on the imaging transducer and not on the image reconstruction methods). The SNR of FD-DC was higher than CONV, TD-VPS and FD-VDS by an average of 5.2 dB, 1.3 dB and 1.2 dB, respectively, for both pulsed and chirp excitations. The SNR of FD-VDS and TD-VPS was about the same but compared to CONV their SNR was higher by an average of 4.0 dB and 3.9 dB, respectively, for both

pulsed and chirp excitations. The spatial resolution and the sidelobe level were the same between pulsed and chirp excitations for all the methods. The CSR of all the SAFT methods was generally the same among each other and between the pulsed and chirp excitations. In general, the CSR of CONV for both pulsed and chirp excitations was significantly smaller than the SAFT methods.

Thus, FD-VDS and FD-DC methods offer efficient solutions to improve the image quality compared to TD-VPS in high-frequency ultrasound imaging using single-element focused transducer.

### 5.3 Future Work

This work in this dissertation can be extended for imaging with array transducers, for tissue harmonic imaging and to be used with other coded excitation methods.

FD-VDS and FD-DC can be implemented for array transducers by using a subset of elements to focus the beam at the same point in both transmit and receive, mimicking a single-element focused transducer. FD-VDS and FD-DC image reconstruction can be applied to the acquired data to improve the lateral spatial resolution at all depths. For FD-VDS the electromechanical impulse response, the excitation signal and the far-field diffraction effect of the transducer have to be determined, and for the FD-DC the simulated point spread function of the imaging system has to be determined. Since FD-VDS takes into account the electromechanical impulse response, the excitation signal and the far-field diffraction effect of the transducer and FD-DC takes into account the simulated point spread function of the transducer, it is expected that they would improve the spatial resolution, sidelobe level and SNR of the TD-VPS. In addition, FD-VDS and FD-DC are expected to be significantly more efficient compared to TD-VPS since they are based on fast Fourier transform.

The proposed algorithms can also be implemented for tissue harmonic imaging, where harmonics are generated due to nonlinear ultrasound wave propagation in tissue, for both high-frequency single-element and array transducers. FD-VDS and FD-DC can be applied to the acquired data after extracting the second harmonic signal (e.g., using pulse inversion or band-pass filtering techniques).

In addition, the proposed algorithms can be implemented for other excitation techniques, such as Golay and Barker codes and m-sequences. Compensating the effect of frequency-domain attenuation can also be incorporated in the image reconstruction.

Since the proposed algorithms compensate the electromechanical impulse response of the transducer in the image reconstruction, the proposed methods can be used for imaging with a narrow band therapeutic transducer. This will enable the use of the same transducer (in dual-mode) for both therapy and imaging.

Furthermore, the implementation of the proposed algorithms can be investigated in a commercial scanner to determine their feasibility and performance. The performance of the proposed algorithms can be tested *in vivo* for pre-clinical and clinical applications. The feasibility of the proposed algorithms can also be investigated in optical coherence tomography (OCT).

# Appendix A

## Supplementary materials for Chapter 3

### A.1 Lateral Width of the Point Scatterer

An alternative metric was also used to quantify spatial resolution and side lobe level by measuring the lateral width of the point scatterer (i.e., full-width-at-half-maximum [FWHM]) at  $-6$  dB and  $-24$  dB, respectively. Since the shape of point scatterers is asymmetrical, the measurement of lateral width depends on the location where the measurement is taken. In this study, the lateral widths were measured at the location of the maximum intensity of each point scatterer. The result of the lateral widths for both the simulated and experimental data is shown in Fig. A.1. The lateral widths had a similar trend to the contour areas. The lateral width of the conventional B-mode was larger compared to the SAFT methods outside the focal zone. FD-VDS and FD-DC had generally smaller lateral width compared to the conventional B-mode and TD-VPS.

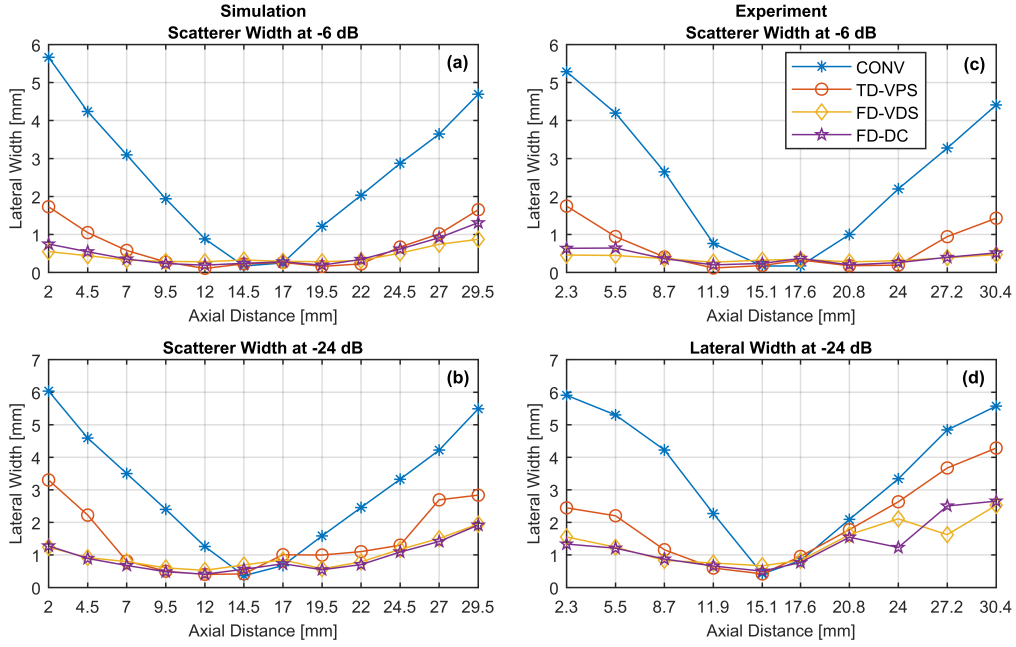


Fig. A.1. The scatterer lateral width of the simulated data at  $-6$  dB (a) and  $-24$  dB (b), and experimental data at  $-6$  dB (c) and  $-24$  dB (d) as a function of depth. The focal distance of the transducer was at 15 mm

## A.2 Statistical Analysis

The average ratio differences in contour area above  $-6$  dB and  $-24$  dB, the average ratio differences in lateral width of point scatterer at  $-6$  dB and  $-24$  dB, and the average difference in SNR between each method for the simulated and experimental data are shown in Fig. A.2. The  $p$ -values were also calculated, using permutation test based on paired t-statistic, to determine if the average differences are statistically significant in a 95% confidence interval. In Fig. A.2,  $p$ -value  $< 0.05$  are shown by the asterisk.

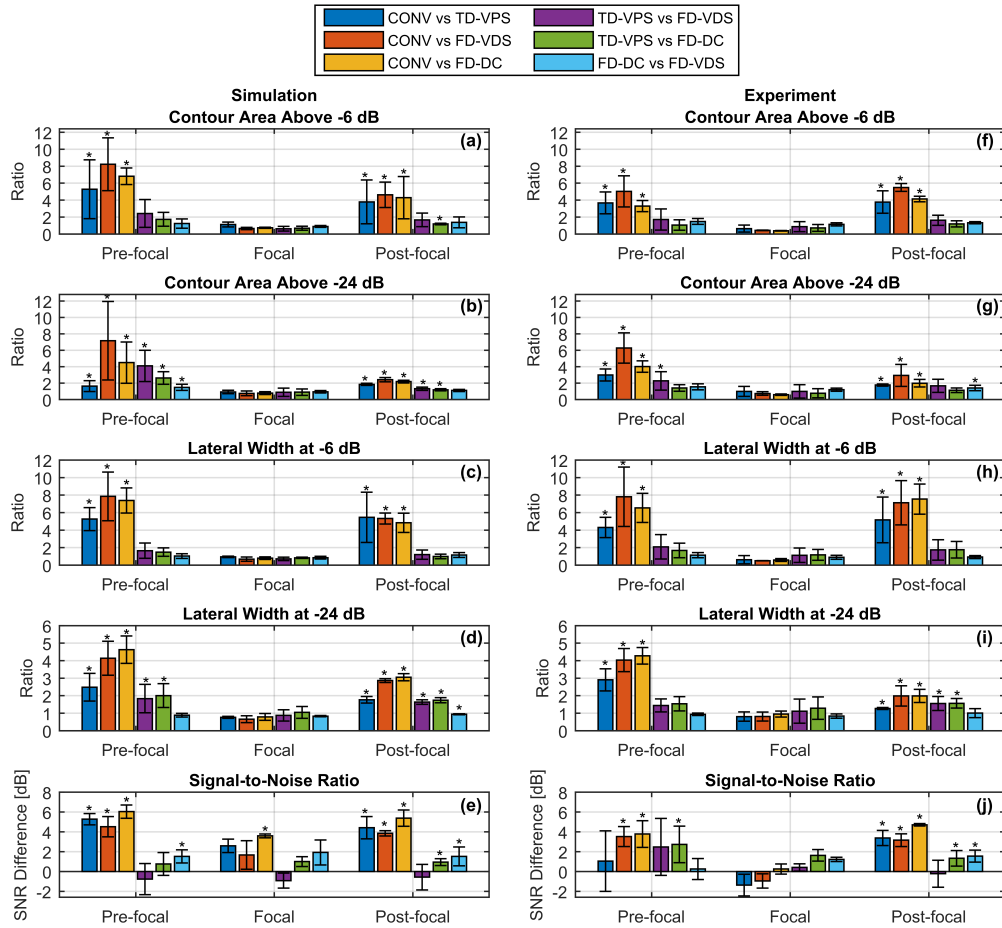


Fig. A.2. The average ratio difference in the contour areas above  $-6$  dB and  $-24$  dB, the average ratio difference in the lateral width of the point scatterers at  $-6$  dB and  $-24$  dB, and the average difference in SNR between the conventional B-mode, TD-VPS, FD-VDS, and FD-DC in the pre-focal, focal and post-focal regions. For the simulated (left column) and experimental (right column) data. The error bars represent standard deviation and \* represents  $p$ -value  $< 0.05$ .

# References

- [1] T. L. Szabo, *Diagnostic ultrasound imaging: inside out*, 2nd ed. Oxford, UK: Academic Press, Inc., 2014, ISBN: 0126801452.
- [2] B. W. Drinkwater and P. D. Wilcox, “Ultrasonic arrays for non-destructive evaluation: A review,” *NDT and E International*, vol. 39, no. 7, pp. 525–541, 2006. DOI: 10.1016/j.ndteint.2006.03.006.
- [3] L. W. Schmerr, *Fundamentals of ultrasonic phased arrays*, 1st ed. New York: Springer International Publishing, 2015, ISBN: 978-3-319-07272-2. DOI: 10.1007/978-3-319-07272-2.
- [4] S. H. Contreras Ortiz, T. Chiu, and M. D. Fox, “Ultrasound image enhancement: A review,” *Biomedical Signal Processing and Control*, vol. 7, no. 5, pp. 419–428, Sep. 2012. DOI: 10.1016/j.bspc.2012.02.002.
- [5] E. G. Moros, *Physics of thermal therapy: fundamentals and clinical applications*, 1st ed., E. G. Moros, Ed. Boca Raton, FL.: CRC Press, 2013, ISBN: 9781439804360.
- [6] M. R. Bailey, V. A. Khokhlova, O. A. Sapozhnikov, S. G. Kargl, and L. A. Crum, “Physical mechanisms of the therapeutic effect of ultrasound (a review),” *Acoustical Physics*, vol. 49, no. 4, pp. 369–388, Jul. 2003. DOI: 10.1134/1.1591291.
- [7] K. K. Shung, *Diagnostic ultrasound: imaging and blood flow measurements*. Boca Raton, FL.: CRC Press, 2006, ISBN: 0-8247-4096-3.
- [8] ———, “High frequency ultrasonic imaging,” *Journal of Medical Ultrasound*, vol. 17, no. 1, pp. 25–30, 2009. DOI: 10.1016/S0929-6441(09)60012-6.

- 
- [9] R. S. C. Cobbold, *Foundations of biomedical ultrasound*. New York: Oxford University Press, 2007, ISBN: 0199775125.
- [10] P. Suetens, *Fundamentals of Medical Imaging*, 2nd. Cambridge: Cambridge University Press, 2002, ISBN: 978-0-511-59640-7.
- [11] P. Hoskins, K. Martin, and A. Thrush, *Diagnostic ultrasound: physics and equipment*, 2nd ed. Cambridge: Cambridge University Press, 2010, ISBN: 978-0-521-75710-2.
- [12] P. Crombie, “Fundamental studies on contrast resolution of ultrasound b-mode images,” PhD thesis, University of Toronto, 1999, pp. 1–164.
- [13] P. N. T. Wells, “Ultrasound imaging.,” *Physics in Medicine and Biology*, vol. 51, R83–R98, 2006. DOI: 10.1088/0031-9155/51/13/R06.
- [14] S. K. Jespersen, J. E. Wilhjelm, and H. Sillesen, “Multi-angle compound imaging,” *Ultrasonic Imaging*, vol. 20, no. 2, pp. 81–102, 1998. DOI: 10.1177/016173469802000201.
- [15] M. Shankar, “Speckle reduction in ultrasound b-scans using weighted averaging in spatial compounding,” *IEEE Transactions on Ultrasonics, Ferroelectrics, and Frequency Control*, vol. 33, no. 6, pp. 754–758, 1986. DOI: 10.1109/T-UFFC.1986.26892.
- [16] P. A. Magnin, O. T. v. Ramm, and F. L. Thurstone, “Frequency compounding for speckle contrast reduction in phased array images,” *Ultrasonic Imaging*, vol. 4, no. 3, pp. 267–281, 1982. DOI: 10.1016/0161-7346(82)90011-6.
- [17] J. H. Chang, H. H. Kim, J. Lee, and K. K. Shung, “Frequency compounded imaging with a high-frequency dual element transducer,” *Ultrasonics*, vol. 50, no. 4-5, pp. 453–457, 2010. DOI: 10.1016/j.ultras.2009.10.003.
- [18] C. Yoon, G. D. Kim, Y. Yoo, T. K. Song, and J. H. Chang, “Frequency equalized compounding for effective speckle reduction in medical ultrasound imaging,” *Biomedical Signal Processing and Control*, vol. 8, no. 6, pp. 876–887, 2013. DOI: 10.1016/j.bspc.2013.08.007.
- [19] T. Misaridis, “Ultrasound imaging using coded signals,” PhD thesis, Technical University of Denmark, 2001, ISBN: 9788578110796.

- [20] R. Y. Chiao and X. Hao, "Coded excitation for diagnostic ultrasound: a system developer's perspective," *IEEE Transactions on Ultrasonics, Ferroelectrics, and Frequency Control*, vol. 52, no. 2, pp. 160–170, 2005. DOI: 10.1109/TUFFC.2005.1406543.
- [21] T. Misaridis and J. A. Jensen, "Use of modulated excitation signals in medical ultrasound. part I: basic concepts and expected benefits.," *IEEE Transactions on Ultrasonics, Ferroelectrics, and Frequency Control*, vol. 52, no. 2, pp. 177–91, Feb. 2005. DOI: 10.1109/TUFFC.2005.1406545.
- [22] L. Ziegler and R. T. O'Brien, "Harmonic ultrasound: a review," *Veterinary Radiology & Ultrasound*, vol. 43, no. 6, pp. 501–509, 2002. DOI: 10.1111/j.1740-8261.2002.tb01040.x.
- [23] R. Lencioni, D. Cioni, and C. Bartolozzi, "Tissue harmonic and contract-specific imaging: back to gray scale in ultrasound," *European Radiology*, vol. 12, no. 1, pp. 151–165, 2002. DOI: 10.1007/s003300101022.
- [24] W. R. Hedrick and L. Metzger, "Tissue harmonic imaging: a review," *Journal of Diagnostic Medical Sonography*, vol. 21, no. 3, pp. 183–189, 2005. DOI: 10.1177/8756479305276477.
- [25] P. J. Frinking, A. Bouakaz, J. Kirkhorn, F. J. Ten Cate, and N. De Jong, "Ultrasound contrast imaging: current and new potential methods," *Ultrasound in Medicine & Biology*, vol. 26, no. 6, pp. 965–975, 2000. DOI: 10.1016/S0301-5629(00)00229-5.
- [26] C.-C. Shen, Y.-H. Chou, and P.-C. Li, "Pulse inversion techniques in ultrasonic nonlinear imaging," *Journal of Medical Ultrasound*, vol. 13, no. 1, pp. 3–17, 2005. DOI: 10.1016/S0929-6441(09)60073-4.
- [27] J. Park, R. Chen, Q. Zhou, and K. K. Shung, "High frequency, high frame rate pulse inversion chirp coded tissue harmonic imaging," in *2011 IEEE International Ultrasonics Symposium Proceedings*, 2011, pp. 2253–2256. DOI: 10.1109/ULTSYM.2011.0559.

- [28] Bamber J.C and Daft. C, “Adaptive filtering for reduction of speckle in ultrasound pulse-echo images,” *Ultrasonics*, vol. 24, no. 1, pp. 41–44, 1986. DOI: 10.1016/0041-624X(86)90072-7.
- [29] R. G. Dantas and E. T. Costa, “Ultrasound speckle reduction using modified gabor filters,” *IEEE Transactions on Ultrasonics, Ferroelectrics, and Frequency Control*, vol. 54, no. 3, pp. 530–538, 2007. DOI: 10.1109/TUFFC.2007.276.
- [30] S. I. Nikolov, “Synthetic aperture tissue and flow ultrasound imaging,” PhD thesis, Technical University of Denmark, 2001.
- [31] J. A. Jensen, S. I. Nikolov, K. L. Gammelmark, and M. H. Pedersen, “Synthetic aperture ultrasound imaging,” *Ultrasonics*, vol. 44, Supple, e5–e15, Dec. 2006. DOI: 10.1016/j.ultras.2006.07.017.
- [32] I. Trots, A. Nowicki, M. Lewandowski, and Y. Tasinkevych, “Synthetic aperture method in ultrasound imaging,” in *Ultrasound Imaging*, M. Tanabe, Ed., Rijeka, Croatia: InTech, 2011, ch. 3, pp. 37–56. DOI: 10.5772/15986.
- [33] M. F. Rasmussen, “Advanced 3-D ultrasound imaging: 3-D synthetic aperture imaging and row-column addressing of 2-D transducer arrays,” PhD thesis, Technical University of Denmark, 2014.
- [34] R. R. Entrekin, B. A. Porter, H. H. Sillesen, A. D. Wong, P. L. Cooperberg, and C. H. Fix, “Real-time spatial compound imaging: application to breast, vascular, and musculoskeletal ultrasound,” *Seminars in Ultrasound CT and MRI*, vol. 22, no. 1, pp. 50–64, 2001. DOI: 10.1016/S0887-2171(01)90018-6.
- [35] S. H. Contreras Ortiz, J. J. Macione, and M. D. Fox, “Enhancement of ultrasound images by displacement, averaging, and interlacing,” *Journal of Electronic Imaging*, vol. 19, no. 1, p. 011 014, 2010. DOI: 10.1117/1.3271168.
- [36] M. Vogt and H. Ermert, “Limited-angle spatial compound imaging of skin with high-frequency ultrasound (20 MHz),” *IEEE Transactions on Ultrasonics, Ferroelectrics, and Frequency Control*, vol. 55, no. 9, pp. 1975–1983, 2008. DOI: 10.1109/TUFFC.888.

- [37] N. B. Smith and A. Webb, *Introduction to medical imaging: physics, engineering and clinical applications*. Cambridge University Press, 2011, ISBN: 9780521190657.
- [38] B. Mesurole, T. Helou, M. El-Khoury, M. Edwardes, E. J. Sutton, and E. Kao, “Tissue harmonic imaging, frequency compound imaging, and conventional imaging,” *Journal of Ultrasound in Medicine*, vol. 26, no. 8, pp. 1041–1051, 2007. DOI: 10.7863/jum.2007.26.8.1041.
- [39] A. Nowicki, Z. Klimonda, M. Lewandowski, J. Litniewski, P. A. Lewin, and I. Trots, “Comparison of sound fields generated by different coded excitations- experimental results,” *Ultrasonics*, vol. 44, no. 1, pp. 121–129, 2006. DOI: 10.1016/j.ultras.2005.10.001.
- [40] M. H. Pedersen, T. X. Misaridis, and J. A. Jensen, “Clinical evaluation of chirp-coded excitation in medical ultrasound,” *Ultrasound in Medicine & Biology*, vol. 29, no. 6, pp. 895–905, 2003. DOI: 10.1016/S0301-5629(02)00784-6.
- [41] T. A. Whittingham, “Tissue harmonic imaging,” *European Radiology*, vol. 9, no. Suppl 3, S323–S326, 1999.
- [42] F. Duck, “Tissue non-linearity,” *Proceedings of the Institution of Mechanical Engineers, Part H: Journal of Engineering in Medicine*, vol. 224, no. 2, pp. 155–170, 2010. DOI: 10.1243/09544119JEIM574.
- [43] M. Claudon, F. Tranquart, D. H. Evans, F. Lefevre, and J. M. Correas, “Advances in ultrasound,” *European Radiology*, vol. 12, no. 1, pp. 7–18, 2002. DOI: 10.1007/s00330-001-1185-1.
- [44] J. D. Thomas and D. N. Rubin, “Tissue harmonic imaging: why does it work?” *Journal of the American Society of Echocardiography*, vol. 11, no. 8, pp. 803–808, 1998. DOI: 10.1016/S0894-7317(98)70055-0.
- [45] U. Bartram and K. Darge, “Harmonic versus conventional ultrasound imaging of the urinary tract in children,” *Pediatric Radiology*, vol. 35, no. 7, pp. 655–660, 2005. DOI: 10.1007/s00247-005-1415-9.

- [46] D. H. Simpson, C. T. Chin, and P. N. Burns, "Pulse inversion Doppler: a new method for detecting nonlinear echoes from microbubble contrast agents," *IEEE Transactions on Ultrasonics, Ferroelectrics, and Frequency Control*, vol. 46, no. 2, pp. 372–382, 1999. DOI: 10.1109/58.753026.
- [47] M. Cheney and B. Borden, *Fundamentals of radar imaging*. Philadelphia, PA: Society for Industrial and Applied Mathematics, 2009, ISBN: 978-0898716-77-1.
- [48] M. Soumekh, *Synthetic aperture radar signal processing with MATLAB algorithms*. Hoboken, New Jersey: John Wiley & Sons, Inc., 1999, ISBN: 0-471-29706-2.
- [49] L. J. Cutrona, "Synthetic aperture radar," in *Radar Handbook*, M. I. Skolnik, Ed., 2nd ed., Boston, Massachusetts: McGraw-Hill, Inc., 1990, ch. 21, pp. 1–21, ISBN: 0-07-057913-X.
- [50] M. A. Richards, *Fundamentals of radar signal processing*. New York, NY: McGraw-Hill, Inc., 2005, ISBN: 0071444742.
- [51] P. T. Gough and D. W. Hawkins, "Imaging algorithms for a strip-map synthetic aperture sonar: minimizing the effects of aperture errors and aperture undersampling," *IEEE Journal of Oceanic Engineering*, vol. 22, no. 1, pp. 27–39, 1997. DOI: 10.1109/48.557537.
- [52] S. Doctor, T. Hall, and L. Reid, "SAFT - the evolution of a signal processing technology for ultrasonic testing," *NDT International*, vol. 19, no. 3, pp. 163–167, 1986. DOI: 10.1016/0308-9126(86)90105-7.
- [53] C. B. Burckhardt, P.-A. Grandchamp, and H. Hoffmann, "An experimental 2 MHz synthetic aperture sonar system intended for medical use," *IEEE Transactions on Sonics and Ultrasonics*, vol. 21, no. 1, pp. 1–6, 1974. DOI: 10.1109/T-SU.1974.29783.
- [54] P. T. Gough and D. W. Hawkins, "Unified framework for modern synthetic aperture imaging algorithms," *International Journal of Imaging Systems and Technology*, vol. 8, no. 4, pp. 343–358, 1997. DOI: 10.1002/(SICI)1098-1098(1997)8:4<343::AID-IMA2>3.0.CO;2-A.

- 
- [55] D. W. Hawkins, "Synthetic aperture imaging algorithms: with application to wide bandwidth sonar," PhD thesis, University of Canterbury, 1996.
- [56] T. Stepinski, "An implementation of synthetic aperture focusing technique in frequency domain," *IEEE Transactions on Ultrasonics, Ferroelectrics, and Frequency Control*, vol. 54, no. 7, pp. 1399–1408, Jul. 2007. DOI: 10.1109/TUFFC.2007.400.
- [57] Y. Ozaki, H. Sumitani, T. Tomoda, and M. Tanaka, "A new system for real-time synthetic aperture ultrasonic imaging," *IEEE Transactions on Ultrasonics, Ferroelectrics, and Frequency Control*, vol. 35, no. 6, pp. 828–838, 1988. DOI: 10.1109/58.9340.
- [58] M. O'Donnell and L. J. Thomas, "Efficient synthetic aperture imaging from a circular aperture with possible application to catheter-based imaging," *IEEE Transactions on Ultrasonics, Ferroelectrics, and Frequency Control*, vol. 39, no. 3, pp. 366–380, 1992. DOI: 10.1109/58.143171.
- [59] F. Lingvall, "Time-domain reconstruction methods for ultrasonic array imaging: a statistical approach," PhD thesis, Uppsala University, 2004, ISBN: 91-506-1772-9.
- [60] J. T. Ylitalo and H. Ermert, "Ultrasound synthetic aperture imaging: monostatic approach," *IEEE Transactions on Ultrasonics, Ferroelectrics, and Frequency Control*, vol. 41, no. 3, pp. 333–339, May 1994. DOI: 10.1109/58.285467.
- [61] C. Passmann and H. Ermert, "A 100-MHz ultrasound imaging system for dermatologic and ophthalmologic diagnostics," *IEEE Transactions on Ultrasonics, Ferroelectrics, and Frequency Control*, vol. 43, no. 4, pp. 545–552, 1996. DOI: 10.1109/58.503714.
- [62] C. H. Frazier and W. D. O'Brien, "Synthetic aperture techniques with a virtual source element," *IEEE Transactions on Ultrasonics, Ferroelectrics, and Frequency Control*, vol. 45, no. 1, pp. 196–207, Jan. 1998. DOI: 10.1109/58.646925.

- [63] M.-L. Li, W.-J. Guan, and P.-C. Li, “Improved synthetic aperture focusing technique with applications in high-frequency ultrasound imaging,” *IEEE Transactions on Ultrasonics, Ferroelectrics, and Frequency Control*, vol. 51, no. 1, pp. 63–70, 2004. DOI: 10.1109/TUFFC.2004.1268468.
- [64] J. Opretzka, M. Vogt, and H. Ermert, “A model-based synthetic aperture image reconstruction technique for high-frequency ultrasound,” in *Proceedings 2009 IEEE International Ultrasonics Symposium*, Rome, Italy, 2009, pp. 377–380. DOI: 10.1109/ULTSYM.2009.5441990.
- [65] ———, “A high-frequency ultrasound imaging system combining limited-angle spatial compounding and model-based synthetic aperture focusing,” *IEEE Transactions on Ultrasonics, Ferroelectrics, and Frequency Control*, vol. 58, no. 7, pp. 1355–65, Jul. 2011. DOI: 10.1109/TUFFC.2011.1955.
- [66] H. Ermert and R. Karg, “Multifrequency acoustical holography,” *IEEE Transactions on Sonics and Ultrasonics*, vol. 26, no. 4, pp. 279–285, Jul. 1979. DOI: 10.1109/T-SU.1979.31101.
- [67] K. Nagai, “A new synthetic-aperture focusing method for ultrasonic b-scan imaging by the Fourier transform,” *IEEE Transactions on Sonics and Ultrasonics*, vol. 32, no. 4, pp. 531–536, Jul. 1985. DOI: 10.1109/T-SU.1985.31627.
- [68] H. J. Vos, P. L. M. J. v. Neer, M. M. Mota, M. D. Verweij, A. F. W. v. d. Steen, and A. W. F. Volker, “F-k domain imaging for synthetic aperture sequential beamforming,” *IEEE Transactions on Ultrasonics, Ferroelectrics, and Frequency Control*, vol. 63, no. 1, pp. 60–71, 2016. DOI: 10.1109/TUFFC.2015.2499839.
- [69] R. Y. Chiao, L. J. Thomas, and S. D. Silverstein, “Sparse array imaging with spatially-encoded transmits,” in *1997 IEEE Ultrasonics Symposium Proceedings*, vol. 2, 1997, pp. 1679–1682. DOI: 10.1109/ULTSYM.1997.663318.

- [70] M. Karaman, P.-C. Li, and M. O'Donnell, "Synthetic aperture imaging for small scale systems," *IEEE Transactions on Ultrasonics, Ferroelectrics, and Frequency Control*, vol. 42, no. 3, pp. 429–442, 1995. DOI: 10.1109/58.384453.
- [71] K. L. Gammelmark and J. A. Jensen, "Experimental study of convex coded synthetic transmit aperture imaging," in *2002 IEEE Ultrasonics Symposium Proceedings*, vol. 2, Munich, Germany, 2002, pp. 1613–1617. DOI: 10.1109/ULTSYM.2002.1192603.
- [72] K. L. Gammelmark and J. A. Jensen, "Multielement synthetic transmit aperture imaging using temporal encoding," *IEEE Transactions on Medical Imaging*, vol. 22, no. 4, pp. 552–563, 2003. DOI: 10.1109/TMI.2003.811048.
- [73] M. H. Pedersen, K. L. Gammelmark, and J. A. Jensen, "In-vivo evaluation of convex array synthetic aperture imaging," *Ultrasound in Medicine & Biology*, vol. 33, no. 1, pp. 37–47, 2007. DOI: 10.1016/j.ultrasmedbio.2006.07.041.
- [74] J. Kortbek, J. A. Jensen, and K. L. Gammelmark, "Sequential beamforming for synthetic aperture imaging," *Ultrasonics*, vol. 53, no. 1, pp. 1–16, Jan. 2013. DOI: 10.1016/j.ultras.2012.06.006.
- [75] G. Lockwood, J. Talman, and S. Brunke, "Real-time 3-D ultrasound imaging using sparse synthetic aperture beamforming," *IEEE Transactions on Ultrasonics, Ferroelectrics, and Frequency Control*, vol. 45, no. 4, pp. 980–988, Jul. 1998. DOI: 10.1109/58.710573.
- [76] S. I. Nikolov, K. L. Gammelmark, and J. A. Jensen, "Recursive ultrasound imaging," *1999 IEEE Ultrasonics Symposium Proceedings*, vol. 2, pp. 1621–1625, 1999. DOI: 10.1109/ULTSYM.1999.849306.
- [77] Y. Tasinkevych, Z. Klimonda, M. Lewandowski, A. Nowicki, and P. A. Lewin, "Modified multi-element synthetic transmit aperture method for ultrasound imaging: a tissue phantom study," *Ultrasonics*, vol. 53, no. 2, pp. 570–579, 2013. DOI: 10.1016/j.ultras.2012.10.001.

- [78] M.-H. Bae and M.-K. Jeong, “A study of synthetic-aperture imaging with virtual source elements in B-mode ultrasound imaging systems,” *IEEE Transactions on Ultrasonics, Ferroelectrics, and Frequency Control*, vol. 47, no. 6, pp. 1510–1519, 2000. DOI: 10.1109/58.883540.
- [79] S. I. Nikolov and J. A. Jensen, “3D synthetic aperture imaging using a virtual source element in the elevation plane,” in *2000 IEEE Ultrasonics Symposium Proceedings*, vol. 2, San Juan, Puerto Rico, 2000, pp. 1743–1747. DOI: 10.1109/ULTSYM.2000.921659.
- [80] —, “Virtual ultrasound sources in high-resolution ultrasound imaging,” in *Proceedings SPIE 4687, Medical Imaging 2002: Ultrasonic Imaging and Signal Processing*, vol. 4687, San Diego, California, 2002, pp. 395–405. DOI: 10.1117/12.462178.
- [81] G. E. Trahey and L. F. Nock, “Synthetic receive aperture imaging with phase correction for motion and for tissue inhomogeneities. Part II: Effects of and correction for motion,” *IEEE Transactions on Ultrasonics, Ferroelectrics, and Frequency Control*, vol. 39, no. 4, pp. 496–501, 1992. DOI: 10.1109/58.148540.
- [82] K. L. Gammelmark, “Improving the image quality of synthetic transmit aperture ultrasound images: achieving real-time in-vivo imaging,” PhD thesis, Technical University of Denmark, 2004.
- [83] R. Y. Chiao and L. J. Thomas, “Synthetic transmit aperture imaging using orthogonal Golay coded excitation,” *Proceedings 2000 IEEE Ultrasonics Symposium*, pp. 1677–1680, 2000. DOI: 10.1109/ULTSYM.2000.921644.
- [84] T. Misaridis and J. A. Jensen, “Use of modulated excitation signals in medical ultrasound. part III: high frame rate imaging,” *IEEE Transactions on Ultrasonics, Ferroelectrics, and Frequency Control*, vol. 52, no. 2, pp. 208–218, 2005. DOI: 10.1109/TUFFC.2005.1406547.

- [85] M. O'Donnell and Y. Wang, "Coded excitation for synthetic aperture ultrasound imaging," *IEEE Transactions on Ultrasonics, Ferroelectrics, and Frequency Control*, vol. 52, no. 2, pp. 171–176, 2005. DOI: 10.1109/TUFFC.2005.1406544.
- [86] G. A. Showman, "Stripmap SAR," in *Principles of modern radar: advanced techniques*, W. L. Melvin and J. A. Scheer, Eds., Edision, New Jersey: Scitech Publishing, 2012, ch. 7, pp. 259–335, ISBN: 9781891121531.
- [87] B.-C. Wang, *Digital signal processing techniques and applications in radar image processing*. John Wiley & Sons, Inc., 2008, ISBN: 978-0-470-18092-1.
- [88] J. Schmerr Lester W, *Fundamentals of ultrasonic nondestructive evaluation: a modeling approach*. New York: Plenum Press, 1998, ISBN: 0306457520.
- [89] R. H. Stolt, "Migration by Fourier transform," *Geophysics*, vol. 43, no. 1, pp. 23–48, 1978. DOI: 10.1190/1.1440826.
- [90] G. F. Margrave and M. P. Lamoureux, *Numerical methods of exploration seismology with algorithms in MATLAB*. Cambridge, UK: Cambridge University Press, 2018, ISBN: 9781316756041. DOI: 10.1017/9781316756041.
- [91] R. Bamler, "A comparison of range-Doppler and wavenumber domain SAR focusing algorithms," *IEEE Transactions on Geoscience and Remote Sensing*, vol. 30, no. 3, pp. 706–713, 1992. DOI: 10.1109/36.158864.
- [92] C. R. Hill, J. C. Bamber, and G. R. ter Haar, Eds., *Physical principles of medical ultrasonics*, 2nd. Chichester, UK: John Wiley & Sons, Ltd, 2004, ISBN: 9780470093979.
- [93] M. S. Patterson and F. S. Foster, "The improvement and quantitative assessment of B-mode images produced by an annular array/cone hybrid," *Ultrasonic Imaging*, vol. 5, no. 3, pp. 195–213, 1983. DOI: 10.1177/016173468300500301.

- [94] K. F. Üstüner and G. L. Holley, "Ultrasound imaging system performance assessment," in *Proceedings AAPM 45th Annual Meeting*, 2003. [Online]. Available: <http://www.aapm.org/meetings/03AM/pdf/9905-9858.pdf>.
- [95] G. Montaldo, M. Tanter, J. Bercoff, N. Benech, and M. Fink, "Coherent plane-wave compounding for very high frame rate ultrasonography and transient elastography," *IEEE Transactions on Ultrasonics, Ferroelectrics, and Frequency Control*, vol. 56, no. 3, pp. 489–506, 2009. DOI: 10.1109/TUFFC.2009.1067.
- [96] R. Kleinerman, T. B. Whang, R. L. Bard, and E. S. Marmur, "Ultrasound in dermatology: principles and applications," *Journal of the American Academy of Dermatology*, vol. 67, no. 3, pp. 478–487, 2012. DOI: 10.1016/j.jaad.2011.12.016.
- [97] F. Alfageme Roldán, "Ultrasound skin imaging," *Actas Dermo-Sifil-iográficas*, vol. 105, no. 10, pp. 891–899, 2014. DOI: 10.1016/j.ad.2013.11.015.
- [98] C. J. Pavlin and F. S. Foster, *Ultrasound biomicroscopy of the eye*. New York: Springer-Verlag, 1995, ISBN: 978-1-4612-7551-0. DOI: 10.1007/978-1-4612-2470-9.
- [99] F. S. Foster, C. J. Pavlin, K. A. Harasiewicz, D. A. Christopher, and D. H. Turnbull, "Advances in ultrasound biomicroscopy," *Ultrasound in Medicine & Biology*, vol. 26, no. 1, pp. 1–27, 2000. DOI: 10.1016/S0301-5629(99)00096-4.
- [100] S. A. Hewick, A. C. Fairhead, J. C. Culy, and H. R. Atta, "A comparison of 10 MHz and 20 MHz ultrasound probes in imaging the eye and orbit," *British Journal of Ophthalmology*, vol. 88, no. 4, pp. 551–555, 2004. DOI: 10.1136/bjo.2003.028126.
- [101] G. J. Latham, M. L. Veneracion, D. C. Joffe, A. T. Bosenberg, S. H. Flack, and D. K. Low, "High-frequency micro-ultrasound for vascular access in young children - a feasibility study by the High-frequency UltraSound in Kids studY (HUSKY) group," *Paediatric Anaesthesia*, vol. 23, no. 6, pp. 529–535, 2013. DOI: 10.1111/pan.12131.

- [102] B. J. Potkin, A. L. Bartorelli, J. M. Gessert, R. F. Neville, Y. Almagor, W. C. Roberts, and M. B. Leon, "Coronary artery imaging with intravascular high-frequency ultrasound," *Circulation*, vol. 81, no. 5, pp. 1575–1585, 1990. DOI: 10.1161/01.CIR.81.5.1575.
- [103] F. S. Foster, M. Y. Zhang, Y. Q. Zhou, G. Liu, J. Mehi, E. Cherin, K. A. Harasiewicz, B. G. Starkoski, L. Zan, D. A. Knapik, and S. L. Adamson, "A new ultrasound instrument for in vivo microimaging of mice," *Ultrasound in Medicine & Biology*, vol. 28, no. 9, pp. 1165–1172, 2002. DOI: 10.1016/S0301-5629(02)00567-7.
- [104] L. Sun, X. Xu, W. D. Richard, C. Feng, J. A. Johnson, and K. K. Shung, "A high-frame rate duplex ultrasound biomicroscopy for small animal imaging in vivo," *IEEE Transactions on Biomedical Engineering*, vol. 55, no. 8, pp. 2039–2049, 2008. DOI: 10.1109/TBME.2008.919110.
- [105] L. Sun, C. L. Lien, X. Xu, and K. K. Shung, "In vivo cardiac imaging of adult zebrafish using high frequency ultrasound (45-75 MHz)," *Ultrasound in Medicine & Biology*, vol. 34, no. 1, pp. 31–39, 2008. DOI: 10.1016/j.ultrasmedbio.2007.07.002.
- [106] F. S. Foster, J. Mehi, M. Lukacs, D. Hirson, C. White, C. Chaggares, and A. Needles, "A New 15-50 MHz array-based micro-ultrasound scanner for preclinical imaging," *Ultrasound in Medicine & Biology*, vol. 35, no. 10, pp. 1700–1708, 2009. DOI: 10.1016/j.ultrasmedbio.2009.04.012.
- [107] I. Trots, A. Nowicki, and M. Lewandowski, "Synthetic transmit aperture in ultrasound imaging," *Archives of Acoustics*, vol. 34, no. 4, pp. 685–695, 2009, ISSN: 2300-262X.
- [108] P. Després and X. Jia, "A review of GPU-based medical image reconstruction," *Physica Medica*, vol. 42, pp. 76–92, 2017. DOI: 10.1016/j.ejmp.2017.07.024.
- [109] D. Romero, O. Martínez-Graullera, C. J. Martín, R. T. Higuí, and A. Octavio, "Using GPUs for beamforming acceleration on SAFT imaging," in *2009 IEEE Ultrasonics Symposium Proceedings*, Rome,

- Italy: IEEE, 2009, pp. 1334–1337. DOI: 10.1109/ULTSYM.2009.5441790.
- [110] J. Amaro, G. Falcao, B. Y. Yiu, and A. C. H. Yu, “Portable parallel kernels for high-speed beamforming in synthetic aperture ultrasound imaging,” in *2013 IEEE International Conference on Acoustics, Speech and Signal Processing*, Vancouver, BC, Canada: IEEE, 2013, pp. 2688–2692. DOI: 10.1109/ICASSP.2013.6638144.
- [111] S. Umchid, “Directivity pattern measurement of ultrasound transducers,” *International Journal of Applied Biomedical Engineering*, vol. 2, no. 1, pp. 39–43, 2009.
- [112] N. Nayebi, “Synthetic aperture imaging: applications in high-frequency ultrasound,” PhD thesis, Ryerson University, 2008.
- [113] G. Ameri, “Synthetic aperture imaging in acoustic microscopy,” PhD thesis, Ryerson University, 2011.
- [114] J. A. Jensen, “Field: a program for simulating ultrasound systems,” in *10th Nordic-Baltic Conference on Biomedical Imaging*, vol. 34, Medical & Biological Engineering & Computing, 1996, pp. 351–353.
- [115] E. E. Hundt and E. A. Trautenberg, “Digital processing of ultrasonic data by deconvolution,” *IEEE Transactions on Sonics and Ultrasonics*, vol. 27, no. 5, pp. 249–252, 1980. DOI: 10.1109/T-SU.1980.31185.
- [116] O. V. Michailovich and D. Adam, “A novel approach to the 2-D blind deconvolution problem in medical ultrasound,” *IEEE Transactions on Medical Imaging*, vol. 24, no. 1, pp. 86–104, 2005. DOI: 10.1109/TMI.2004.838326.
- [117] D. Kim, J. Park, J. Cho, T.-K. Song, and Y. Yoo, “New synthetic aperture imaging technique with dynamic apodization window,” in *Proceedings SPIE 8320, Medical Imaging 2012: Ultrasonic Imaging, Tomography, and Therapy*, San Diego, California, 2012. DOI: 10.1117/12.912356.

- [118] J. A. Jensen and N. B. Svendsen, "Calculation of pressure fields from arbitrarily shaped, apodized, and excited ultrasound transducers," *IEEE Transactions on Ultrasonics, Ferroelectrics, and Frequency Control*, vol. 39, no. 2, pp. 262–267, 1992. DOI: 10.1109/58.139123.
- [119] J. A. Jensen, "A model for the propagation and scattering of ultrasound in tissue," *The Journal of the Acoustical Society of America*, vol. 89, no. 1, pp. 182–190, 1991. DOI: 10.1121/1.400497.
- [120] R. E. Baddour, M. D. Sherar, J. W. Hunt, G. J. Czarnota, and M. C. Kolios, "High-frequency ultrasound scattering from microspheres and single cells," *The Journal of the Acoustical Society of America*, vol. 117, no. 2, pp. 934–943, 2005. DOI: 10.1121/1.1830668.
- [121] D. Foster, M. Arditi, F. Foster, M. Patterson, and J. Hunt, "Computer simulations of speckle in B-scan images," *Ultrasonic Imaging*, vol. 5, no. 4, pp. 308–330, 1983. DOI: 10.1016/S0161-7346(83)81004-9.
- [122] P. Kruizinga, F. Mastik, N. De Jong, A. F. W. Van der Steen, and G. Van Soest, "Plane-wave ultrasound beamforming using a nonuniform fast Fourier transform," *IEEE Transactions on Ultrasonics, Ferroelectrics, and Frequency Control*, vol. 59, no. 12, pp. 2684–2691, 2012. DOI: 10.1109/TUFFC.2012.2509.
- [123] E. Shaswary, J. Tavakkoli, and J. C. Kumaradas, "Efficient frequency-domain synthetic aperture focusing techniques for imaging with a high-frequency single-element focused transducer," *IEEE Transactions on Ultrasonics, Ferroelectrics, and Frequency Control*, vol. 66, no. 1, pp. 57–70, Jan. 2019. DOI: 10.1109/TUFFC.2018.2881726.
- [124] E. Moghimirad, C. A. V. Hoyos, A. Mahloojifar, B. M. Asl, and J. A. Jensen, "Synthetic aperture ultrasound Fourier beamformation using virtual sources," *IEEE Transactions on Ultrasonics, Ferroelectrics, and Frequency Control*, vol. 63, no. 12, pp. 2018–2030, 2016. DOI: 10.1109/TUFFC.2016.2606878.

- [125] C. Cafforio, C. Prati, and F. Rocca, "SAR data focusing using seismic migration techniques," *IEEE Transactions on Aerospace and Electronic Systems*, vol. 27, no. 2, pp. 194–207, Mar. 1991. DOI: 10.1109/7.78293.
- [126] N. Rao, "Investigation of a pulse compression technique for medical ultrasound: a simulation study," *Medical and Biological Engineering and Computing*, vol. 32, no. 2, pp. 181–188, 1994. DOI: 10.1007/BF02518916.
- [127] T. Misaridis, J. A. Jensen, and S. Member, "Use of modulated excitation signals in medical ultrasound. part II: design and performance for medical imaging applications.," *IEEE Transactions on Ultrasonics, Ferroelectrics, and Frequency Control*, vol. 52, no. 2, pp. 192–207, 2005. DOI: 10.1109/TUFFC.2005.1406546.
- [128] Y. Takeuchi, "An investigation of a spread energy method for medical ultrasound systems. part one: theory and investigation," *Ultrasonics*, vol. 17, no. July, pp. 219–224, 1979. DOI: 10.1016/0041-624X(79)90052-0.
- [129] S. Zhou, X.-C. Wang, J. Yang, J.-J. Ji, and Y.-Q. Wang, "Barker-coded excitation in ophthalmological ultrasound imaging.," *International Journal of Clinical and Experimental Medicine*, vol. 7, no. 9, pp. 2413–24, 2014, ISSN: 1940-5901.
- [130] Jian Shen and E. Ebbini, "A new coded-excitation ultrasound imaging system. I. Basic principles," *IEEE Transactions on Ultrasonics, Ferroelectrics, and Frequency Control*, vol. 43, no. 1, pp. 131–140, Jan. 1996, ISSN: 0885-3010. DOI: 10.1109/58.484472.
- [131] B. Lashkari, K. Zhang, and A. Mandelis, "High-frame-rate synthetic aperture ultrasound imaging using mismatched coded excitation waveform engineering: a feasibility study," *IEEE Transactions on Ultrasonics, Ferroelectrics, and Frequency Control*, vol. 63, no. 6, pp. 828–841, 2016. DOI: 10.1109/TUFFC.2016.2551705.

- 
- [132] B. Lashkari, K. Zhang, E. Dvblo, and A. Mandelis, “Coded excitation waveform engineering for high frame rate synthetic aperture ultrasound imaging,” *Ultrasonics*, vol. 77, pp. 121–132, 2017. DOI: 10.1016/j.ultras.2017.02.007.
- [133] G. S. Kino, *Acoustic waves: devices, imaging, and analog signal processing*. New Jersey: Prentice Hall, Inc., 1987, ISBN: 0130030473.